Ryerson University
Digital Commons @ Ryerson

1-1-2011

Numerical heat transfer analysis of micro-scale jet-impingement cooling in a high-pressure turbine vane

Karan Anand
Ryerson University

NUMERICAL HEAT TRANSFER ANALYSIS OF MICRO-SCALE JET-IMPINGEMENT
COOLING IN A HIGH-PRESSURE TURBINE VANE

by

Karan Anand
B. Eng Aerospace Engineering, 2009
Ryerson University

A thesis
presented to Ryerson University

in partial fulfillment of the
requirements for the degree of

Master of Applied Science
in the program of
Aerospace Engineering

Toronto, Ontario, Canada, 2011

© Karan Anand 2011

AUTHOR'S DECLARATION

I hereby declare that I, Karan Anand, am the sole author of this thesis.

I authorize Ryerson University to lend this thesis to other institutions or individuals for the purpose of scholarly research.

_____

Karan Anand

I further authorize Ryerson University to reproduce this thesis or dissertation by photocopying or by other means, in total or in part, at the request of other institutions or individuals for the purpose of scholarly research.

_____

Karan Anand

ABSTRACT

NUMERICAL HEAT TRANSFER ANALYSIS OF MICRO-SCALE JET-IMPINGEMENT
COOLING IN A HIGH-PRESSURE TURBINE VANE

Master of Applied Science
2011

Karan Anand
Aerospace Engineering
Ryerson University

This research provides a computational analysis of heat transfer due to micro jet-impingement inside a gas turbine vane. A preliminary-parametric analysis of axisymmetric single jet was reported to better understand micro jet-impingement. In general, it was seen that as the Reynolds number increased the Nusselt number values increased. The jet to target spacing had a considerably lower impact on the heat transfer rates. Around 30% improvement was seen by reducing the diameter to half while changing the shape to an ellipse saw 20.8% improvement in Nusselt value. The numerical investigation was then followed by studying the heat transfer characteristics in a three-dimensional, actual-shaped turbine vane. Effects of jet inclination showed enhanced mixing and secondary heat transfer peaks. The effect of reducing the diameter of the jets to 0.125 mm yielded 55% heat transfer improvements compared to 0.51 mm; the tapering effect also enhanced the local heat transfer values as local velocities at jet exit increased.

ACKNOWLEDGEMENTS

TABLE OF CONTENTS

LIST OF TABLES

LIST OF FIGURES

NOMENCLATURE

Latin

A	*Area*	N_2	*Number of Elements for Coarse Grid*	
a	*Semi-Major Axis*	N_A	*Avogadro's Number*	
b	*Semi-Minor Axis*	P	*Perimeter, Absolute Pressure*	
C	*Constant (Length of Potential Core)*	q_s	*Total Heat Surface Heat Flux*	
D	*Nozzle Diameter*	R	*Gas Constant*	
d	*Diameter of Air Molecule*	r	*Radial Direction*	
D_H	*Hydraulic Diameter*	$r_{effective}$	*Effective Refinement Factor*	
E^3	*Energy Efficient Engine*	T	*Thermodynamic Temperature*	
F(z)	*Complex Potential*	T_j	*Jet Temperature*	
G	*Mass Flow per Heat Area*	T_s	*Target Plate Surface Temperature*	
H	*Nozzle to Target Distance*	u	*x Direction Velocity Component*	
h	*Convective Heat Transfer Coefficient*	u'	*Velocity Fluctuations*	
I	*Turbulence Intensity*	u_m	*Maximum Velocity*	
k	*Thermal Conductivity of Jet*	u_{oc}	*Velocity at Origin of Jet (Nozzle Exit)*	
K_n	*Knudsen Number*	V	*Volume of Gas*	
L_c	*Chord Length*	v	*y Direction Velocity Component*	
L_e	*Entrance Length*	W	*Nozzle Slot Width*	
n	*Number of Moles of Gas*	z	*Along the Normal Direction*	
N_1	*Number of Elements for Fine Grid*	U_∞	*Free Stream Velocity*	

Greek

δ	*Boundary Layer Thickness*	Φ	*Velocity Potential*
η	*Adiabatic Effectiveness*	Ψ	*Stream Function*
λ	*Mean Free Path Length*	μ	*Viscosity*
ρ	*Density*		

Abbreviations

CFD	*Computational Fluid Dynamics*	Pr	*Prandtl Number*
FOD	*Foreign Object Damage*	Re	*Reynolds Number*
GCI	*Grid Convergence Index*	SFC	*Specific Fuel Consumption*
GTE	*Gas Turbine Engine*	TIT	*Turbine Inlet Temperature*
N-S	*Navier-Stokes*	Nu	*Nusselt Number*

CHAPTER ONE

INTRODUCTION

Cooling schemes for hot flow gas-path components in a modern gas turbine engine (GTE) are required to continue to outperform the current cooling effectiveness and efficiency. The thermal efficiency, specific power output and specific weight in GTE(s) are improved by operating the engine at high turbine inlet temperatures (TIT) of about 2700-3200 ˚F [1,2]. Figure 1-1 shows the relationship between specific core power and rotor TIT, illustrating the trends of gas turbine development. The core power stoichiometric limit is almost 4 times higher than current production engines [1]. Realizing that actual engines will achieve lower than ideal cycle performance, an improvement of 2.5 times the current engine performance is expected in the near future [3]. The improvement in thermal efficiency is an added benefit to the enhanced core power. Figure 1-2 demonstrates this behavior as reduction in specific fuel consumption (SFC) is obtained for increased TIT. However, the TIT is also amongst the most important factors limiting the engine performance [4].
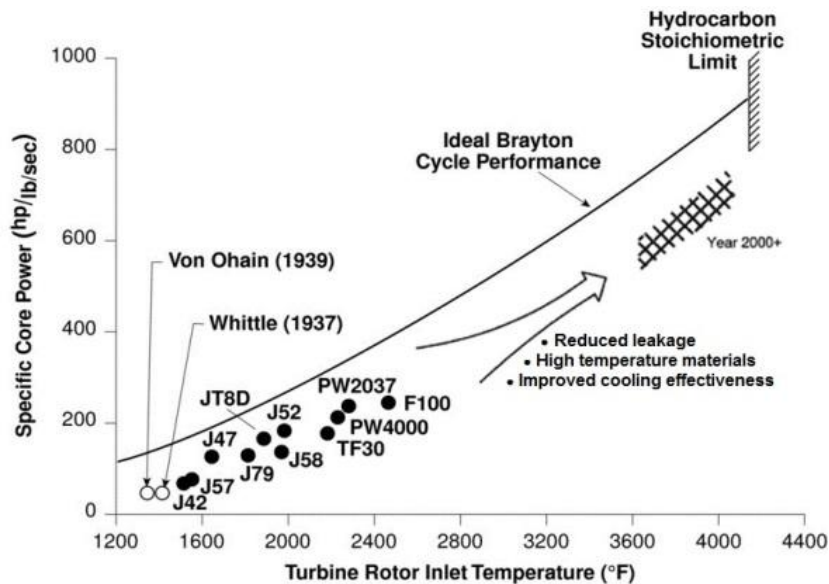
Figure 1-1: Trends in rotor TIT [3]

---

[1] Stoichiometric limit is defined as the limit where all the oxygen and fuel are consumed. This occurs at fuel to air ratio of 0.068.

1
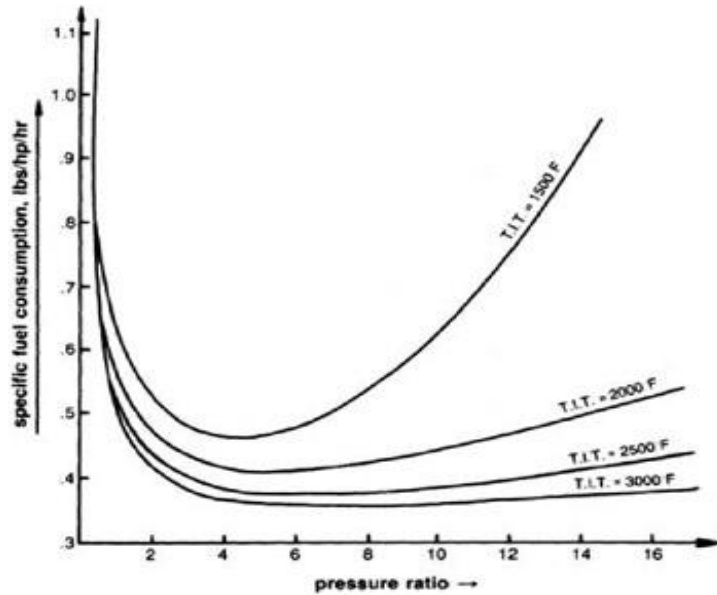
Figure 1-2: Relation between TIT and SFC [5]

One of the reasons for the TIT being the limiting factor of engine performance is the melting temperatures of the materials used. Advances in the material technology have had a significant progress on turbine performance. However, the TIT(s) mentioned previously (2700-320 ˚F) are about 650˚F above the melting temperatures of super alloys. Hence, cooling schemes are introduced that allow turbines to operate close to the temperature limits of these materials. It is also important to recognize that about 20-30% of the core flow is depleted in the cooling systems employed in a GTE to sustain these temperature loads [3]. This depletion further affects the engine performance.

Another factor affecting the turbine performance is the cooling airflow entering the mainstream gas flow. The cooling airflow from the turbine generally causes a momentum drop when the coolant enters the hot gas flow passage, usually around the trailing edge of the airfoil. Thus, the variation in the ratio of coolant temperature and mainstream temperature and the coolant exit velocity and mainstream Mach number induces mixing losses [3].

Leakages due to various components of the turbine, such as disks, seals, specialized chambers for cooling and vanes deteriorate the turbine's performance. All above-mentioned factors directly or indirectly correlate to the increased TIT being the limiting factor [6].

2

The repercussions of the turbine's rigorous environment involve three modes of turbine failure. The first mode of failure is creep. Metal creep is time, temperature and load dependent. Moreover, in the turbine's environment, the blades of the turbine undergo lengthening (creep) due to high centrifugal loads. The rate of creep increases due to high thermal loads in addition to blade loading and, this condition cumulates over time. The second mode of failure is the weakening of the material due to repeated cyclic loading. This is known as fatigue failure. Periodic temperature variations per engine cycle (idle to take-off, cruise, descent, reverse thrust and back to idle) greatly influence fatigue failure. Corrosion is the third mode affecting turbine's durability. Corrosion is also temperature dependant. High surface temperatures allow oxidation to occur and at lower temperatures, the metal experiences sulfidation (corrosion due to condensation of sodium sulphate) [7].

In brief, there are several benefits of increasing the TIT. The consequences of high TIT are also numerous. To curb the consequences, efficient cooling (high heat transfer coefficients) is a necessity. The cooling for turbines is accomplished by directing the compressor bleed air through passages inside the engine to the turbine's internal chambers (or cavities, tubes, and longitudinal holes). It should however be taken into consideration that, if the cooling air is increased alongside TIT, the core power could decrease due to reduced air to burn in the combustor [3]. Hence, to meet the desired metal temperature with high thermodynamic efficiency it is preferred to achieve low coolant-flow rates and reduced mixing losses when coolant is returned to the flow path [6].

1.1   Turbine Cooling

The necessity of turbine cooling was recognized almost from the beginning of the first turbojet engine. By the 1960s turbine cooling was first used in commercial airplane engines [7]. Since then, turbine cooling has had greater emphasis and the cooling technology has evolved significantly. Figure 1-3 illustrates the time-line of cooling development and the TIT achieved respectively. The common cooling techniques used in a GTE are internal convective cooling, film cooling, impingement cooling and transpiration cooling. Combinations of these techniques are commonly used in modern GTE(s).
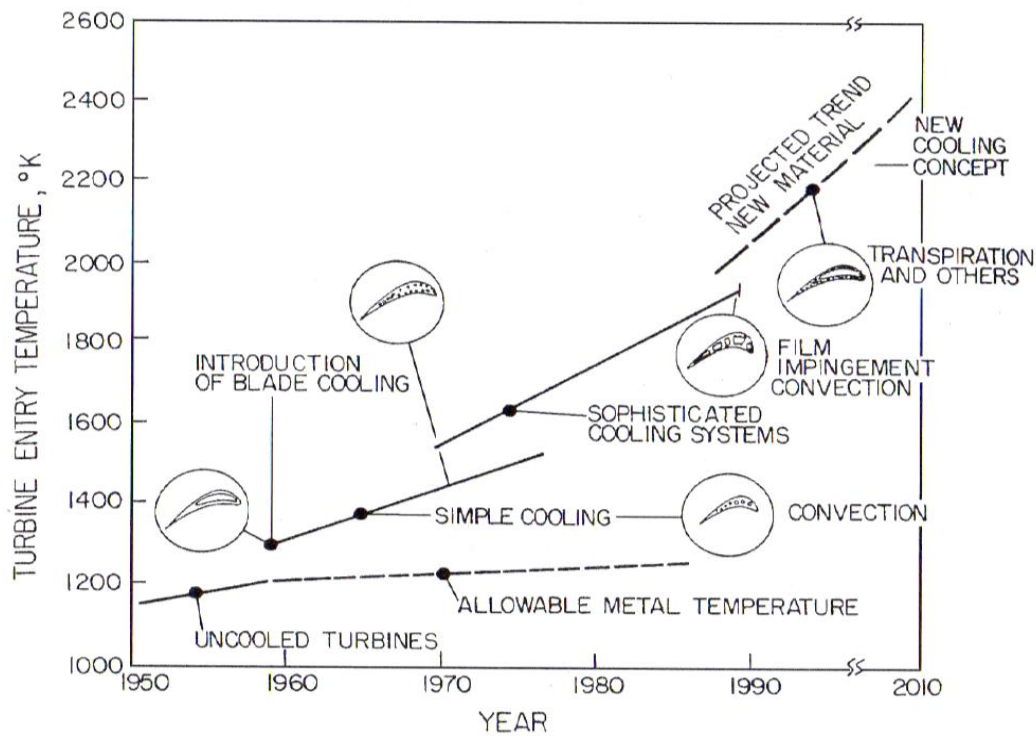
Figure 1-3: Evolution of cooling schemes [1]

Convection cooling is the simplest and one of the earliest techniques used [4]. The effects of convective cooling are amplified by using pin-fins and turbulence promoters. However, due to its limited advantages, film cooling and thermal barrier coating gained a lot of prestige. Film cooling and thermal barrier coating are external methods of cooling turbines. Transpiration cooling is probably the most efficient and effective external cooling method. However, external cooling interferes with the mainstream gas and reduces the aerodynamic efficiency. Furthermore, transpiration cooling is in its early stages of development and is extremely difficult to manufacture and maintain [4].

Amongst all heat transfer enhancement techniques, jet impingement cooling has a substantial potential to achieve high local heat transfer coefficients while maintaining globally, low coolant-flow rates [1]. The high heat fluxes dissipated by an impinging jet on a surface have made this cooling technique not only popular in GTE but also electronic packaging, industrial drying, micro systems and other industrial applications such as annealing of metals and tempering of glass. Jet impingement cooling is an internal turbine cooling method and it is used in locations

4

where the thermal loads are excessively high [1]. Typically, jet impingement is used in combination with external cooling (such as film cooling) in the first stage of high pressure turbine nozzle vanes and blades. It is sometimes used in the second staged high pressure turbine vane and/or blade depending on the engine requirements. By the time the gases reach the next stage (usually low pressure turbine), they have already expanded and enough work has been extracted that the temperatures reach allowable material limits. The interest of current study deals with impingement cooling in a high pressure turbine vane as stated in the section below.

1.2   Thesis Objective and Approach

The purpose of this thesis is to perform parametric analysis of micro-jet impingement cooling in a second staged high pressure turbine vane. Furthermore, the numerical investigation is conducted to better understand the heat transfer characteristics and hydrodynamics of the impinging jets. The modeled second-staged vane is part of the Energy Efficient Engine (E^3) whose studies were conducted by the General Electric Company for NASA. In accomplishing the above-mentioned objective, various minor objectives were also met. For instance, to review the fundamental behavior of two dimensional single jet impingement and apply to single axisymmetric jet impingement cooling, to access different turbulence models, to understand computational management for large jobs and parallel processing of the same and to gain insight to commercially available software for numerical analysis and geometry creation. Various aerospace related software used include: Matlab, Fluent, Gambit, Icem CFD and SolidWorks.

The current study is divided into 7 Chapters. A comprehensive discussion on impingement cooling technique and the flow physics is provided in Chapter 2. The common approach used in discussing the literature review is the bottom-up approach. That is, the thesis starts with analysis of the simplest model possible in terms of impingement: two-dimensional, inviscid, flow on a single jet without the use of a heated model. This type of flow is commonly known as Hiemenz flow. Exact solution of the same exists in literature. Hence, derivation of the same is provided as the analysis. The true model analyzed and discussed is the single, axisymmetric model with viscosity and thermal boundary condition enabled. This parametric analysis was intended to better understand and compare micro impingement jets (0.25 mm) to macro jets (0.5 mm) for gas

5

turbine vane cooling application. The problem on hand consisted of a laminar or turbulent, constant property flow of air via a nozzle jet, impinging onto a target plate at high temperature. The effect of Reynolds number, with effect of change in target to jet spacing and other geometric parameters such as diameter and shape were studied. The numerical investigation was then followed by studying the heat transfer characteristics and hydromechanics in a three dimensional, actual-shaped turbine vane. No concession is made on either the skewness or curvature profile of the airfoil in the streamwise direction, nor to the lean, airfoil twist or tapering of the vane in the spanwise direction. The problem on hand consists of a constant property flow of air via an array of 42 round micro jets impinging onto the inner surface of the airfoil. Here the most important parameter studied is the decrease of jet diameter to micro size (510 μm, 250 μm and 125 μm). Effect of jet inclination (+45° and -45° inclinations) with the cross flow effect are amongst the other parameters studied. Various flow properties are also studied and the advantages and disadvantages are presented as required throughout the text and mainly in Chapter 3. This approach helped gain insight and knowledge to the understanding of flow physics and heat transfer of impinging jets.

The process of numerical computation and validation involves many steps and the Chapters are arranged in this manner as shown in Figure 1-4. The first step is to create a reference model. This is done in Chapter 4. The next step is to mesh the model created and then setup the CFD simulation by applying the necessary boundary conditions; this is presented in Chapter 5. Validation and results are obtained by first solving the flow setup and then post-processing the results. These post processed results are discussed in Chapter 6. This process is repeated for the parametric changes involved and the process/results are consolidated in the respective Chapters.

Figure 1-4: Process followed for numerical computation

1.3 Contributions

At the time of completing the writing of the present thesis, the research held herein has been written into several technical publications. The first such submission was to the CFD society of Canada in 2010. The 18th annual CFD society conference was held at London, Ontario where a paper entitled "Study of Single, Axisymmetric Micro Jet-Impingement Cooling" was presented. This paper focused on the single jet impingement analysis and used transitional to turbulent Reynolds number. Another paper was submitted for publication to the Journal of Heat Transfer Engineering and is awaiting acceptance. More recently, a conference paper was accepted titled "Computational Study of Micro-Jet Impingement Heat Transfer in a High Pressure Turbine Vane". The conference proceedings will be held in Vancouver, British Columbia in 2011. The publisher for this conference is the ASME and the publication is the part of ASME Turbo Expo 2011.

The current study was motivated by extending the success of micro impingement cooling in electronic systems to gas turbine vane cooling application. Computational investigation of hydrodynamic and thermal behavior of single jet impingement cooling in micro scale is presented. Turbulence modeling for single jet with geometric changes of nozzle diameter reduction to micro scale, and shape change to an ellipse is successfully modeled. The reported outcomes from the single jet analysis paved ground for more comprehensive investigation on micro-jet array for impingement cooling of gas turbine vane, also included herein. The high-pressure turbine vane model presents heat transfer characteristics and fluid dynamics in three-dimensional, actual-shaped turbine vane geometry. Effects of jet inclination and diameter reduction to micro scale are also studied.

CHAPTER TWO

FLOW PHYSICS OF IMPINGING JETS

In order to study and understand jet impingement cooling, it is necessary to understand the fluid-dynamics, the relevant flow physics and the heat transfer involved. The first section provides an analytical treatment of impinging jets by reviewing the behaviour of the hydrodynamics of a two-dimensional stagnation point flow without heat transfer involved. The Chapter then progresses to three-dimensional axisymmetric flow with details of flow physics and reasons of heat transfer involved until finally a literature review of the flow in a turbine vane is presented.

2.1   Two-Dimensional Stagnation Point Flow

The first part of this section of the literature review deals with idealized fluid flow, that is, the fluid is inviscid and incompressible. Governing equations are used and exact solution is found to the stagnation point problem. The second part of this section provides the similarity solution to the same problem with viscosity terms involved.

2.1.1   Ideal fluid flow

Exact solution to the stagnation point flow was first analyzed using the Navier-Stokes (N-S) equations by Hiemenz [8]. Such flows are also commonly known as Hiemenz flow. The solution to this problem is based on the potential flow theory. The flow considered may be represented as shown in Figure 2-1. The coordinate system shown has its origin placed at the stagnation point with the horizontal axis along the target plane and the vertical axis being positioned normal to the target plane. The derivation for the potential flow from the governing equation and derivation of the velocity field with stream function is presented in Appendix A. The analytic function of z for the stagnation flow may be described by the complex potential, F(z), in equation (2.1) [8] (see Appendix A for details).
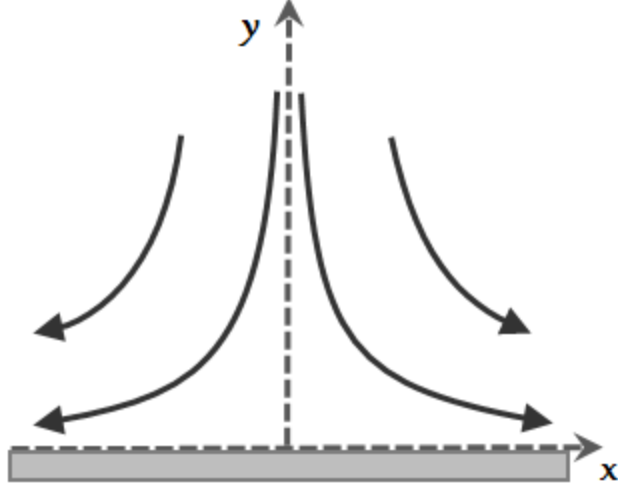
Figure 2-1: 2-D Stagnation point flow

$$F(z) = U_\infty z^2 \tag{2.1}$$

The velocity potential (ϕ) and stream function (ψ) for the complex potential are given below:

$$\left.\begin{aligned} \phi &= U_\infty(x^2 - y^2) \\ \psi &= 2U_\infty xy \end{aligned}\right\} \tag{2.2}$$

and the components of velocity (u and v) for the potential flow are shown in equation (2.3).

$$\left.\begin{aligned} u &= 2U_\infty x \\ v &= -2U_\infty y \end{aligned}\right\} \tag{2.3}$$

The above stream function (equation (2.2)) was plotted using Matlab and is presented in Figure 2-2 (sample script in Appendix B). The direction of the flow is obtained by finding the velocity at particular points using equation (2.3). This direction is also shown in the figure. The free stream velocity was given a value of unity ($U_\infty = 1\,m/s$) for flow visualization. The value of stream function obtained in equation (2.2) is per unit characteristic length. Hence, the unit of stream function is squared meters per second. Also note that the target plate has velocity applied and represents $\psi = 0$ streamline. This value of stream function also holds for the stagnation streamline (streamline at x = 0 in Figure 2-2).

9
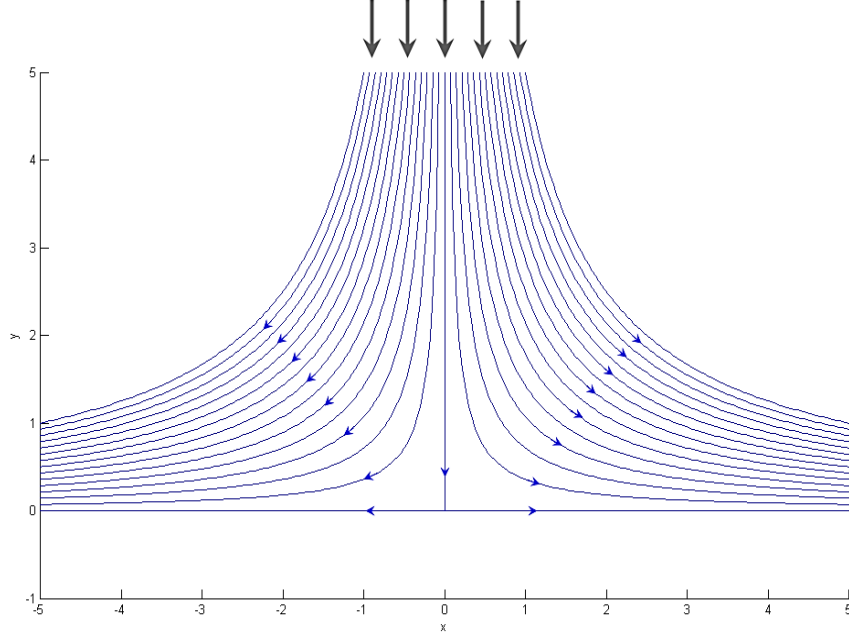
Figure 2-2: Streamlines for Stream function $\psi = 2xy$

2.1.2 Viscous fluid flow

The velocity field in equation (2.3) satisfy the continuity and N-S equation as it was derived using these equations in the appendix section. The assumption made was that the fluid is inviscid and hence the viscous terms were neglected. The flow in the vicinity of the target plate however, is dominant of viscous forces and constitutes a boundary layer. Also, the no slip boundary condition should be satisfied at the wall surfaces. Hence the solution obtained above is not valid within the boundary layer that develops after impingement. For the case of stagnation point flow, Hiemenz attempted to modify the potential-flow field in such a way that meeting this boundary condition would be possible [8]. The derivation for the solution to the flow field, including the effects of viscous forces is presented in Appendix A. The viscous solution is derived from the inviscid potential flow theory mentioned above and substituted in the N-S equation. Then, similarity solution yields the Hiemenz equation, given by equation (2.4). The solution to the third order non-linear ordinary differential equation, equation (2.4), is plotted using Matlab® in Figure 2-3 [9]. The boundary conditions are represented by equation (2.5).

$$\Phi''' + \Phi\Phi'' - (\Phi')^2 + 1 = 0 \tag{2.4}$$

10
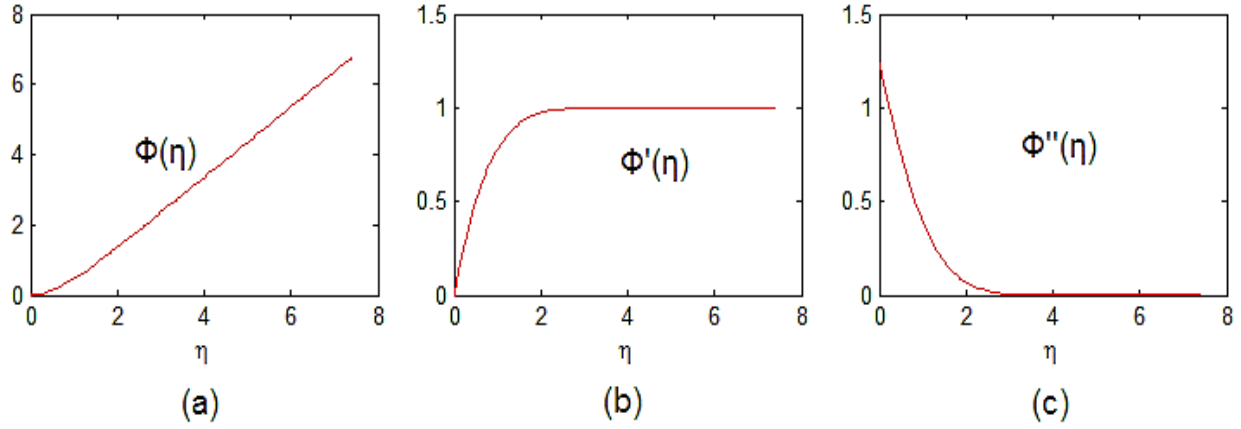
Figure 2-3: Solution to the Heimenz equation (a) $\Phi(\eta)$ (b) $\Phi'(\eta)$ (c) $\Phi''(\eta)$

$$\left.\begin{aligned}\Phi(0) = \Phi'(0) &= 0 \\ \Phi'(\eta) \to 1 \text{ as } \eta &\to \infty\end{aligned}\right\} \tag{2.5}$$

Where, $\eta = \sqrt{2U_\infty y/\nu}$. It is seen from solution of Φ' that solution reaches about 0.99 around η of 2.4. At this point the potential solution is reached. The velocity field for stagnation point flow in two dimensions is given by equation (2.6) [8]:

$$\left.\begin{aligned}u &= 2U_\infty x\Phi' \\ v &= -\sqrt{2U_\infty \nu}\,\Phi\end{aligned}\right\} \tag{2.6}$$

The stream function obtained is provided by equation (2.7) and is compared to inviscid case in Figure 2-4 [10]. Finally, the boundary layer thickness (δ) is given by equation (2.8) [8].

$$\psi = x\Phi(\eta)\sqrt{2U_\infty \nu} \tag{2.7}$$

$$\delta = 2.4\sqrt{\frac{\nu}{2U_\infty}} \tag{2.8}$$

11
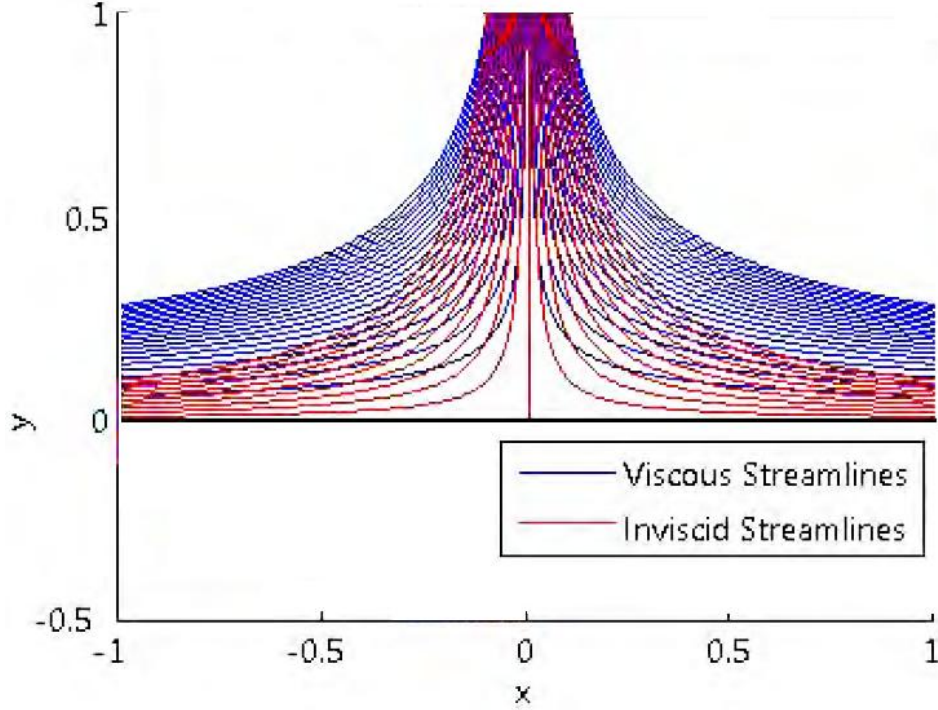
Figure 2-4: Streamlines comparing viscous solution to inviscid solution [10]

2.2 Fluid Dynamics for Axisymmetric Single Impinging Jet

The previous section provided a brief overview to the overall flow structure for an impinging jet in two-dimensions. And for the two-dimensional case, the stagnation point is essentially a line as there is no variation in z direction. Or in other words, the plane may lie at any point in the z-direction. However, in an axisymmetric flow, the flow is in a three-dimensional plane and the stagnation of impinging flow is at a point. This point lies at the axis of symmetry. In the axisymmetric case, cylindrical coordinate system of N-S equations are commonly used and the solution obtained is different than two dimensional case as given below [11]:

$$\Phi''' + 2\Phi\Phi'' - (\Phi')^2 + 1 = 0 \tag{2.9}$$

The flow is subjected to the boundary conditions given by equation (2.5).

The following text provides details of flow physics in two dimensions for an axisymmetric jet, pertaining to single jet impingement inside a turbine vane and the reasons for the high heat

12

transfer rate due to impingement cooling. The working fluid (coolant) in a turbine vane is the compressed air which was bled from the compressor section of the engine. This pressurized coolant mass is impinged onto the internal surface of the vane. Thus, jet impingement cooling may be defined as a high velocity coolant mass ejected from a nozzle or array of nozzles that strikes on the target surface (usually in the perpendicular direction) which is at an elevated temperature and is commonly known as the heat transfer surface [1]. The common impingement nozzles for gas turbine application include circular nozzles and slot nozzles. The impingement nozzle considered for single, axisymmetric jet in the present study has a circular cross-section[2].

Impinging jets may be categorized as submerged jets or un-submerged jets. An un-submerged jet may be defined as a jet which is discharged into a region with a different fluid than the jet itself. For instance, liquid impingement cooling is performed using water as the coolant on boiled eggs in an industrial plant. Here, water is injected into an air filled control volume and impinges onto the surface of the egg shell. On the other hand if air was used as coolant, the jets would be categorized as submerged jets [12]. The case of turbine cooling consists of submerged jet with the coolant being compressed air and the flow physics considered being represented as revealed in Figure 2-5.
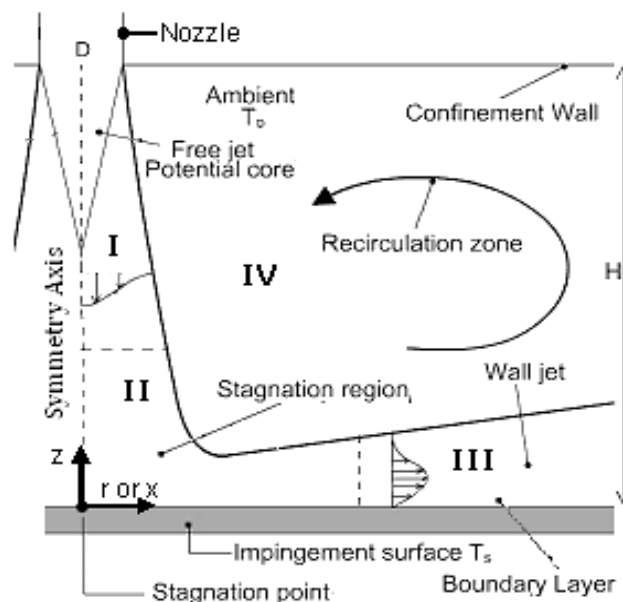
Figure 2-5: Single jet impingement flow physics (modified from original) [13]

---

[2] Parametric analysis was also performed with change in shape of the nozzle to an ellipse for a single jet case.

For cooling the impingement surface, coolant fluid at a high velocity is discharged from a circular nozzle of diameter D. Different regions of flow are seen as a result, marked in roman numerals in the figure. In region I, three zones can be defined: potential core, developing and fully developed zones (Figure 2-6). Typically, the jet exiting the nozzle is turbulent as the Reynolds number (Re) is high, and the velocity profile is uniform [14]. The uniform velocity profile is maintained through the conical section where velocity is at its peak; this regime is known as the potential core. The velocities near the boundary of the jet begin to diminish almost immediately after the jet is discharged due to exchange of momentum to the ambient. This momentum exchange induces mixing and entrainment of air thus expanding the free jet boundary and reducing the potential core. Various experiments have been performed to determine the length of the potential core and the maximum velocity obtained. For a circular jet, with u_m and u_{oc} being the maximum velocity and velocity at the origin of the jet (considered at the nozzle exit) respectively, the ratio of the velocities is found to be given by the expression below [15]:

$$\frac{u_m}{u_{oc}} = \frac{C}{z/D + z_0/D}$$

(2.10)

In equation (2.10), the value of the constant, C determines the length of the potential core. The nominal value of C seems to change from author to author and is dependent on the method of its determination. For instance, in reference [15], Albertson et al. provided a value of 6.2, Cintrini recommended an empirical relationship, Baines claimed that C is a function of Re and that C ranged from 5.0 to 7.0 whereas Abramovich appealed that C is a function of velocity profile; a comprehensive review on values of C and how the experiment was performed is given in reference [15]. One of the interesting facts about potential core length is that it may extend beyond nine diameters long from the nozzle exit location [15]. In case of fully developed axisymmetric jet, completely turbulent flow exists in the potential core.

Downstream of the potential core, the velocity profile tends to develop until it reaches its fully developed stage where the velocity profile is non-uniform over the entire jet cross-section. Here, the maximum velocity is found at the center of the cross-section. This region I, is unaffected by the impinging surface and is known as the free jet [13,14]. In fact, in cases when the impinging

14

surface is only one diameter away from the origin of the jet, neither the mass flux nor the momentum flux is affected through the free jet in question. This was confirmed by the experimental observations of Tani and Komatsu as reported in reference [15]. The velocity distribution of a free jet has a point of inflection and thus is different from a viscous boundary layer [1].
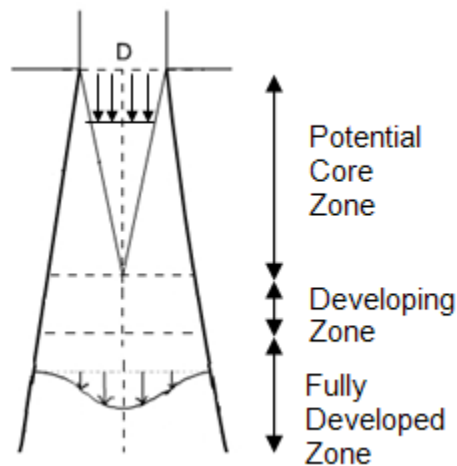
Figure 2-6: Flow region of a free jet

Region II in Figure 2-5 is the stagnation region or impingement region. Here, the oncoming flow is first decelerated, impinged and then accelerated in the radial (r axis) and normal directions (z-axis). The accelerating flow in the normal direction encounters oncoming flow from the nozzle and is the cause for decelerating the flow just before it impinges. The boundary layer in this region is thin and highly turbulent. Also, due to stagnation, convection effects are negligible; however, the stagnation point is inherently unstable and moves around within a bound. Thus, the high momentum coupled with velocity fluctuations is the cause of high heat transfer coefficient around the stagnation region [1]. The centerline turbulence distribution highly determines the heat transfer involved at the stagnation region [16]. The local heat transfer value at the stagnation point reaches a maximum value at the apex of the potential core and reduces if the target is too close to the nozzle or too far away from it. Inside the potential core, the centerline velocity is a constant; however, the stagnation heat transfer reduces as the distance between target and nozzle is reduced. The increase of heat transfer at the apex of potential core is due to the effects of turbulence. This is shown by plotting the velocity fluctuations in the free jet region [16] (Figure

15

2-7). The rate of fluctuation increase is seen in the potential core and is shown in Figure 2-7 (a). The correlation obtained for finding the centerline fluctuations, u', is given below [16]:

$$\frac{u'}{u_{oc}} = 0.84 \left(\frac{z}{D}\right)^{-0.88} \tag{2.11}$$

Also of interest is the observation that the fluctuations increased as the nozzle diameter decreased from 3″ to 1″. Also, the exact solution referred in the previous section can be utilized for the stagnation region.

(a)

(b)
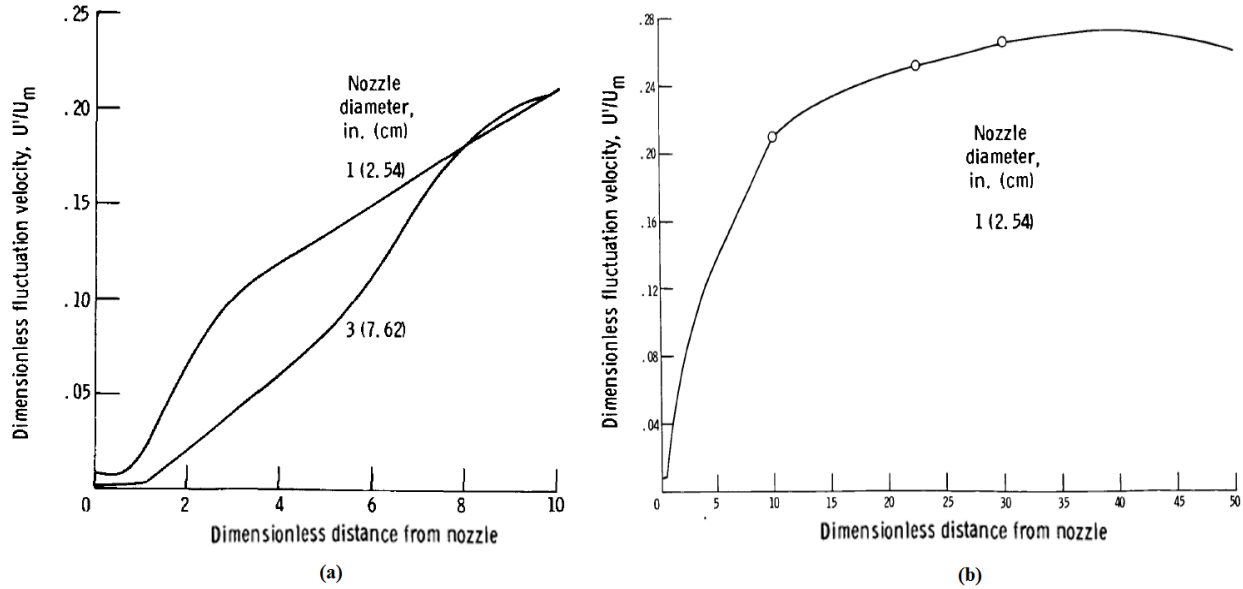
Figure 2-7: Turbulence distribution at jet centerline (a) Potential core region (b) Free jet [16]

In the transverse direction, flow is first accelerated; it reaches its maximum, and then subsequently decays to zero, again due to exchange of momentum and entrainment with the ambient air on one side and due to wall friction (shear stress) on the other. This region is defined as the wall jet and is marked by region III. This region also witnesses developing boundary layers (as shown in section 2.1) and the cooling technique is convective [15]. The maximum velocity achieved is inversely proportional to the radial direction with exponent value of 1.14 [16] implying that the decay of the maximum velocity is faster in wall jet than free jet. Due to a top confinement wall (Figure 2-5), another zone is seen marked as region IV. This confinement

16

allows recirculation of the ambient air due to above mentioned flows types which are capable of producing toroidal vortices.

In general, the geometry of even a single impingement jet is highly complicated and the heat transfer involved is highly dependent on the fluid flow structure. Next section covers impingement study of array of jets inside a high pressure vane.

2.3   Impingement Cooling in Turbine Vanes

The turbines in a modern GTE are of axial-flow design and consist of one or more stages located immediately to the rear of the burner section. A turbine stage consists of a row of nozzle guide vanes called stators and a row of rotating blades called rotors. Typically the first stage or second stage in a multi-spool engine comprises the high pressure turbine; subsequent downstream stages are attached to the low pressure spool. As a result cooling is primarily required in the high pressure turbines. The first component in a turbine stage is the vane and hence the cooling system employed in the first stage high pressure vane is extremely complex. Figure 2-8 shows a schematic configuration of cooling scheme engaged in a first stage nozzle vane [1].
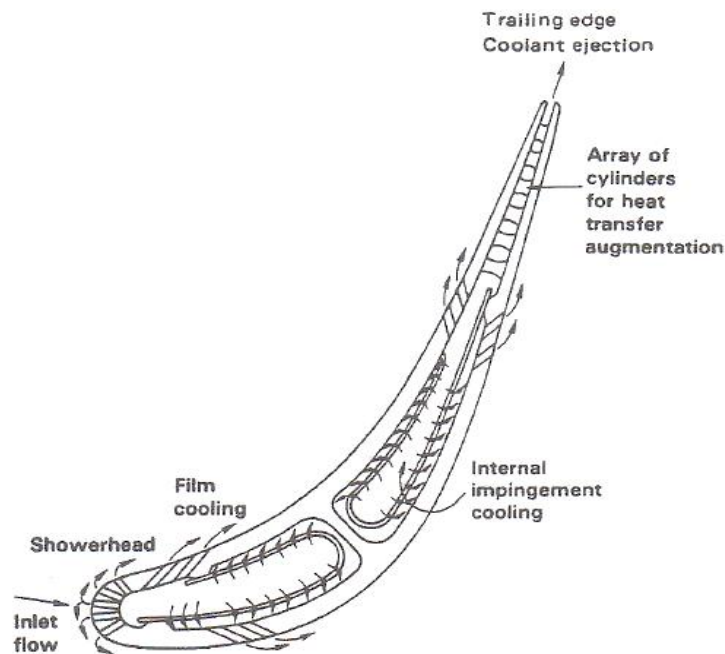
Figure 2-8: First stage turbine guide vane cooling schemes [1]

17

Clearly seen are the various cooling schemes such as film cooling, convective and impingement cooling with turbulence promoters and pin-fins employed in the first stage of turbine vanes. Also, impingement cooling seen above uses two separate impingement inserts in the chambers separated by a rib. An example of the first stage aft-impingement insert used in the Energy Efficient Engine (E^3) is shown in Figure 2-9. The current study however, pertains to parametric analysis of micro-jet impingement cooling only in a high pressure vane. Hence, the model chosen is a second staged NASA-GE E^3 vane where the primary cooling method is impingement cooling by a single impingement insert [6].
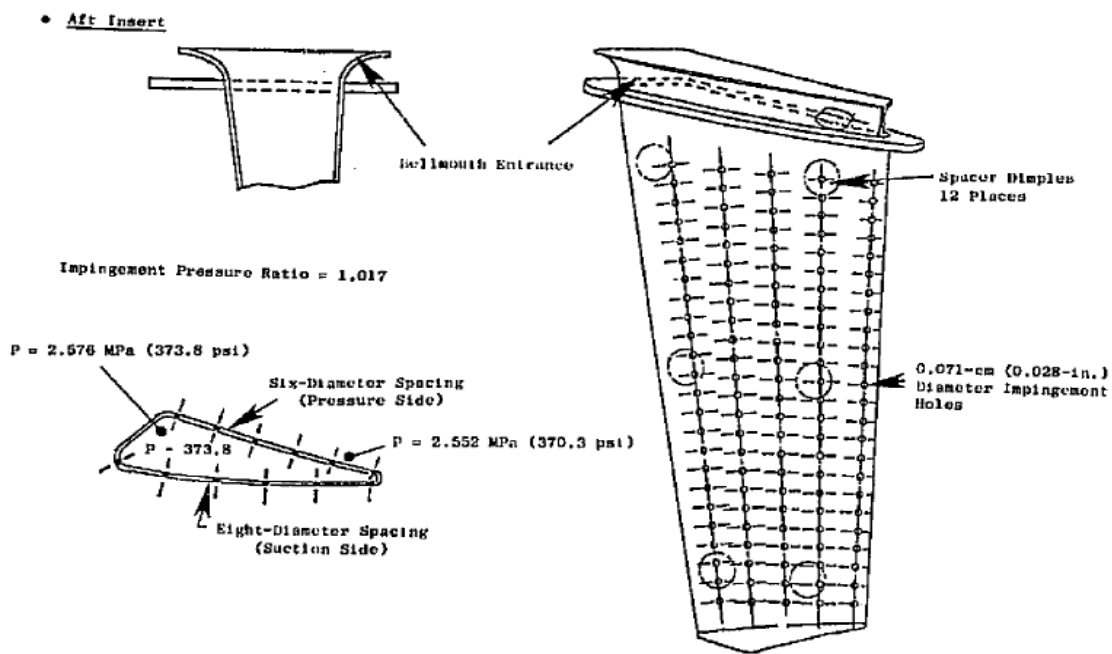
Figure 2-9: First stage vane aft-impingement insert [6]

2.3.1   *Cooling in Second Staged E³ Vane*

The second stage vane does not experience as high heat fluxes as its forward counterpart, and hence, requires only single impingement insert with no film cooling to achieve the desired temperatures. The coolant air enters the impingement insert in the spanwise direction, impinges perpendicularly on the inner airfoil surface, and exits at the trailing edge, effectively cooling the vane. Figure 2-10 shows the flow directions in the single impingement insert.
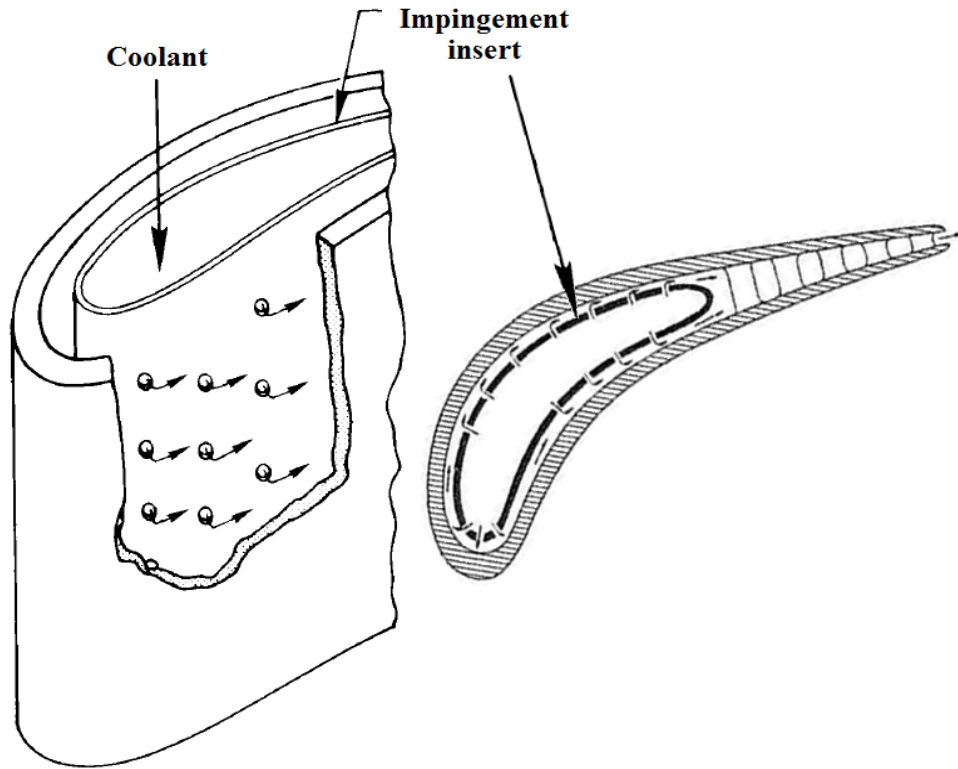
Figure 2-10: Impingement cooling flow directions [1,7]

The stage two cooling bleed air is fed from the seventh stage compressor stator to the turbine vanes. The air enters the casing and flows circumferentially to supply cooling to complete set of stator vanes. The air from the casing enters the impingement insert and is directed towards the engine axis (spool). The designed vane requires 1.85% of mass flow for impingement cooling with holes (jets) of diameter 0.51 mm spaced between 4 and 12 diameters apart [6]. The schematic is presented in Figure 2-11. After impingement 0.75% of the cooling mass is passed to provide purging for the interstage seal, hence reducing losses. The remaining flow exits from the trailing edge bleed slot. The metal bulk temperature is about 1781 °F and maximum temperature experienced is around 2440 °F at 65% span [6].

The spanwise spacing of jets is preferential. That is, the insert is modified by adding extra orifice to the areas where maximum heat load is experienced. Apart from high heat transfer values, preferential cooling is another major advantage of impingement cooling. Typical hole diameter varies for different manufacturers but the hole sizes are usually larger than 0.5 mm [6].
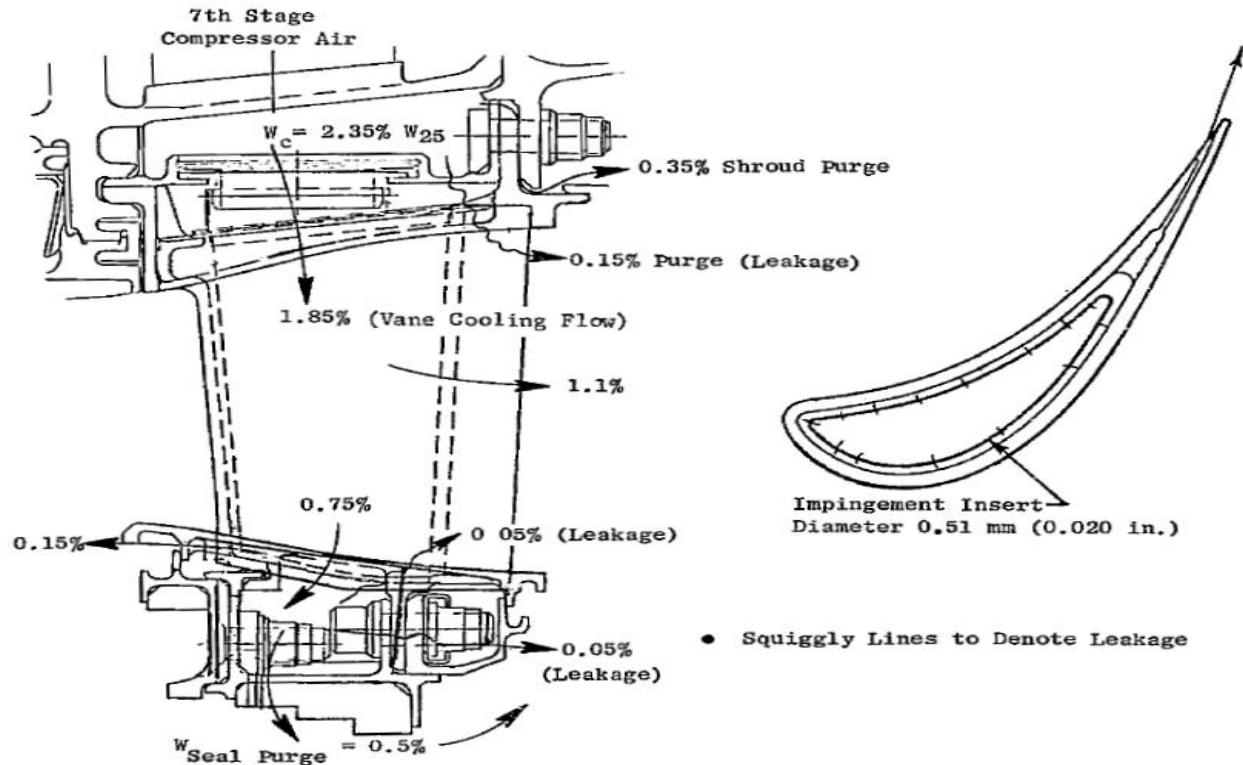
Figure 2-11: Second stage nozzle cooling flow [6]

2.3.2 *Array of Impinging Jets*

Array of jets are used to reduce the excessive localized heat loads on the vane thereby increasing its life and cooling efficiently. A group of jets perform differently from a single jet. The primary contributor to the difference is the cross-flow developed from upstream spent jets. Figure 2-10 shows the cross-flow build up in the streamwise direction. The array of jets can have two configurations, inline configuration and staggered configuration and the impingement surface can be flat or curved. Various experiments involving both configurations (inline and staggered) are present in the literature.

Koopman and Sparrow [17] showed the effect of cross-flow on the array of inline jets and compared the results to single radial jet. It was shown that the oncoming flow rate altered the performance of neighbouring jets. The experimental work of Florschuetz et al. [18] assessed different parameters which affect the cross-flow distribution across the array; a cross-flow to jet mass flow velocity ratio was derived in this model and was seen to be independent of the

20

streamwise spacing of the array (the test model used by Florschuetz et al. [18] is shown in Figure 2-12). However, the ratio was a function of jet to target spacing and the spanwise spacing; the cross-flow experienced by the jets decreases with an increase in any of these functional parameters. The effect of hole spacing was also considered. Results suggested that spacing between holes of 4 to 6 diameters yielded the best heat transfer results. It should be noted that the experimental work in GTE usually models the vane as a flat plate. References [18-21] are a few instances of such work for gas turbine application. Also, most experimental work such as above, penetrate the flow into the nozzle not in normal direction but parallel directions. That is, the inlets are aligned in the direction of jet discharge. This is however not true for inside a turbine vane as presented in section 2.3.1.
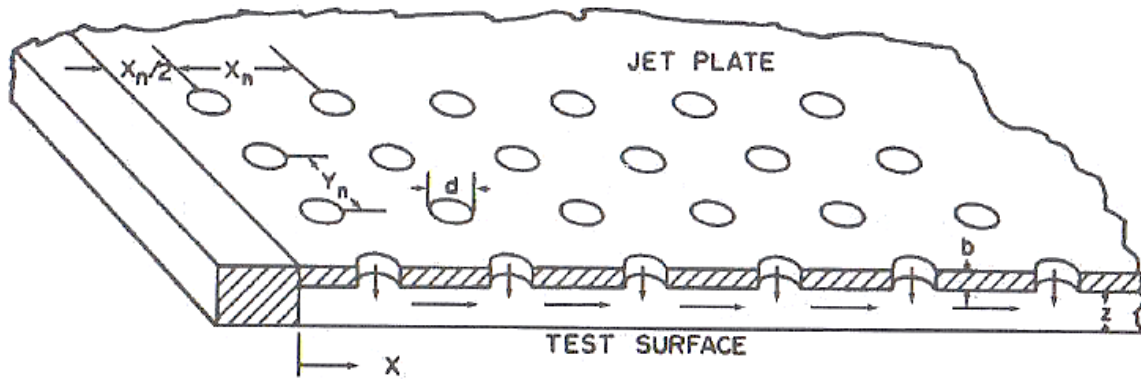
Figure 2-12: Experimental model used by Florschuetz et al. [18]

Staggered array of jets are also studied in literature, however the results suggested that the heat transfer values reduce when compared to inline jets [1]. The reasoning lies in the fact that cross-flow due to spent air is allowed to accelerate as the downstream impinging jet is not present and hence forced convection becomes the medium of heat transfer. The current study focuses on inline impingement jets as they are most commonly used in GTE.

The hydrodynamics of impinging flow from array of nozzles is quite similar to a single jet impingement and shows similar flow regimes: free jet, stagnation zone, wall jet and recirculation zone in case of confinement. In addition, secondary stagnation zones may be seen due smaller spacing between jets. This zone is characterized by boundary layer separation and eddying of flow [22]. The heat transfer under an impinging array is typically resolved in the streamwise

21

direction. Key parameters which influence the heat transfer rate are: the nozzle geometry, the Re, the cross-flow ratio, the streamwise and spanwise spacing, the jet to target spacing, angle of impact and the exit/entrance conditions [22]. Mentioned in Martin's [22] paper is the result obtained by Korger and Krizek in relation to the inclination of jets; the stagnation point was shifted by a length ΔX towards the part of the jet that creates acute angle. Huang et al. [23] performed experimental work in studying inclined jets and found that inclined jets under perform with respect to heat transfer coefficients than straight jets; the supporting argument for reduction in cooling being that cross-flow tends to diffuse the impingement effect. For the case of reducing the jet diameter, experimental analysis was performed by Lee and Lee [24] with micro sized (0.25 mm) nozzle diameter. This analysis was performed with single jet impingement and not an array of jets. The effect of diameter on the local Nu was negligibly small for wall jet region due to impinging flow effects being diminished for r/D > 0.5 (r being the radial direction on the target plate). However, the stagnation heat transfer values were seen to increase by about 30%. This value was obtained for a large jet to target distance. In an experimental setup by Glynn and Murray [25], about 20% to 70% increase was seen in stagnation values when jet diameter was reduced to 1 mm from 1.5 mm. This case also pertains to flat plate with single jet, but with confinement added as opposed to the former case. However, the report presented in reference [15] referred to the work of Hilgeroth, who suggested that of the velocity of jet and spacing between the jets are held constant, heat transfer coefficient increases as the hole diameter increases. Also noticed was that the cross-flow effect interfered with the potential core of the free jet, hence reducing the overall heat transfer.

In analyzing the models considered for the current study, simplifications and various model considerations were taken into account. These not only discuss the simplifications and correlations with respect to heat transfer but also discuss the negative aspects of impingement cooling. The discussion on the same is presented in the subsequent Chapter.

To the best of authors' knowledge, it seems to-date that, most of the work on jet impingement cooling for turbine application is limited to flat plate impingement and that there is no or limited reported study in the open literature on numerical analysis of fully defined 3D turbine vane model with micro jets with the exception of the work of De Paz [26].

22

CHAPTER THREE

MODEL CONSIDERATIONS AND HEAT TRANSFER

The current Chapter first analyzes a single axisymmetric jet impingement cooling and provides model considerations intended to understand micro impingement jets for gas turbine vane cooling application. The second part of the Chapter provides behaviour of array of jets inside a true vane. There are various considerations that need to be acknowledged for analyzing and validating both single jet and array of jets in a turbine vane. These are listed in the following sections.

3.1   Considerations for Axisymmetric Single Jet Impingement

3.1.1   Validity of Continuum Laws

Due to the small diameter of the nozzle, there is an increased probability that the system may deviate from well-established continuum laws. The Knudsen number (K_n) is a dimensionless number defined as the ratio of the molecular mean free path length λ to the characteristic length (nozzle diameter, D, for this case) which provides guidance for deciding whether the continuum laws should be used or not [27]. This is shown in equation (3.1). K_n for jet diameter of 0.5 mm and 0.25 mm are in order of $10^{-5} \approx 0$ for air at 300 K and 1 atm. For $K_n < \sim 10^{-3}$, the continuum approach is considered valid; $0 < K_n < 0.1$ is referred to as slip flow; while, no-slip is captured by $K_n = 0$ [27,28] [3].

$$K_n = \frac{\lambda}{D} \tag{3.1}$$

It was found that the continuum laws are still valid for the model relating to the single jet case, at 250 μm (smallest considered) diameters and jet and ambient temperature of 300 K[4].

---

[3] Please refer to the appendix section for details on sample calculation regarding the same.
[4] Refer to Chapter 5 for boundary and operating conditions used.

3.1.2 Geometric Considerations

The axisymmetric single jet model considered had fully developed flow at the nozzle exit. This was done purely for validation purposes. In cases where fully developed profile is used, the potential core is still valid; however, the length of the potential core diminishes when compared to a profile when the velocity is uniform and maximum throughout the cross-section [15]. Thus, for obtaining the length of the nozzle pipe, the entrance length, L_e, for a fully developed flow in pipes should be calculated. It is seen that the entrance length required for a fully developed flow is a function of only the Re given by equation (3.2) [29].

$$\left.\begin{array}{l}\dfrac{L_e}{D} \approx 0.06\, Re \quad [0 < Re < 2300]\ \ Laminar\ Flow \\[2mm] \dfrac{L_e}{D} \approx 4.4\, Re^{\frac{1}{6}} \qquad [Re > 2300]\ \ Turbulent\ Flow\end{array}\right\} \tag{3.2}$$

3.2   Considerations for High Pressure Turbine Vane

3.2.1 Validity of Continuum Laws

In case of the HPT vane, the plenum pressure, P (explained later in Chapter 4.2) is used for calculation of Knudsen number given by equation (3.1). For air at 500 K and the equation of state, equation (3.3), the mean free path (λ) for air was calculated using equation (3.4), where d is the diameter of air molecule and N_A is the Avogadro's number. The Knudsen number for jet diameter of 125 μm (smallest selected) are in order of ($10^{-5} \approx 0$) at P of ~1.4 MPa. Consequently for the case considered, the regular N-S equation has been used for solving the problem with no slip boundary condition on solid surfaces[5].

$$pV = nRT \tag{3.3}$$

$$\lambda = \frac{RT}{\sqrt{2}\pi d^2 N_A P} \tag{3.4}$$

---

[5] Calculations shows that no slip condition is valid for D ≥ 0.125 mm in both cases (for boundary conditions used in the current model and in true conditions of vane cooling)

3.2.2   *Geometric Considerations*

The flow at the jet exit is determined by the pressure difference between the two chambers (plenum chamber and impingement chamber). The thickness of the insert in the plenum chamber represents the entrance length of the jet. As a result, the flow remains undeveloped and the potential core is longer than seen in single jet impingement case [15].

One of the parameters studied is the reduction in jet diameter. The shortcoming of reducing the diameter is the increased demand for higher pressure head. Since the length of the jet has the same order of magnitude as the diameter of the jet, the jet can be regarded as an orifice flow and the impingement holes in the vane's plenum can be perceived as an orifice plate. When fluid reaches the orifice, it is forced to converge to go through the small hole. The point of maximum convergence actually occurs downstream of the physical orifice (known as vena contracta). The static pressure at the vena contracta decreases to its minimum and the velocity increases to its maximum as the orifice diameter decreases. To meet this requirement, the flow area in the flow passage decreases, thereby increasing blockage as diameter is reduced [30]. The velocity values soon approaches high subsonic Mach number and choked flow condition can be reached in which case extremely high losses are seen and eventually the flow is blocked. The variation of pressure and velocity for an orifice flow is shown in Figure 3-1 [30].

Another consideration or rather concern for small diameter jets is the fact that small jets tend to be expensive to manufacture and may be prone to plugging/blockage [6,31]. Manufacturability of extremely small holes for gas turbine application does exist and is successfully used. Two of the common methods used include the Electro Stream process and the Laser Beam Machining. The Electro Stream process mentioned was developed by GE, where the holes (~0.2 - 1.02 mm) are "drilled" using electrolytic operation. Materials targeted are hardened or tough materials such as 300 series stainless steels, Rene, Inconel, and Hastelloy alloys [32]. The airfoils used in the E^3 second staged vane are made of Rene-150 and the Electro Stream process was used to bore the jet holes [6]. Drilling using Laser Beam Machining is used for cooling holes in jet engine components where even smaller diameters are targeted [32]. Considering blockages/plugging in

the jet holes due to foreign object damage (FOD[6]), various patents have been filed and numerous researches are being performed to protect such blockages, see references [33,34] as examples. All recommendations suggested geometric changes around the inlet to the plenum and cooling passages leading to the insert.
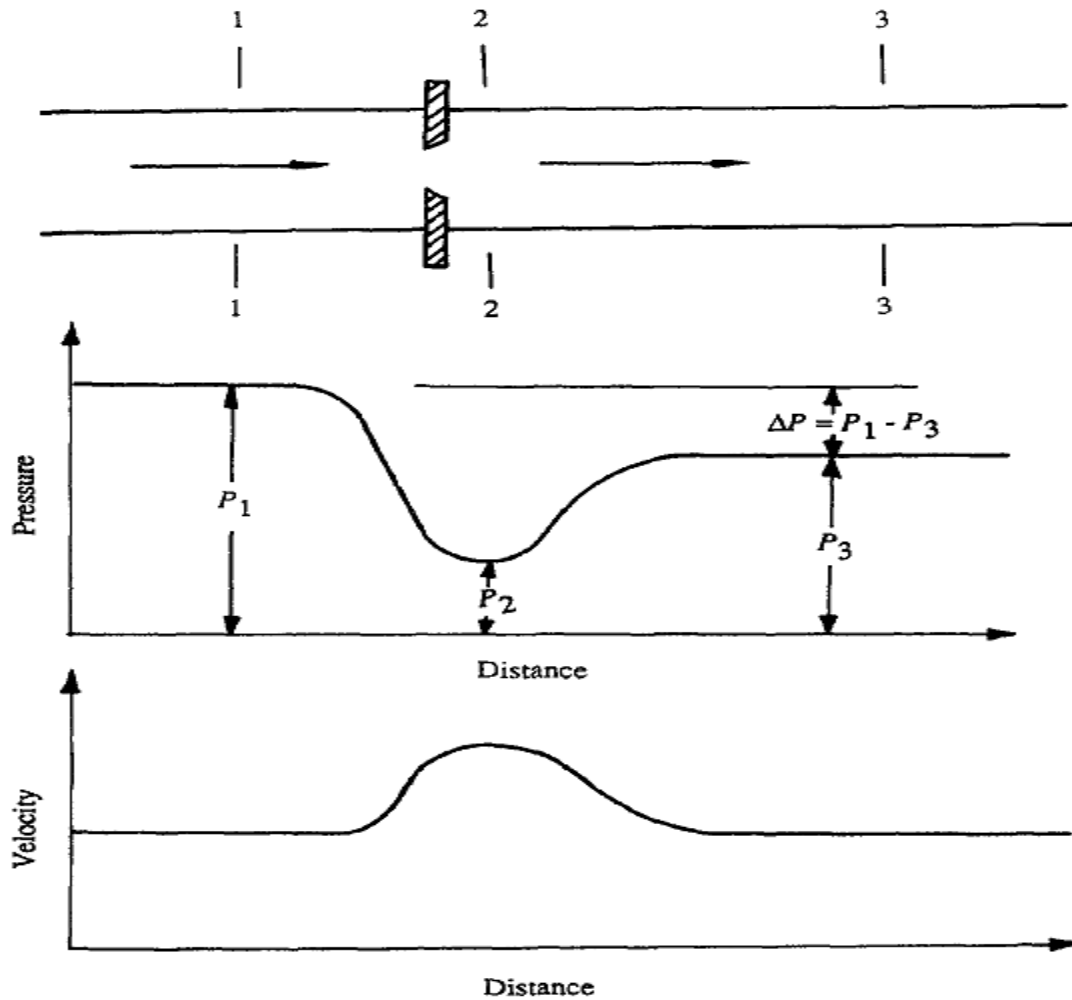
Figure 3-1: Pressure and velocity profiles through an orifice [30]

This paper presents a concept of micro-holes for cooling of gas turbine vanes with the understanding that there are substantial parallel researches on minimizing hole clogging if not eliminating them altogether. The same holds for producing more state of the art manufacturing processes. The focus here is looking into the thermal and hydrodynamic fields of micro-jets. Hence, manufacturing and clogging are not discussed in detail and the paper assesses micro jet

---

[6] FOD is the damage caused by foreign object debris. That is, articles (such as dust particles, sand gains, volcanic ash or any other objects) that are not part of the engine system that has potential to cause a damage.

cooling assuming there is no blockage. Moreover, micro-jet holes-cooling can be used in the future with research advances related to cleaner fuels.

3.3   Heat and Mass Transfer

Since the target surface temperature is greater than the jet stream, there will be convective heat transfer occurring between the two and thus cooling of the target shall be seen as it is at a higher temperature. For evaluation of heat transfer between the fluid and target plate, the convective heat transfer coefficient, h, is defined as:

$$h = \frac{q_s}{T_s - T_j} \tag{3.5}$$

Where, q_s is the heat flux from the surface into the fluid [W/m^2], T_s is the target plate surface temperature and T_j is the temperature of the jet. Also, h has the units of [W/m^{2}K] and the unit for temperature is [K]. To measure the effectiveness of cooling due to impingement, the dimensionless Nusselt number, Nu, is introduced. For single jet impingement case the Nu may be defined as:

$$Nu = \frac{hD}{k} \tag{3.6}$$

Where, k is the thermal conductivity of the jet fluid and D is the jet diameter chosen to be the characteristic length. In case of a turbine vane, the Nu is defined using the characteristic length based on chord length (L_c) of the airfoil at the mid-span as given in equation (3.7)

$$Nu = \frac{hL_c}{k} \tag{3.7}$$

Nu is directly related to the effectiveness, η, of the jet, where the effectiveness of the jet is given by the expression in equation (3.8). Here, T is the local total temperature of the target surface. Throughout the thesis, Nu was modeled as the parameter to show the effectiveness of the jets.

$$\eta = \frac{T_j - T}{T_j - T_s} \tag{3.8}$$

Various correlations have been found and substantial research has been performed in order to model heat transfer under a single impinging jet which can also be applied to the case of array of jets inside a turbine vane. It was seen that the averaged Nu is a function of Re and Prandtl number, Pr as [35]:

$$\overline{Nu} = f(Re, Pr) \tag{3.9}$$

The local Nu is given in the functional form as shown in equation (3.10) [36]

$$Nu = f(Re, H/D, r/D, Pr) \tag{3.10}$$

Where H is the nozzle to target distance and r or x is the transverse distance from stagnation point on the target plate non-dimensionalized by the diameter. However, these correlations do not account for the significant effects of nozzle geometry, jet dissipation temperature, confinement and the generation of turbulence upstream of the jet nozzle. Gardon and Akfirat [37] studied the heat transfer characteristics of two-dimensional and axisymmetric air jets in and around the stagnation point. Similar experimental analysis was performed by Lee and Lee [24] with micro sized (0.25 mm) nozzle diameter for electronic cooling. For a turbulent Re, the stagnation heat transfer was correlated as:

$$Nu_0 = 0.443 Re^{0.565} \left(H/D\right)^{0.0384} \tag{3.11}$$

valid for H/D ratio of 2, 4, 6 and 10. Obot et al. [38] experimented with nozzle geometry and found that the nozzle exit configuration is the most important factor that affects the heat transfer. Furthermore, Lytle and Webb [39] performed experimentation with respect to nozzle to target plate spacing of less than 1D, and found that the local heat transfer substantially increases with

decreasing nozzle to plate spacing unlike for H/D greater than one. Martin [22] provided enormous experimental data for jet impingement over a flat plate. Hoffman [40] extended the results obtained in their experiment to Martin's for the case of micro diameter. The equations are:

$$
\left.\begin{aligned}
Nu &= \Pr^{0.42} \left[Re^3 + 10Re^2 \right]^{0.25} 0.042\, e^{-\frac{0.052r}{D}} \\
\overline{Nu} &= \Pr^{0.42} \left[Re^3 + 10Re^2 \right]^{0.25} \frac{1 - e^{-0.052(r/D)}}{1.24\,(r/D)}
\end{aligned}\right\}
\tag{3.12}
$$

valid for: $3000 < Re < 210000$, $0.5 < H/D < 40$ and $0 < r/D < 70$. Also for H/D < 5, a secondary peak in Nu distribution is observed (see Figure 3-2) mainly associated with increase in the turbulence level in the translational direction and/or formation of vortices in and near stagnation region [14].
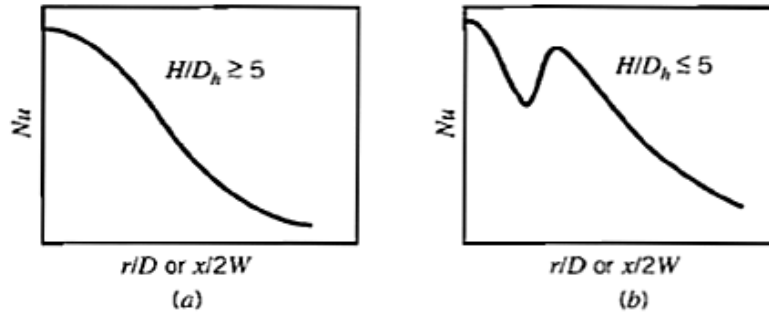
Figure 3-2: Distribution of Nu associated with (a) large and (b) small H/D ratio [14]

CHAPTER FOUR

MODEL GEOMETRY

4.1   Single, Axisymmetric Micro-Jet Model

The problem may be defined as a transition and turbulent, incompressible, constant property flow of air at 300 K via a nozzle jet, impinging onto a target plate. The geometric model is semi-confined and consists of a submerged jet. Figure 4-1 depicts the geometric problem under consideration.
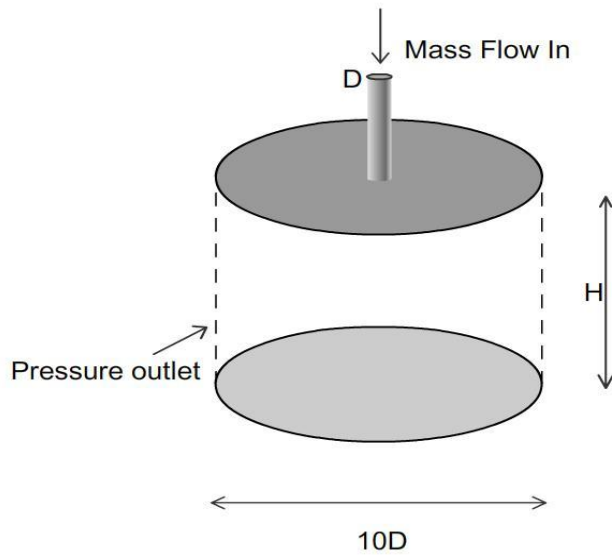
Figure 4-1: Single, axisymmetric impinging micro-jet geometry [13]

The control volume is a 10D×H cylinder. The bottom plate (target) is provided a constant boundary temperature of 600 K. The top confinement wall and nozzle pipe are at ambient temperature while the incoming jet properties are at ambient conditions. The effect of Reynolds number is studied at Re of 2000, 4000 and 6000. The effect of changing the nozzle to target distance is also studied for H/D ratio of 1, 3 and 6. Two cases are initially considered with respect to change in nozzle geometry: one with constant circular nozzle diameter of 0.5 mm and the other 0.25 mm. The shape of the nozzle was later changed to an ellipse with the same hydraulic diameter to further investigate geometric effects. The model with 0.5 mm diameter is used for validation purposes. This model also serves as a baseline case for comparison. As this

paper provides parametric evaluation of heat transfer, equation (3.9) and (3.10) determines the monitoring results.

The geometry was modeled in Gambit; the methodology used was the "top-down" solid modeling approach. That is, the 3D geometry is created by using inbuilt simple geometric volumes and then manipulating them through use of Boolean operations [41]. This method reduces coding needed to automate the process and thus the time required for building the model. Due to the nature of the problem, only quarter of the model (control volume) was modeled (Figure 4-2). The rest of the 3 quarters share symmetric conditions. The simplification of this model is not possible to the two dimensional case as explained in section 2.2.
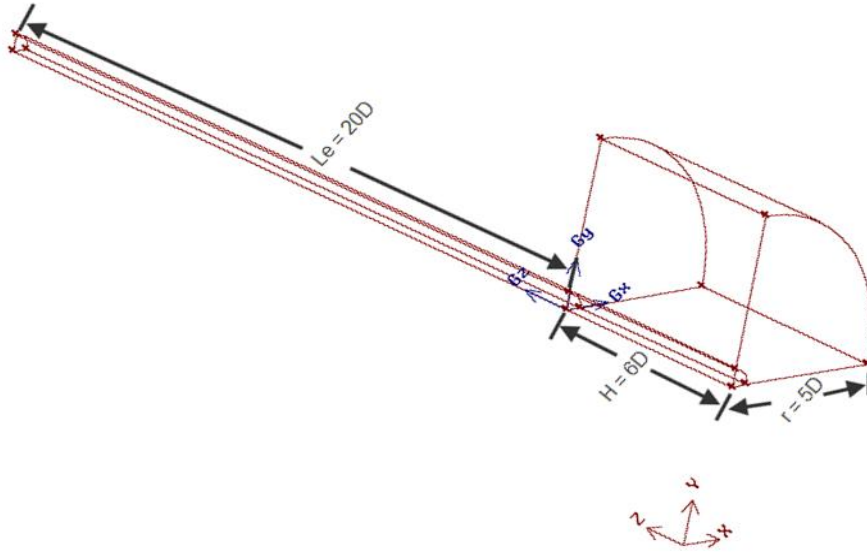
Figure 4-2: Quarter model of the modeled geometry

The model with reduced diameter is not shown as only the diameter of the inlet nozzle was changed to 0.25 mm. For the case with the elliptical model, the hydraulic diameter was kept approximately 0.5 mm and the ellipse was a 2:1 ellipse. The major axis of the ellipse was 0.8 mm wide while the minor axis was 0.4 mm. The area (A), perimeter (P) and the hydraulic diameter (D_H) of the ellipse is given by the equation (4.1) where, 'a' is the semi-major axis and 'b' is the semi-minor axis of the ellipse. The area of the elliptical cross-section of the jet was 0.2513 mm^2 and the perimeter was 1.98 mm. The elliptical model is revealed in Figure 4-3.

$$\left.\begin{array}{l} A \ = \pi ab \\[2mm] P \ \approx \ 2\pi \sqrt{\dfrac{1}{2}\left(a^2 + b^2\right)} \\[2mm] D_H = \dfrac{4A}{P} \end{array}\right\} \qquad (4.1)$$
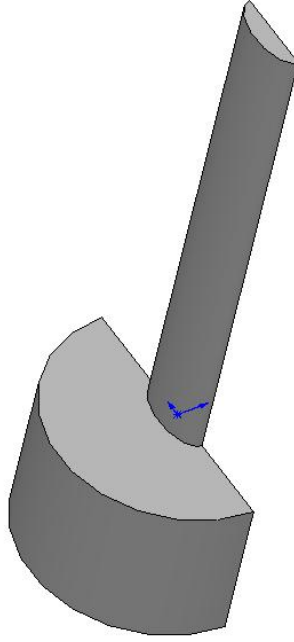
Figure 4-3: Elliptical single jet model

The initial grid sensitivity was established by monitoring $\overline{Nu}$ values for the highest selected Re and a constant Pr. For surety, the local Nu values were used where possible for sensitivity analysis. Parameters that were investigated for obtaining the results include Re and H/D ratio where the diameter is kept a constant and the height is varied. This is done as changing the height and not the diameter of nozzle kept the exit velocity from the nozzle for that Re a constant. The Pr for all cases was kept a constant. Parameters were plotted against r/D for obtaining local Nu results. Parametric analysis included H/D effect for ratios of 6, 3 and 1. The Reynolds effect was also observed for Re of 6000, 4000 and 2000. Alongside, turbulence model selection played a key role for such an analysis, which is also discussed herein. The geometrical model consists of a long entrance pipe for attaining fully developed flow. The length of the pipe was calculated to be approximately 20D for turbulent flows and 120D for laminar flows using equation (3.2)

4.2   High Pressure Turbine Vane Model

The modeled second-staged high-pressure turbine vane is part of the E^3, which was developed by the General Electric Company for NASA. Airfoil coordinates are provided in a report by Timko [42]. Two models were generated in the present investigation, one for validation and other as the base model. The base model was then used for parametric analysis. The vane consists of a single plenum chamber defined by the impingement insert and the design utilizes convection only cooling, making it an excellent choice for the study of impingement cooling in a real vane. The flow considered is incompressible; steady state solution is obtained for flow of air at 500 K impinging on the airfoil surfaces. The holes are 0.51 mm in diameter and an array of 42 jets are studied. The modeled volume spans a total of 12D and consists of three columns of jets; each contains 14 rows of jets: one for leading edge, seven for the pressure surface and remaining for the suction surface cooling. The spanwise spacing between holes was kept at 4D for the base model.

Figure 4-4 depicts the geometric problem under consideration. The model shown is the fluid domain control volume. Air enters in the –Z direction into the plenum chamber, making the blue surface (below) as the inlet boundary. Flow thus moves in the spanwise direction; due to the pressure difference between the two chambers (plenum chamber, shown in blue and impingement chamber, shown in pink in Figure 4-4), air impinges on the airfoil surface via the nozzles coloured in green. The purple arrow shows the direction of the flow from the inlet face. The orange arrow shows the outlet flow. The red arrows show the spanwise and streamwise directions. The arrows within the impingement chamber (pink) show the streamwise cross-flow direction and lastly, the arrows within the plenum chamber (blue) show the impingement flow direction. The other end of the plenum chamber that is opposite to the inlet flow is closed. Also, the jet flow passage is closed on both sides by walls. The arrows show the direction of flow only. After impinging the airfoil surface, the flow is forced to exit at the outlet boundary at the trailing edge of the vane in the streamwise direction. Since all the flow entering the inlet has to exit the outlet to conserve mass, the jet flow consumes flow in its entirety. Figure 4-5 illustrates the flow in the section with transparency. Parameters like nozzle length, L, and jet to target spacing, H, are also defined in the figure.
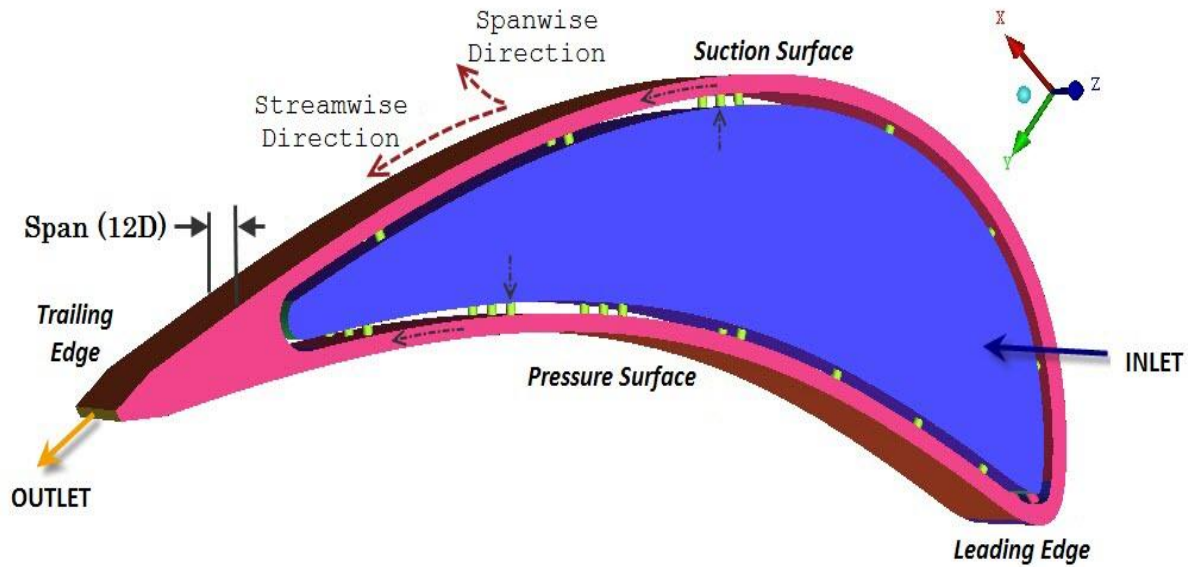
Figure 4-4: Base model geometric configuration

The parametric values chosen for the base model, tested parameters and other geometric reference values used for obtaining the results are provided in Table 4-1 below. The values chosen for span, jet Spacing, L and H are for validation purposes and the values closely mimic true values. The characteristic reference value used is the chord length. Although this length changes locally, the mid span chord length was used as a reference value. Also, this was the reference value used by Leon De Paz [26]; and, the current vane is validated against the same work by Leon De Paz [26].

The difference between the base model and validation model is shown in Figure 4-7 (c) and (b), respectively. The Base model is part of the midsection of the actual vane profile presented in Figure 4-6 (a). The airfoil sections at the different span locations are also shown for clarity (Figure 4-6 (b)). The effect of tapering, skewedness and twisting are noticed when the profile are overlapped in Figure 4-7 (a). In Figure 4-6 and Figure 4-7, the purple arrows show the direction of the flow from the inlet face and the orange arrows show the outlet flow at the trailing edge. Note that the other end of plenum chamber opposite to the inlet flow is closed and is marked as 'wall' in Figure 4-6 (a) and (b).

Table 4-1: Parametric and reference values for the geometry

Span/D	12
L/D	1.05
H/D	1.588
Spanwise Jet spacing/D	4
D[7]	0.51, 0.25 and 0.125 mm
Nozzle Inclination[8]	90°, +45° and -45°
True Vane span	68.326 mm
Reference Chord Length[9], L_c	66 mm
True Taper Ratio	0.98
Meridional Taper Ratio	0.86
Blade lean angle[10] (hub and shroud)	~1°
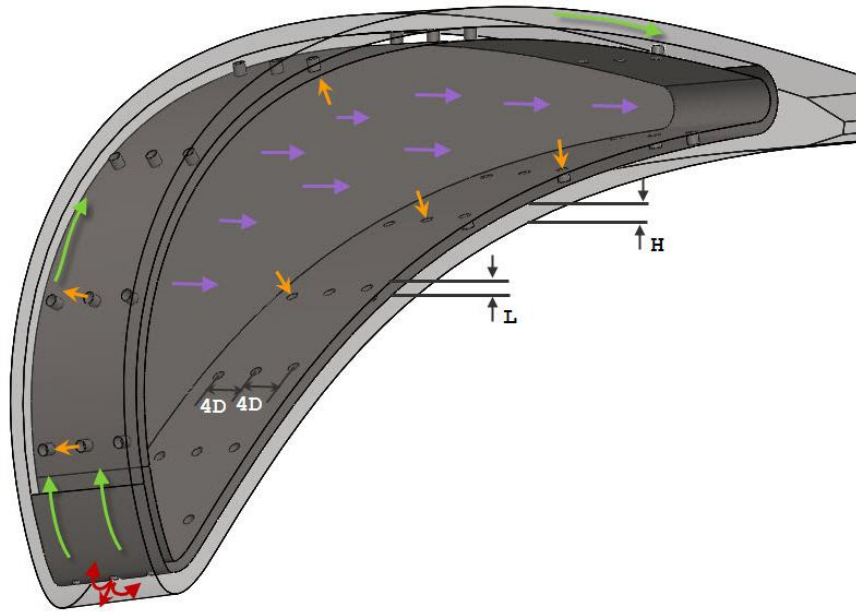
Figure 4-5: Base model showing geometric parameters and flow directions

---

[7] Parameters such as the span, jet spacing, L and H are non-dimensionalized using nozzle diameter of 0.51 mm. These ratios do not change when diameter is varied for testing. See the results Chapter for reasoning.

[8] Inclination angles provided are at nozzle diameter of 0.51 mm

[9] The chord length is measured from leading edge to trailing edge of the outer airfoil surface and not the inner surface

[10] Blade lean angles were defined as the angle between the lines created by joining the hub to tip points at the leading edge to the tangent of the curvature of the leading edge in the spanwise direction.
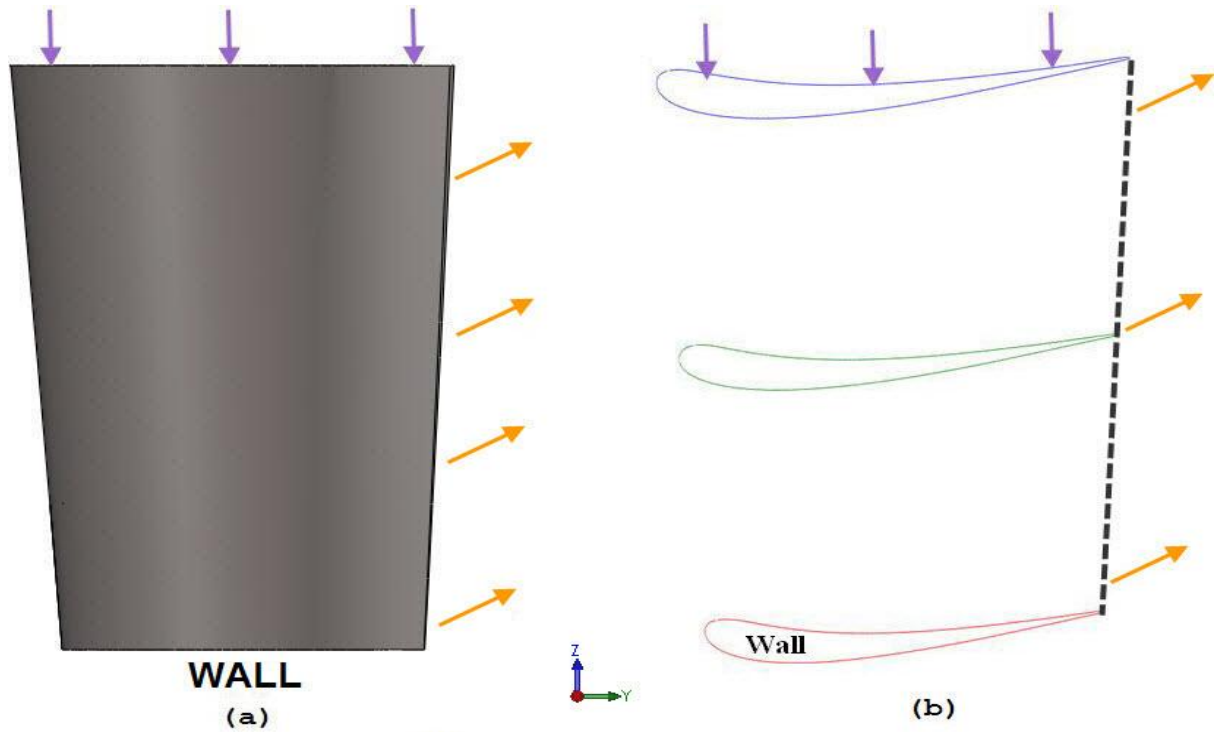
Figure 4-6: (a) Actual vane radial view (b) Corresponding airfoil sections
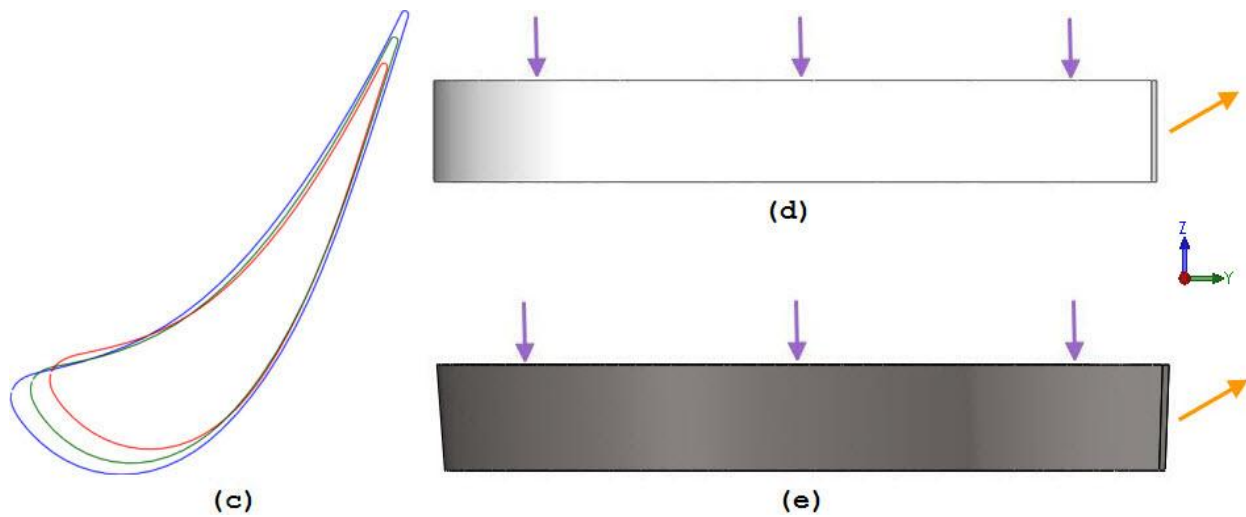
Figure 4-7: (a) Airfoil section overlapped (b) Validation model (c) Base model

The models for inclined jets are displayed in Figure 4-8. The convention defined for the inclination of jets is that, it is positive when the nozzles are aligned in the direction of the streamwise cross-flow build-up from the leading edge. Also, the jets are angled such that the symmetric axis of the inclined nozzle matches the target surface at the same point where the

symmetric axis of the base model did. This would allow for easier comparison between the models. The difference in micro jets are not put on view as the only difference is that the jets are smaller in diameter.
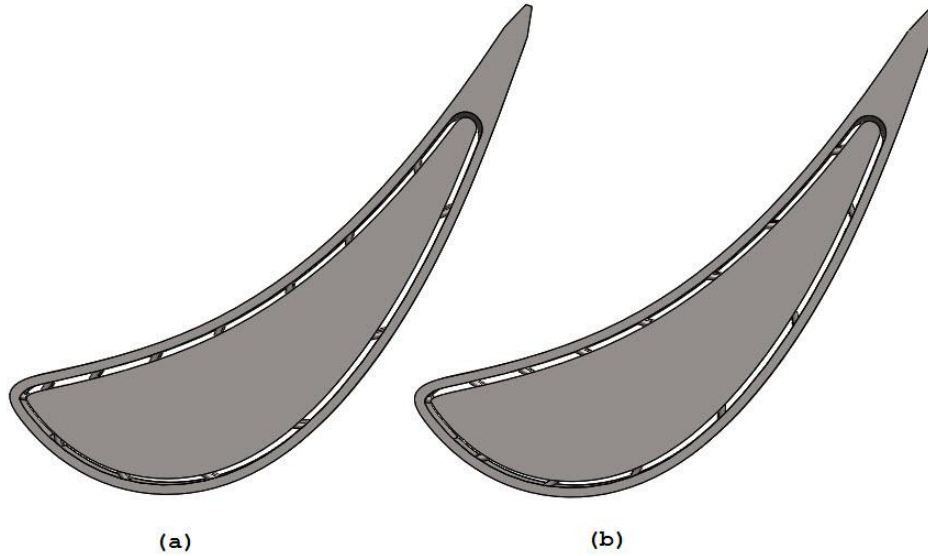
Figure 4-8: Inclined jets at D=0.51 mm (a) +45° (b) -45°

For simplicity, validation and better understanding the nature of impingement heat transfer, the airfoil surfaces (target) are provided with a constant temperature boundary condition. All other walls are kept adiabatic. The airfoil temperature is maintained at 300 K and the impinging fluid is maintained at 500 K. This was mainly done for validation purposes; also, various experimental testing for the same application is performed in this manner; besides, the aim of the paper is to show the effects of heat transfer coefficients, which is independent of the temperature. An added benefit for using such a boundary condition is that the solution convergence issue is avoided [26]. The inlet boundary condition is provided as velocity inlet and is given an inlet velocity of 1.2266 m/s to achieve constant mass flow of 0.003269 kg/s. Fluid properties where changed too; density was changed to behave as incompressible ideal gas due high absolute pressures in the plenum. Constant air properties at 500 K were used otherwise: viscosity at 2.6375×10^{-5} kg/ms, thermal conductivity at 0.040284 W/mK and specific heat value at 1030.305 J/kgK [42,26]. Furthermore, it was assumed that the flow in its entirety exits from the trailing edge and no leakages occur (especially at inter-stage seal).

CHAPTER FIVE

CFD SIMULATION SETUP

The complex flow structure exhibited by impinging jets for the models selected herein can often be difficult to simulate numerically. There are numerous factors that play a significant role in determining the accuracy of the numerical solution obtained including mesh quality, turbulence model selection, the solution technique used and combination of the above to predict excellent results for the model under consideration.

5.1 Single, Axisymmetric Micro-Jet Model

5.1.1 Mesh Creation

Gambit was used for creating the mesh structure for the control volume. The mesh type selected was structured hexahedral with Cooper meshing scheme which has been typically used in many single jet impingement studies [43,44]; whereas, more complicated 3-D models rely on tetrahedral elements with a boundary layer mesh near wall region [45]. The quarter model was divided into three volumes and meshed separately. This was the preferred method of meshing as it was easier to create structured mesh of varying densities in these volumes. The three volumes can be named as the inlet pipe region, the region of intersection when pipe volume is extruded to the bottom plate and lastly the remaining volume. Boundary layer mesh was created near the bottom plate for reduced y^+ values. To capture flow and energy characteristics near the stagnation region and where the flow acted as free jet, the mesh density was increased accordingly. The meshed domain is indicated in Figure 5-1, where the inlet nozzle has not been shown for clarity and mesh is mirrored about the axis of symmetry. Due to the iterative process involved in obtaining good quality mesh a macro code was scripted for program automation and hence time savings. A sample script is available in Appendix B.

The mesh quality was checked in Gambit and the mesh statistics are provided below in Table 5-1. Due to nature of the geometry being round for the 3D case, some skewing is noticed. However, none are in the bad sectors. About 0.3% bad elements were found with respect to the

edge length ratio. This was found in the pipe entrance region and the edges were along the pipe. Thus, the bad sectors are within limits and are acceptable for this section of the geometry.

Table 5-1: Mesh statistics for quarter model H/D = 6

Mesh Measure	% Good Elements	% Bad Element	
Equi-Angle Skew	91.72	0.00	
Edge Length Ratio	71.17	0.28	at pipe region
Volume	100	0.00	
Mesh Size	~$180,000$ nodes		
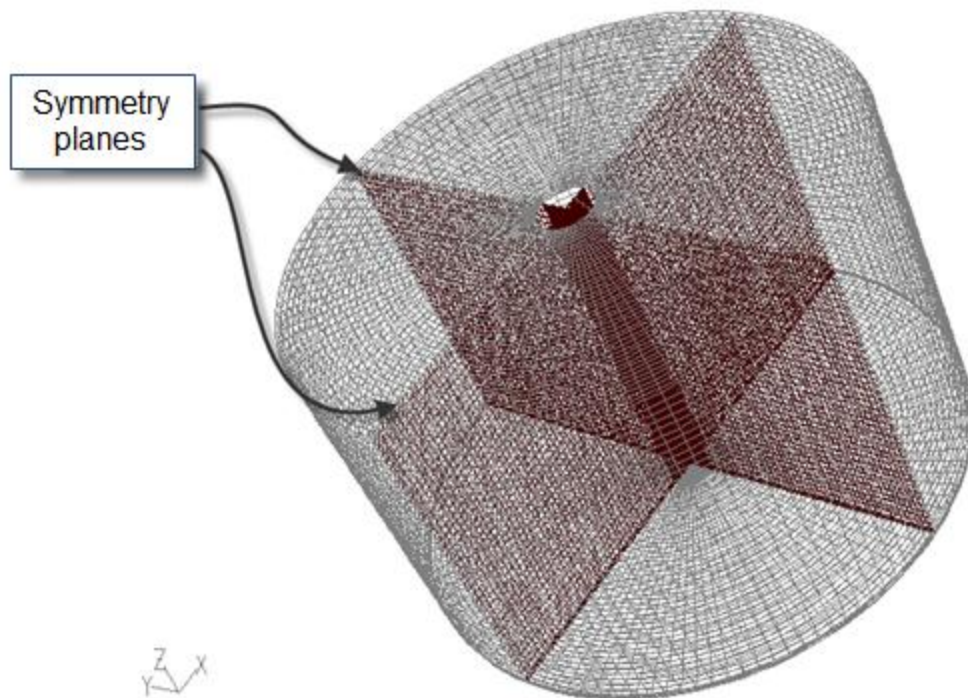
Figure 5-1: Sample mesh for quarter model at H/D=6

5.1.2   Simulation Technique

CFD simulation was conducted in Fluent. The boundary conditions for wall and fluid have been mentioned previously. The domain definitions are tabulated in Table 5-2. The relaxation parameters were tweaked (over-relaxed) for faster convergence for initial solution and then

under-relaxed for forcing convergence when using higher order discretization. SIMPLE algorithm was used for pressure-velocity coupling on staggered grid for solving the N-S equation. Upwind scheme was used to discretize the N-S equation to prevent wiggles in the solution obtained (when compared to other schemes); also, this scheme keeps the coefficient matrix as diagonally dominant and positive; hence, maintaining numerical stability and physically realistic flows [46]. The spatial accuracy of the upwind scheme was later improved by choosing second order upwind for momentum and energy equations. The scheme was maintained for all cases, although the second order upwind might benefit from higher Re as the scheme is less diffusive compared to first-order upwind scheme.

Table 5-2: Component and physics definition

Simulation Type	Steady State
Formulations	Implicit
Heat Transfer	Total Energy
Boundary Template	Velocity Inlet; Pressure Outlet
Solver	Segregated (Pressure Based)

At the inlet section, with boundary type of velocity inlet, the magnitude of inlet velocity is case specific and is calculated using the Re number based on diameter where, μ is the viscosity and ρ is the density as:

$$V = \frac{\mu Re}{\rho D} \tag{5.1}$$

The fluid properties used at 300 K are tabulated below in Table 5-3 for reference. In case where compressibility effects cannot be ignored and the flow cannot be accurately predicted (convergence is affected), the boundary condition was changed to "Pressure Inlet" where the dynamic head along with prevailing static pressure conditions provided the total pressure. The inlet condition could also be specified as mass flow inlet. Assuming that the density change is not dominant as the flow condition is low-subsonic and no work is being done on the fluid, the

kinetic energy is given by $\frac{1}{2}\rho V^2$. This boundary condition is added with incompressible ideal gas equation suitable for low Mach number flows [46]. The convergence criteria was set such that the residual was targeted to 10^{-4} for all equations except energy equation, which was targeted to 10^{-6} as used by Leon De Paz [13]. This was not the absolute convergence criteria, but the minimum threshold requirement. In addition to the residual convergence check, convergence criterion was determined by monitoring mass averaged surface monitor variables (for instance, total pressure and velocity at nozzle exit) against iterations. Indifference of the magnitude of the variables against iterations represented convergence.

Table 5-3: Fluid Properties at 300 K

Density, $\rho\ \left[\frac{kg}{m^3}\right]$	1.225
Specific Heat, $C_p\ \left[\frac{J}{kg \cdot K}\right]$	1006.43
Thermal Conductivity, $k\ \left[\frac{W}{m \cdot K}\right]$	0.0242
Viscosity, $\mu\ \left[\frac{kg}{m \cdot s}\right]$	1.789×10^{-5}

5.1.3 Turbulence Modeling and Mesh Sensitivity

Various studies have been dedicated to modeling turbulence; selecting a turbulence model greatly determines how accurate the solution to the problem can be predicted. An extremely meagre jet impingement case preferred the use of one-equation turbulence model; two-equation models have been successfully applied for such designs. Amongst the two-equation models, it was found that for the standard k-ε model, excessive kinetic energy prediction at stagnation region was a disadvantage. Similar over prediction (about 300% at stagnation) was seen by Ashforth-Frost and Jambunathan [47]. In addition, this model was perceived to be incapable of predicting near wall flows.

The best reported turbulence model was the v^2-f model [48]; however, the accuracy was achieved at a higher computational cost. To achieve good accuracy with considerable computational cost, modifications to existing two-equation models were incorporated such as the Yap correction

factor by Craft et al. [49]. Low-Re turbulence models were also tested with better prediction results for stagnation region but over prediction at downstream region from stagnation point. Various sorts of low-Re k-ε model have been tested by Wang and Mujumdar [50]. When Yap correction was applied to low-Re turbulence model, it was seen that for both regions, near wall and stagnation region, the prediction improved. RNG model was seen to agree better than standard or low-Re k-ε model for impinging jets by Shuja et al. [51]. Additionally, it was pointed out by Isman et al. [48] that the turbulence intensity is an important parameter that affects heat transfer rate. Under prediction of stagnation values was reported by Leon De Paz and Jubran [13] and Angioletti et al. [44] for the k-ω turbulence model family. Results for standard k-ω model by Abdon and Sunden [52] saw over prediction again at stagnation; it also saw misplaced secondary peak in case of non-confined jet impingement. Tzeng et al. [53] pointed out that the prediction accuracy of a model depends on the grid distribution (density), application of the model and the numerical scheme used in spatial discretization. Hybrid models such as Menter's SST model have also been successful due to the presence of the blending function between k-ω and k-ε models [54]. A preliminary comparison chart of turbulence model for the current application is presented below in Table 5-4.

Table 5-4: Comparison of turbulence models for single jet impingement

Turbulence Model	Computational Cost	Heat transfer coefficient error prediction
Standard $k - \epsilon$	Low	Poor: $15 - 60\%$
Low Re $k - \epsilon$	Low-Moderate	Good: $10 - 30\%$
Standard $k - \epsilon$ RSM	Low	Poor: $15 - 60\%$
Alternate $k - \epsilon$ RSM models	Low-Moderate	Fair: $10 - 45\%$
$k - \epsilon$ RNG	Low	Fair: $20 - 35\%$
Standard $k - \omega$	Low-Moderate	Poor : $15 - 60\%$
Low Re $k - \omega$	Moderate	Good: $10 - 30\%$
SST	Moderate	Fair: stagnation Nu error: $20 - 40\%$
$v^2 - f$ model	High	Excellent: $2 - 30\%$
DNS/LES	Extremely High	Excellent

Thus, from the various turbulence models proposed, the k-ε RNG model, low-Re k-ε model (Lam-Bremhorst model), k-ω SST model and RSM model were chosen for testing the current case. This decision was based on the trade-off between computational cost and numerical accuracy. Different turbulence models become insensitive to grids at different mesh sizes. Hence, independent sensitivity analysis was performed for each turbulence model separately[11]. For reduced convergence time, solution from previous model was mapped for evaluation of new turbulence model. For comparison, experimental work of Angioletti et al. [44] and numerical work of Leon De Paz and Jubran [13] is used with Re = 4000 and H/D = 4.5, as shown in Figure 5-2.
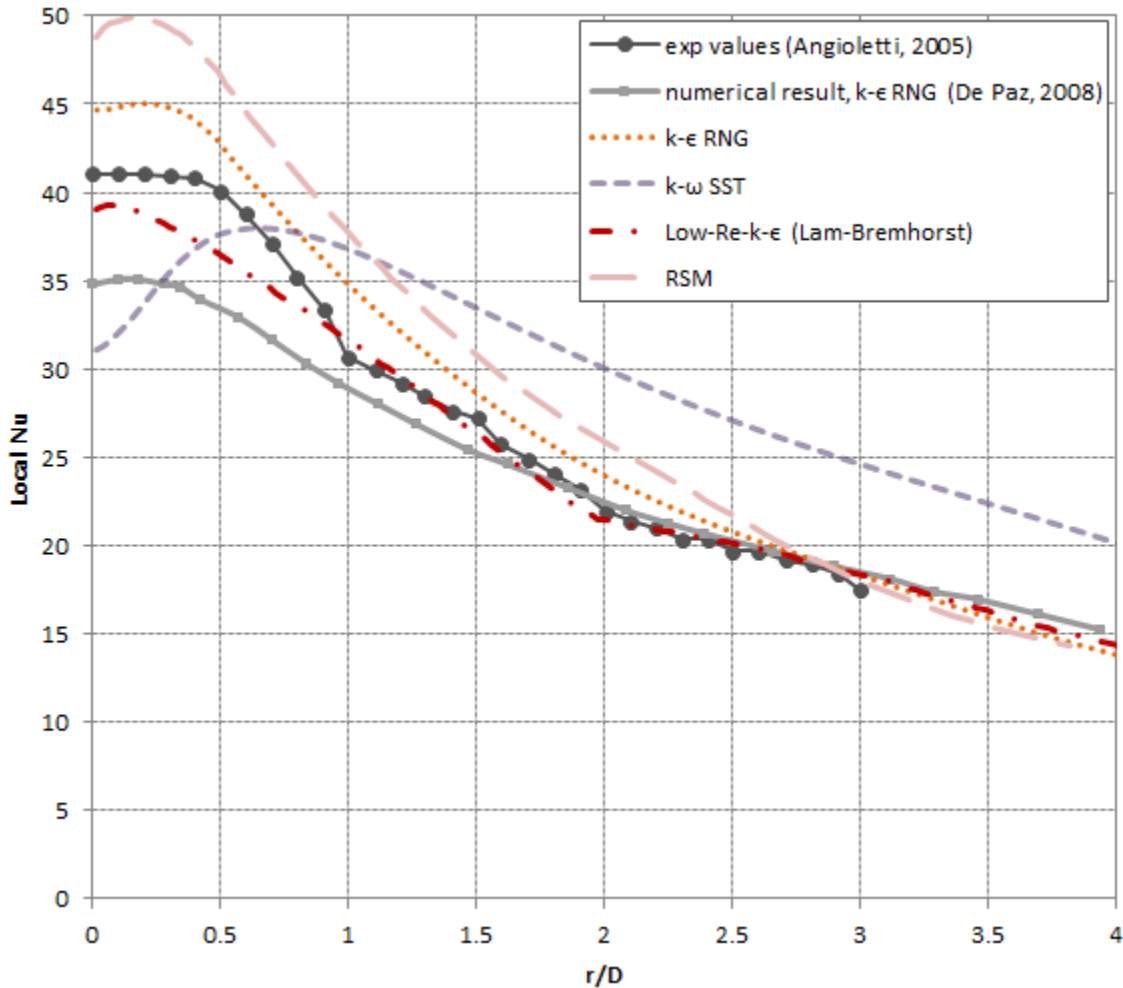
Figure 5-2: Turbulence modeling. Local Nu distribution

---

[11] Sensitivity analysis was first performed for the selected turbulence models.

The figure indicates that the best turbulence model was the low-Re k-ε Lam-Bremhorst model. This model is used hereon for parametric analysis of single impinging jet. The stagnation value for the low-Re model was 5.25% off the experimental Nu value whereas the average up to r/D of 3 bore 1.95% error. The k-ε RNG model over predicts the stagnation values as disclosed in the figure. This may be attributed to excessive kinetic energy prediction as mentioned above [47]. It should however be noted that the low-Re model required finer meshing when compared to standard k-ε model for achieving mesh independence.

The inlet turbulence intensity plays an important role in determining the turbulent flow characteristics and hence the heat transfer involved. In fact, it has been observed that the turbulence intensity has a major and direct effect on the heat flux and thus the Nu values obtained especially at stagnation. According to Jambunathan [36], an increase of about 0.5 to 3.2% in the axial turbulence intensity at Re 6000 and r/D of 2 increases the Nu value at stagnation point by an absolute difference of 35 or about 19.5% increase. Hence, erroneous results will be introduced if the boundary conditions are not changed accordingly. The turbulence intensity (I) for internal flow based on hydraulic diameter is given in equation (5.2) below [55]:

$$I = 0.16 \times Re^{-1/8} \tag{5.2}$$

The hydraulic diameter may be calculated using the following equation:

$$D_H = \frac{4 \times Area}{Perimeter} \tag{5.3}$$

Where, the area of interest is the cross-sectional area. Grid sensitivity analysis was performed with the low-Re turbulence model on Re = 6000 (highest selected Re) and H/D = 6. This is because the error is expected to grow with increasing Re as the non-linear convective terms in the N-S equation become dominant. Initially a coarse mesh was created and then refined by a factor of 1.2 as grid spacing in Gambit. The mesh independence was checked with $\overline{Nu}$ and Nu values. The $\overline{Nu}$ values for three grids were 21.55, 22.95 and 23.29 respectively. Any refinement hereafter did not produce significant improvement when compared to increase in computational

44

time. Hence, a fine mesh was used. The maximum y^+ value was kept within 5 as Fluent uses blending linear and logarithmic laws-of-the-wall using the function suggested by Kader (for the turbulence and viscous model selected) [55], which extends correct asymptotic behaviour for large and small values of y^+. For a reasonable representation of velocity profiles, it was suggested to maintain $3 < y^+ < 10$ [55].

To speed the long runtime for model creation, CFD setup, solving and post-processing results, macro scripts were written to support the iterative process as discussed before. Time reduction in terms of solving the N-S equation was performed by parallel computing of the computational grid at High Performance Computing Virtual Laboratory clusters. The time to convergence was monitored and plotted against grid node counts for different number of processors (Figure 5-3). This provided an efficient environment of solving the moderately loaded mesh count. An almost linear time reduction was seen until a maximum of 8 CPUs for the finest grid used. No more processors were used to maintain good accuracy in the results obtained.
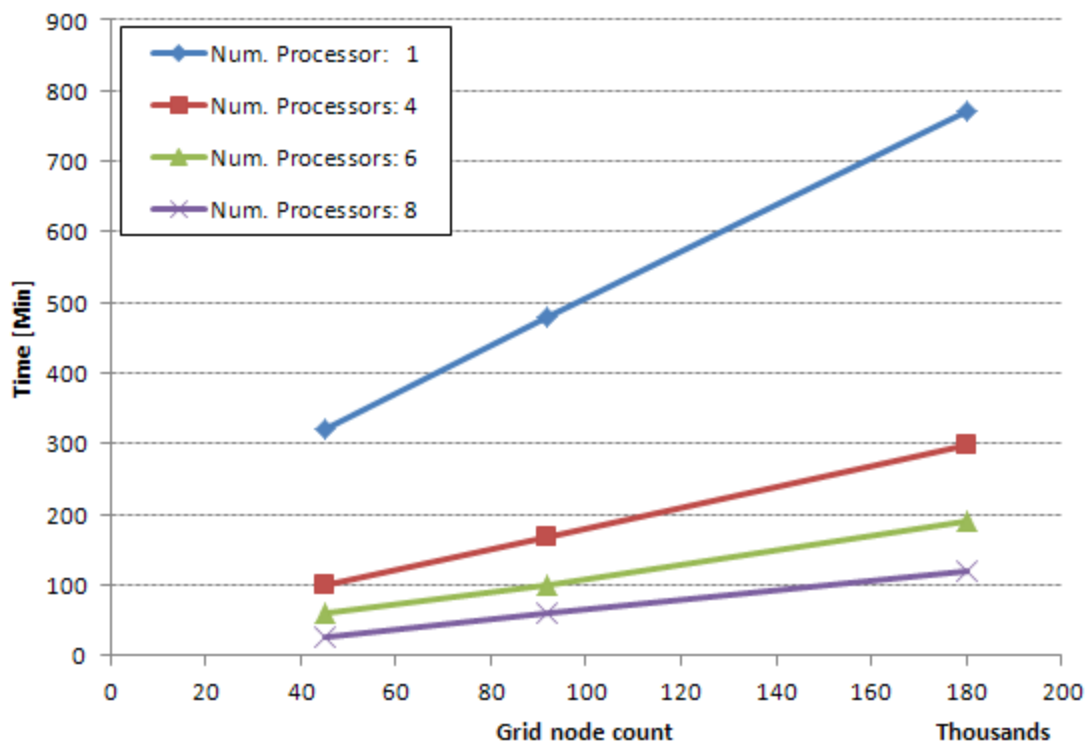
Figure 5-3: CFD solver performance

5.2   High Pressure Turbine Vane Model

5.2.1   Mesh Creation

The control volume presented in section 4.2 was modeled in SolidWorks and the meshing was performed in ICEM-CFD. The current study uses true three dimensional vane profiles with flow entering the plenum in the spanwise direction and flow impinging orthonormal to this direction. As a result, no concession is made on either the skewness or curvature profile of the airfoil in the streamwise direction, nor to the lean, airfoil twist or tapering of the vane in the spanwise direction. However, the model was truncated in the spanwise direction for validation purposes.

Due to the complex geometry modeled, unstructured tetrahedral mesh structure is the preferred meshing routine [45]. Using tetrahedral mesh structure as opposed to hexahedral mesh structure implies that the grid density has to increase tremendously to capture the flow structure and obtain a good solution. This further implies that the time to compute increases. As a solution, the fluid domain was filled with a conformal unstructured hybrid mesh; that is, tetrahedral mesh structure on all surfaces and volumes with hexahedral core and prism boundary layer on the target surfaces. The volumes were split into three with plenum acting as reservoir, the jets and the impingement region. The jet inlet and outlet surfaces were provided as interior surface for the flow to pass through. Different mesh densities were used based on importance of the location. Boundary layer mesh was maintained at target surfaces only as shown in Figure 5-4.
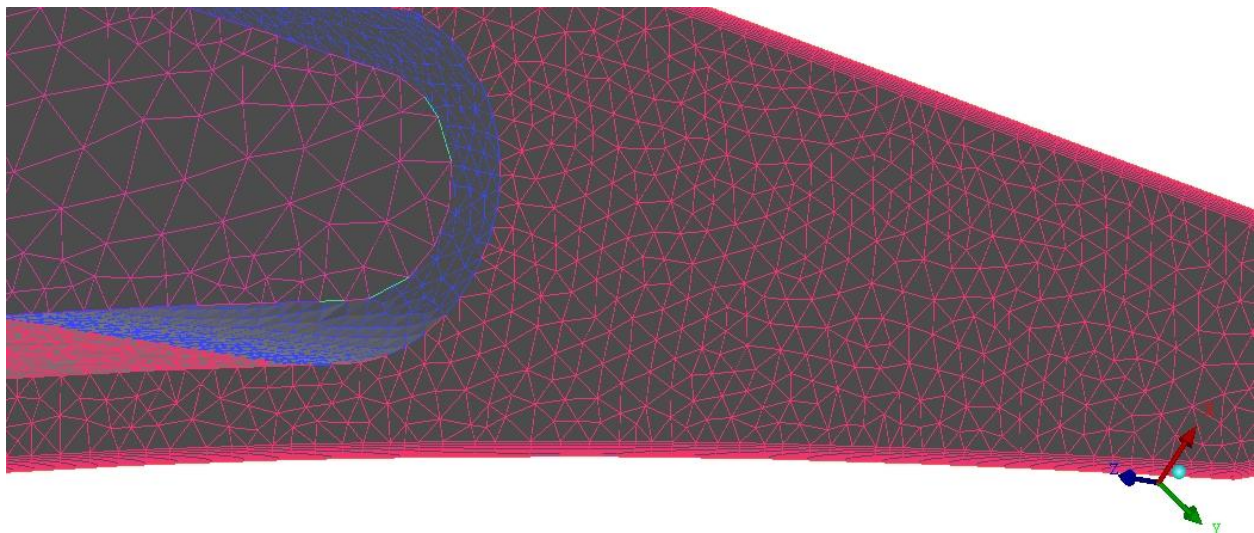
Figure 5-4: Boundary layer mesh with surface mesh

The meshed structure for the entire domain for base model is shown in Figure 5-5. A prism boundary layer was created making the model a hybrid. However, this does not reduce the mesh count. The plenum mesh was truly made hybrid to reduce on time taken for solving. The hexahedral core structure in the plenum cut down the mesh by roughly 60%. A cut plane through the model is revealed in Figure 5-6 and Figure 5-7 showing the hybrid mesh.

The mesh structure remained the same for all tests. The mesh size was changed appropriately confirming mesh independence for all cases tested. The mesh size was approximately 355,000 for the intermediate case with D = 0.51 mm. The average Y^+ was maintained around 2.5 and the max recorded Y^+ was 4.83 near the trailing edge. The maximum y^+ value was kept within 5 enabling the use of enhanced wall functions for the mainly turbulent boundary layer at impingement region and allowing blending functions for regions with higher Y^+ value; for instance, the max recorded Y^+. For a reasonable representation of velocity profiles, it was suggested to maintain Y^+ within five [55]. The mesh statistics was also examined in ICEM-CFD and the mesh quality was checked. The worst element was kept above 40% quality level as recommended by Ansys ICEM for all mesh types selected [56].
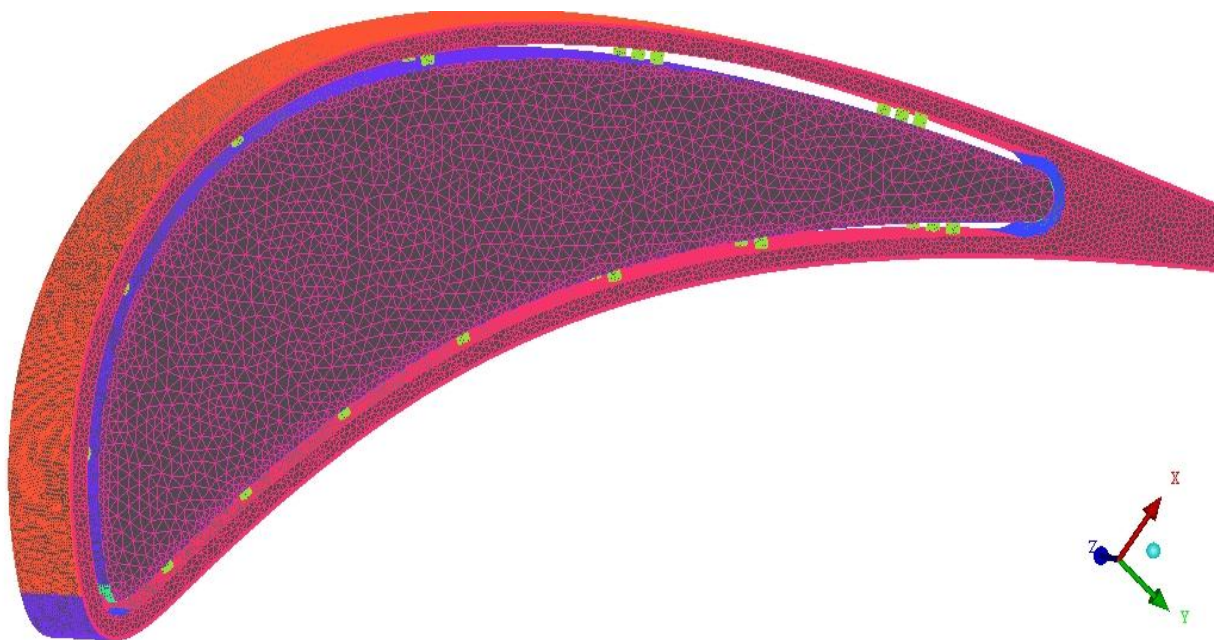
Figure 5-5: Mesh structure for base model
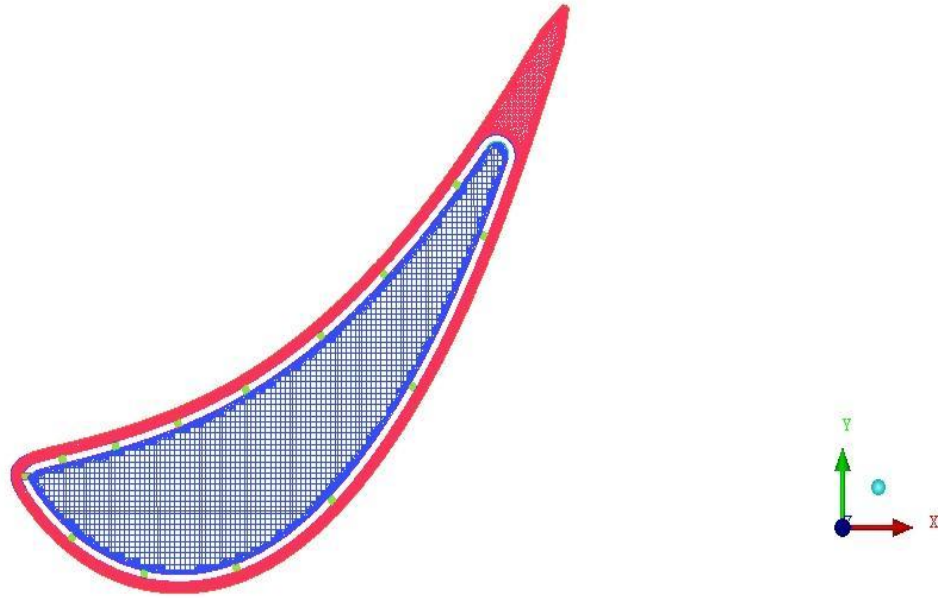
Figure 5-6: Hybrid mesh structure
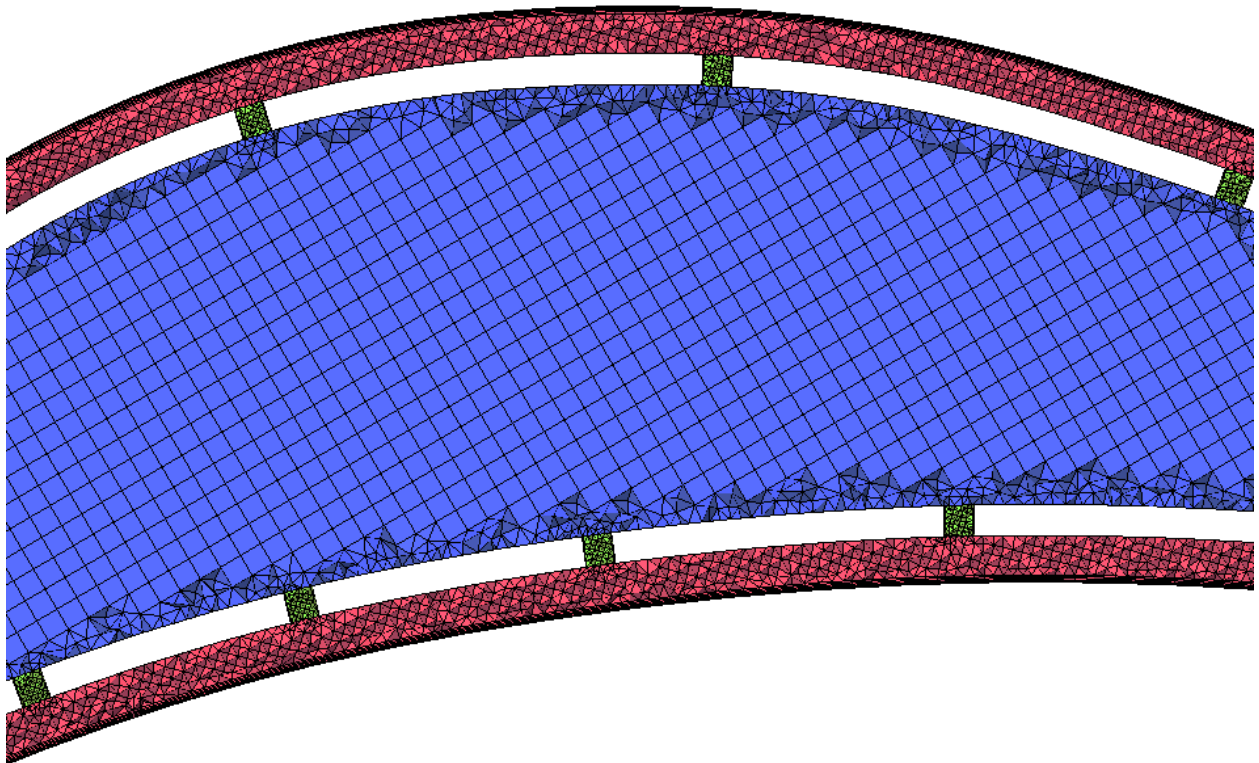
Figure 5-7: Section view of hybrid mesh structure. Grid size reduced for better visibility.

5.2.2   CFD Simulation Setup

CFD simulation was conducted in Fluent. The boundary conditions have been mentioned previously. Implicit, segregated based solver was used with pressure-velocity coupling set to SIMPLE algorithm. The relaxation parameters were tweaked accordingly for maintaining stability or achieving faster convergence. Spatial accuracy of the solution was improved by using second order upwind scheme. Convergence was defined when parameters such as velocity, pressure and temperature were non responsive to many iterations at surface monitors. The monitored surfaces included the inlet and outlet of jets, vane outlet and target airfoil surfaces. The minimum criterion for all cases was that the residuals obtained should be well below 10^{-5}.

The inlet boundary condition is provided as velocity inlet and is given an inlet velocity of 1.2266 m/s to achieve constant mass flow of 0.003269 kg/s. Since the Mach number remains less than 0.5, compressibility effects can be ignored [16]. The density is changed from a constant to incompressible ideal gas, where the density is calculated using ideal gas law without compressibility effects. The inlet boundary condition could be changed to a Pressure Inlet or mass flow inlet boundary template as this would not affect the solution under considerations. Fluid properties where changed too and are provided in the table below [42,26].

Table 5-5: Fluid properties at 500 K

Density, ρ $\left[\frac{kg}{m^3}\right]$	Incompressible ideal gas
Specific Heat, C_p $\left[\frac{J}{kg \cdot K}\right]$	1030.305
Thermal Conductivity, k $\left[\frac{W}{m \cdot K}\right]$	0.040284
Viscosity, μ $\left[\frac{kg}{m \cdot s}\right]$	2.6375×10^{-5}

5.2.3   Turbulence Modeling and Mesh Sensitivity

Various studies have been dedicated to modeling turbulence; and selecting a turbulence model greatly determines how accurate the solution to the problem can be predicted. A detailed review of the turbulence modeling w.r.t. single jet impingement is provided in section 5.1.3. For array of

jets it was found that due to cross-flow effect, the average Re in the boundary layer was higher than in single jet impingement case and hence low Re turbulence model was not an effective substitute for accurate solution [48]. Leon De Paz [26] presented an extensive evaluation of turbulence model selection for a similar case as herein; the results indicated that both the RNG and the SST turbulence models were quite capable of predicting heat transfer and hydrodynamics for impingement in turbine vane. In comparison, it was recommended to use the SST model for its relatively improved prediction. Hence, for the simulation considered, the k-ω SST turbulence model was chosen.

Mesh independence study was conducted by refining the mesh successively until the solution was insensitive. To estimate the discretization error, the absolute error is defined by the difference between the computed solution and exact solution. Since in this case the exact solution is not known, the independent solution is found using Richardson extrapolation theory or grid convergence index (GCI) and later validated [57]. All the refinement methods support mesh refinement procedure for structured hex meshes, where the number of nodes are increased using a refinement factor. This refinement is not supported for hybrid meshes. Hence, an effective refinement factor ($r_{effective}$) is defined as the ratio of elements in fine grid to coarse grid raised to a fraction of dimensionality of the problem [58], also shown below in equation (5.4). Refer to reference [58] for equations used to calculate the GCI.

$$r_{effective} = \left(\frac{N_1}{N_2}\right)^{1/D} \tag{5.4}$$

Where, N_1 and N_2 are the total number of elements for fine and coarser grid, respectively. D is the jet diameter. Table 5-6 illustrates the CGI values and confirms independence. The values shown are for the validation vane used; sensitivity was checked for all tested configurations. In addition, the local heat transfer coefficient values are also provided for last four grids used in Figure 5-8.

The relative difference in terms of the averaged heat transfer values between the fine and medium was 0.43% and 3.7%, 10.2% for the coarse and extreme coarse grids used, respectively.

50

Considering the computational requirements and time required to obtain a solution, the medium grid was used to validate the vane as it closely replicated true solution given the trifling difference in the averaged and local heat transfer values.

To decrease the long runtime for model creation, CFD setup, solving and post-processing results, macro scripts were written to support the iterative process and parallelization of processors was used to solve the N-S equation. Please refer to section 5.1.3 for more information.

Table 5-6: Mesh independence check - GCI calculation

$r_{effective}$	1.603
GCI Coarse	1.3 %
GCI Fine	0.6 %
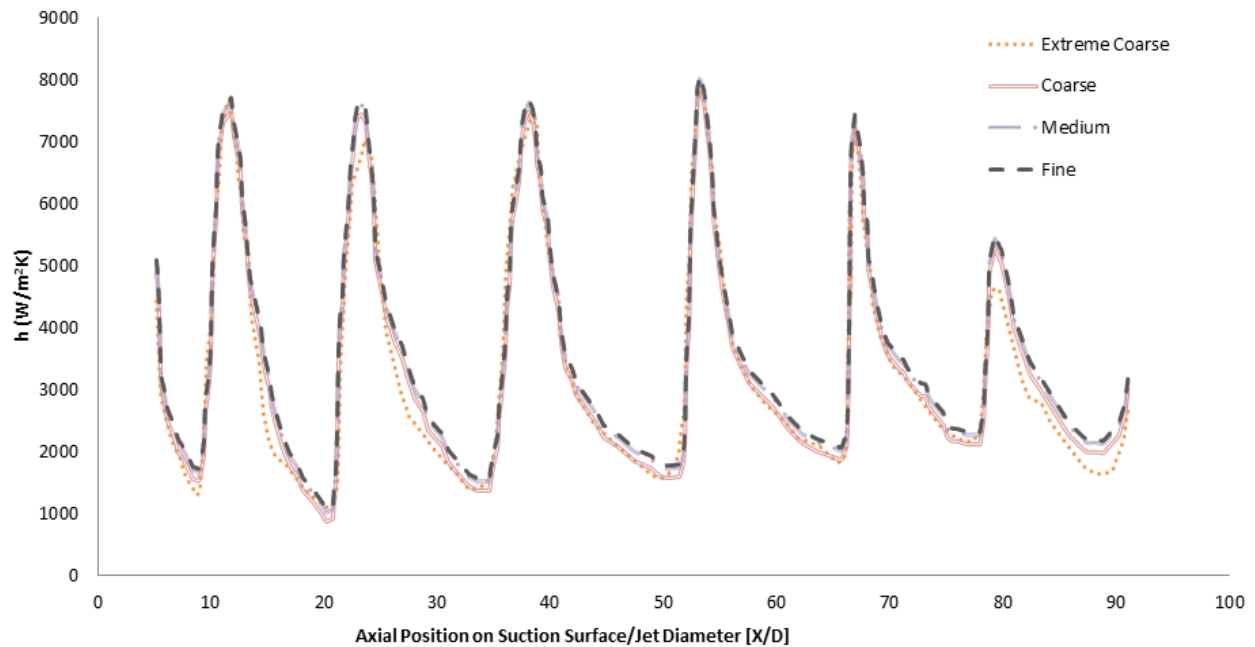
Figure 5-8: Sensitivity analysis based on local heat transfer distribution

CHAPTER SIX

RESULTS AND DISCUSSIONS

6.1   Single, Axisymmetric Micro-Jet Model

The effects of the change in the Reynolds number, the jet to target distance and geometrical parameters (size and shape of nozzle) on heat transfer enhancement from micro-jet impingement cooling are considered in the present study. Reynolds number of 6000, 4000 and 2000 were tested for H/D ratio of 6, 3 and 1. For the H/D test, the diameter of the nozzle was kept a constant. The results obtained were mainly compared to numerical work of Leon De Paz [13] and to corresponding experimental values.

6.1.1   The Effect of Reynolds Number

To compare the results and understand the effect of Re on the model, the Re was varied in the near transitional and turbulent region and other functional parameters in equation (3.9) and (3.10) are kept a constant. The results of the local Nusselt, Nu, and the average Nusselt number, $\overline{Nu}$, given by equation (6.1), is shown in Figure 6-1 for H/D = 6 and Pr = 0.72 at a constant diameter of 0.5 mm.

$$\overline{Nu} = \frac{1}{r} \int_0^R Nu_r \ \mathrm{d}r \tag{6.1}$$

It was observed in general that as the Re increases for a constant H/D, the heat transfer values throughout increases. At the stagnation region, the slope of the curve first increases and so do the heat transfer values; at close proximity, the slope attains a value of zero marking the region of maximum heat transfer. This does not occur at r/D of zero as the stagnation point is inherently unstable and moves around within a bound [1]. Also at stagnation point, convective effects are negligible (velocity is zero by definition). After attaining peak Nu, the heat transfer values then decrease monotonically. Similar results were also obtained numerically by Leon De Paz [13] and

Gardon and Akfirat [37]. In this case, however, the decrease from the maxima is initially steep, then a small transition region is seen where the Nu values almost even out. The curve then decays again with a steep slope. Experimental results by Lee and Lee [24] and Glynn and Murray [25] also showed a similar trend. This transition region is called the saturation zone and is the region between the stagnation region and the wall jet region; hence, a boundary layer transition occurs. This effect has also been attributed to the region with toroidal vortices being convected to the impingement plate [24], hence increasing heat transfer rates in this region. Moreover, an important observation to note is that as the Re increases, the maxima shifts off the stagnation point. This is due to the effects of the potential core. The potential core as described by Lee is nearly four times the diameter for fully developed flow and is directly dependent on the Re [24].
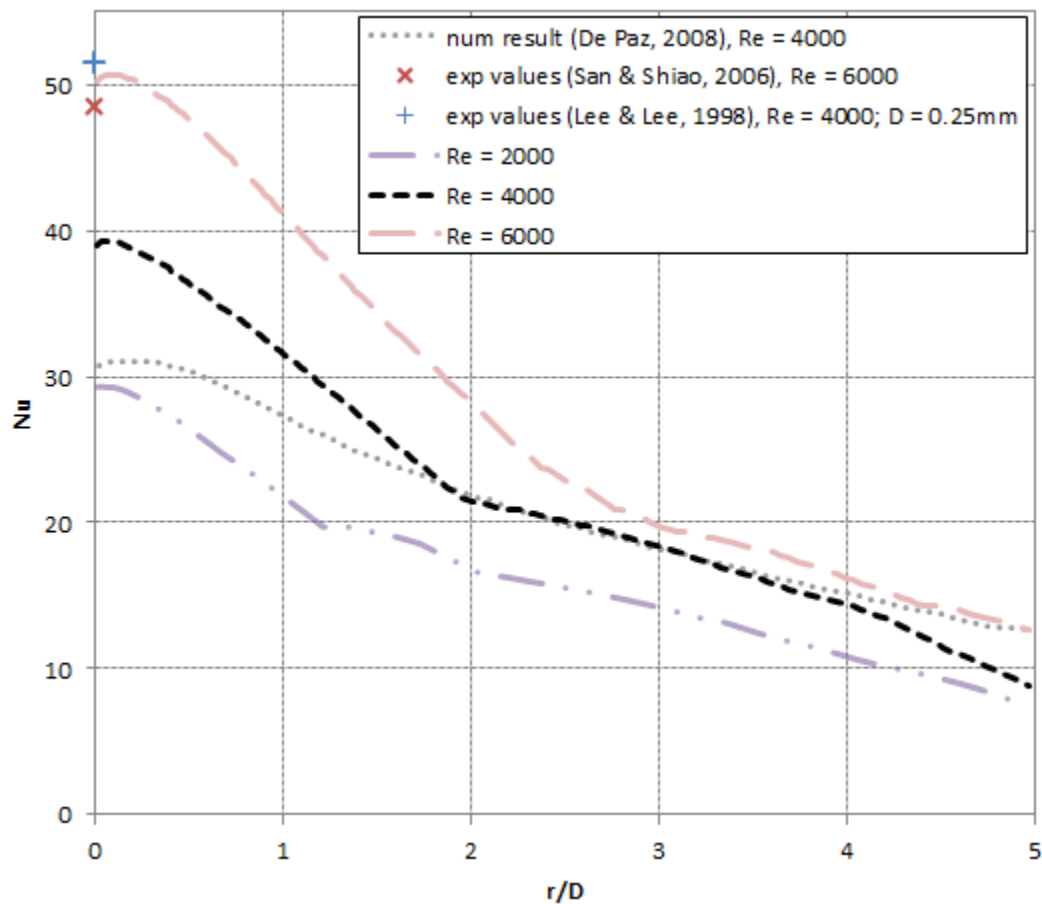
Figure 6-1: Reynolds number effect on local Nu at H/D=6 and D=0.5mm

From the plot in Figure 6-1, the calculated error at stagnation point obtained for Re = 6000 is 3.53% off from the experimental value obtained by San and Shiao as shown in reference [13]. Also in comparison to numerical results obtained, the wall jet region results closely agree to that obtained by De Paz [13]. The inaccuracy of stagnation values being differed from reference [13] could be directed towards the turbulence model selected by De Paz. To get an idea of the effect of diameter, the stagnation Nu value at Re of 4000 is plotted using equation (3.11), for diameter of 0.25 mm. The value obtained for micro diameter is about 31.97% greater than stagnation Nu value for macro case. The $\overline{Nu}$ values had deviation of about 6.48% and 1.75% (at Re = 6000) from that of the correlation in equation (3.12) and that of Huang and El-Genk [59], respectively; at Re = 4000 and 2000, the $\overline{Nu}$ values were within 6% and 10% difference, respectively. The variations obtained for different H/D ratios (H/D = 3 and 1) yields similar results and have not been shown for clarity. The global effect of Re can be easily judged by the $\overline{Nu}$ values obtained as mapped out in Figure 6-2 alongside average values obtained by Martin [22] for Re of 6000.
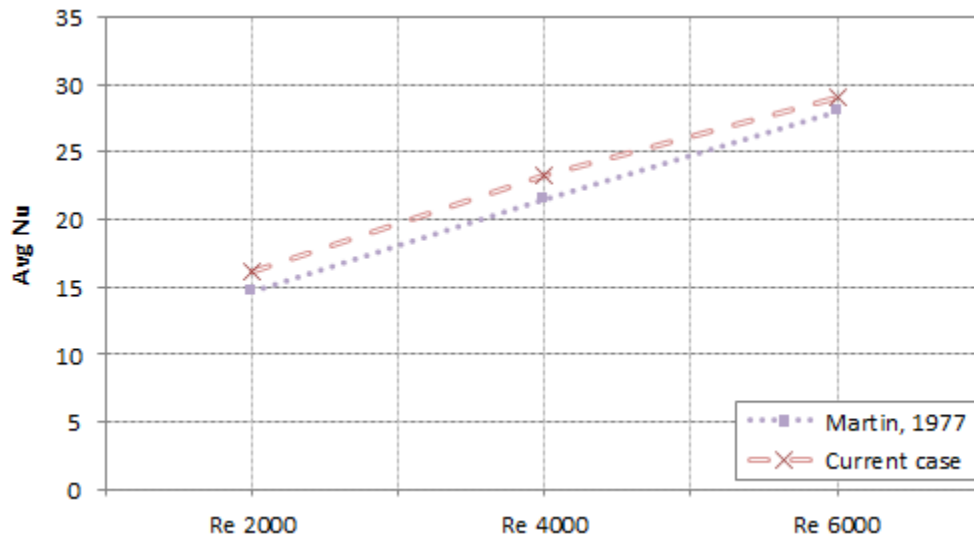
Figure 6-2: $\overline{Nu}$ with increasing Re at H/D=6

To understand the role of increasing Re and thus the heat transfer on the target plate, velocity contours were also plotted. Velocity contours help comprehend the relation of Re and Nu, as the flow is incompressible and the diameter is a constant. In a comparison from Figure 6-3 (a) and (b), it is seen that at higher Re, the jet is not influenced much by circulating air and penetrates through towards stagnation. The velocity magnitude at stagnation point by definition should be

zero; this is confirmed by the contours in the figure. This also causes the maximum heat transfer to be shifted away from the stagnation point itself, as convection effects are negligible. Additionally, due to entrainment to ambient and exchange of momentum the discharged jet widens from nozzle, degrading the potential core. This is clearly seen in the same figures.

The physics of cooling lies in the principle of forced convection around and further downstream of the impinged area, however not at the impinged surface. This can be observed in the radial velocity contours in Figure 6-5. It is seen that the velocity increases in radial direction parallel to the target plate and thus acts as forced convection on the wall. Maximum heat transfer is also accredited to these locations of maximum radial velocity. The convected heat, so called, is also shown in Figure 6-4. It is observed that the coolant warms up and absorbs the heat, thus producing a cooling effect due to forced convection with the driving force being temperature difference. The observations discussed above can all be seen in Figure 6-6 where the cooled temperatures are plotted.
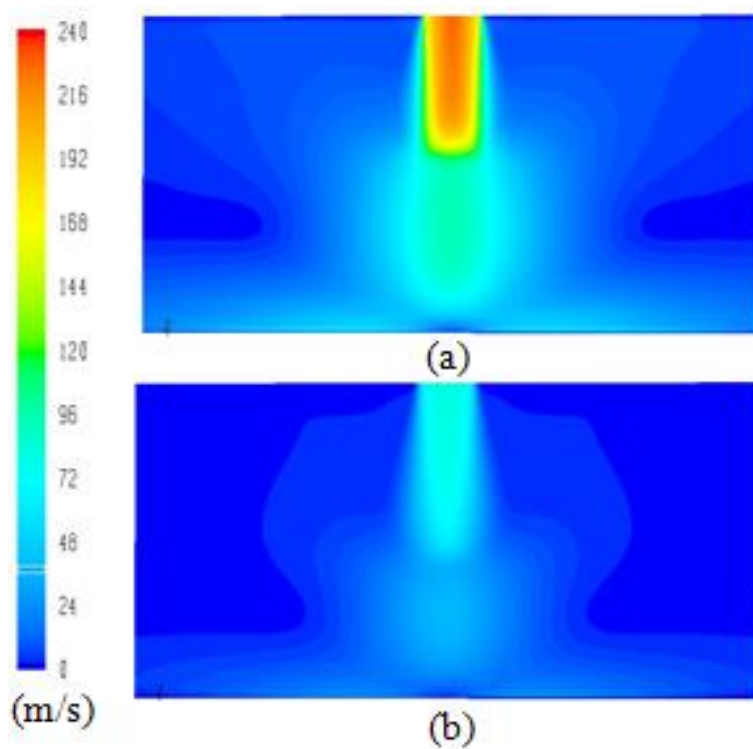
Figure 6-3: Contours of velocity at H/D=6 for (a) Re=6000 and (b) Re=2000
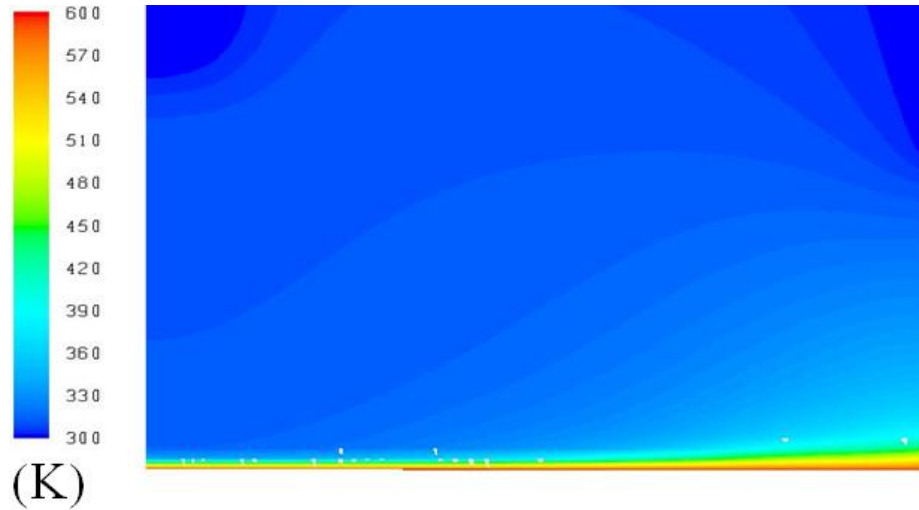
Figure 6-4: Contours of temperature perpendicular to target plate at H/D=6 and Re=6000

The role of boundary layer development plays an important role in the heat transfer region. To understand the effects of boundary layer, velocity vectors were plotted on the target surface[12] and compared to the Nu plot as shown in Figure 6-7. In Figure 6-7 (a), starting with the stagnation point (bottom left corner), the flow accelerates in the radial direction as shown by arrows in blue at the outer edge of the target plate[13]. It is interesting to note that accelerating flow does not maintain the Nu values and the heat transfer values continue to decrease steeply. This can be explained by the total pressure contours in Figure 6-10. At the stagnation point the velocity is zero and the dynamic head (impinging flow) completely transforms to a static pressure rise which equals the total pressure as also observed in Figure 6-8, Figure 6-9 and Figure 6-10. On the target surface, the highest recorded total pressure occurs at this point (in the stagnation zone) also marking the highest heat transfer values. The boundary layer in this region is thin and highly turbulent. Also, due to stagnation, convection effects are negligible; however, the stagnation point is inherently unstable and moves around within a bound. Thus, the high momentum coupled with velocity fluctuations is the cause of high heat transfer coefficient around the stagnation region [1].

---

[12] The velocity vectors lay on a plane slightly above the target surface as velocity at the boundary is zero. The plane is placed at the first set of nodes around y^+ of 2; hence, the plane lies inside the boundary layer.
[13] The Blue arrows are drawn to show the direction of the flow only and do not represent the magnitude of the velocity. The arrows were drawn as the vectors in the image were not scaled to screen resolution.
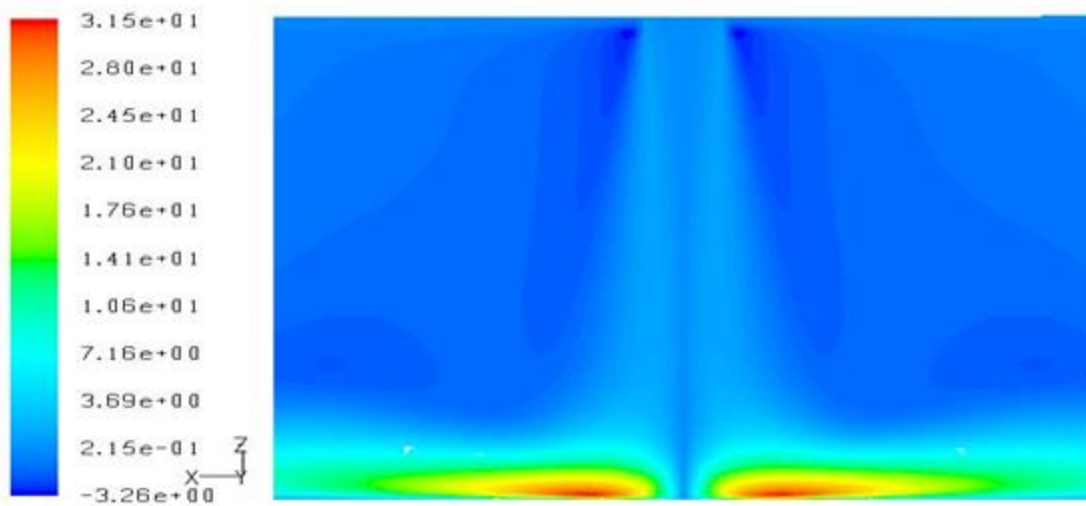
Figure 6-5: Contours of radial velocity [m/s] for H/D=6; Re=2000
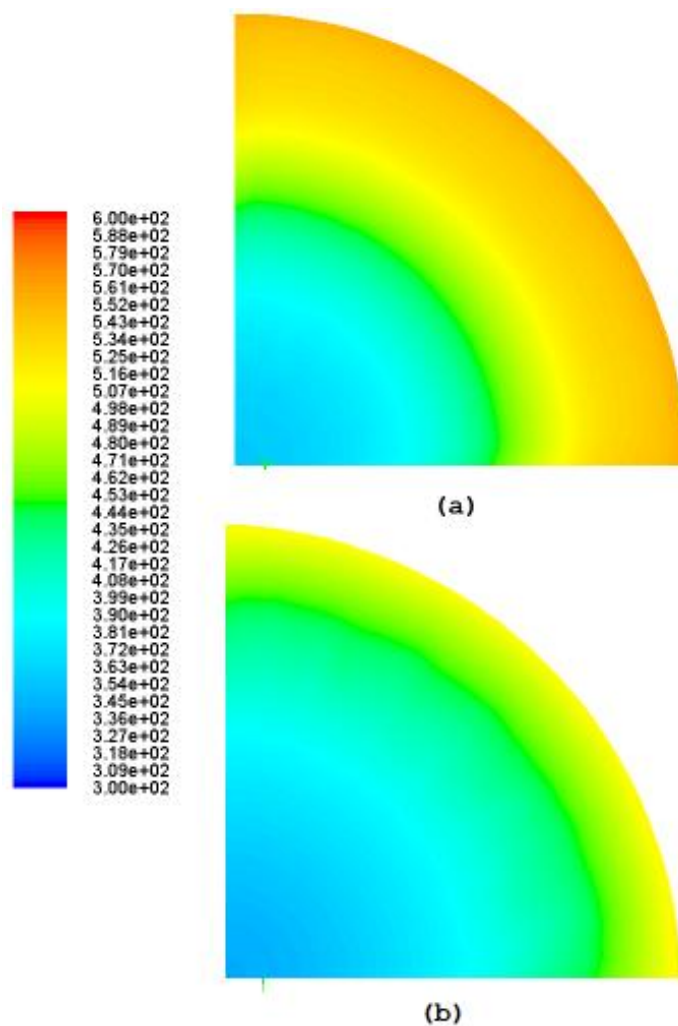
Figure 6-6: Total temperature [K] contours on target surface for (a) Re=2000 (b) Re=4000
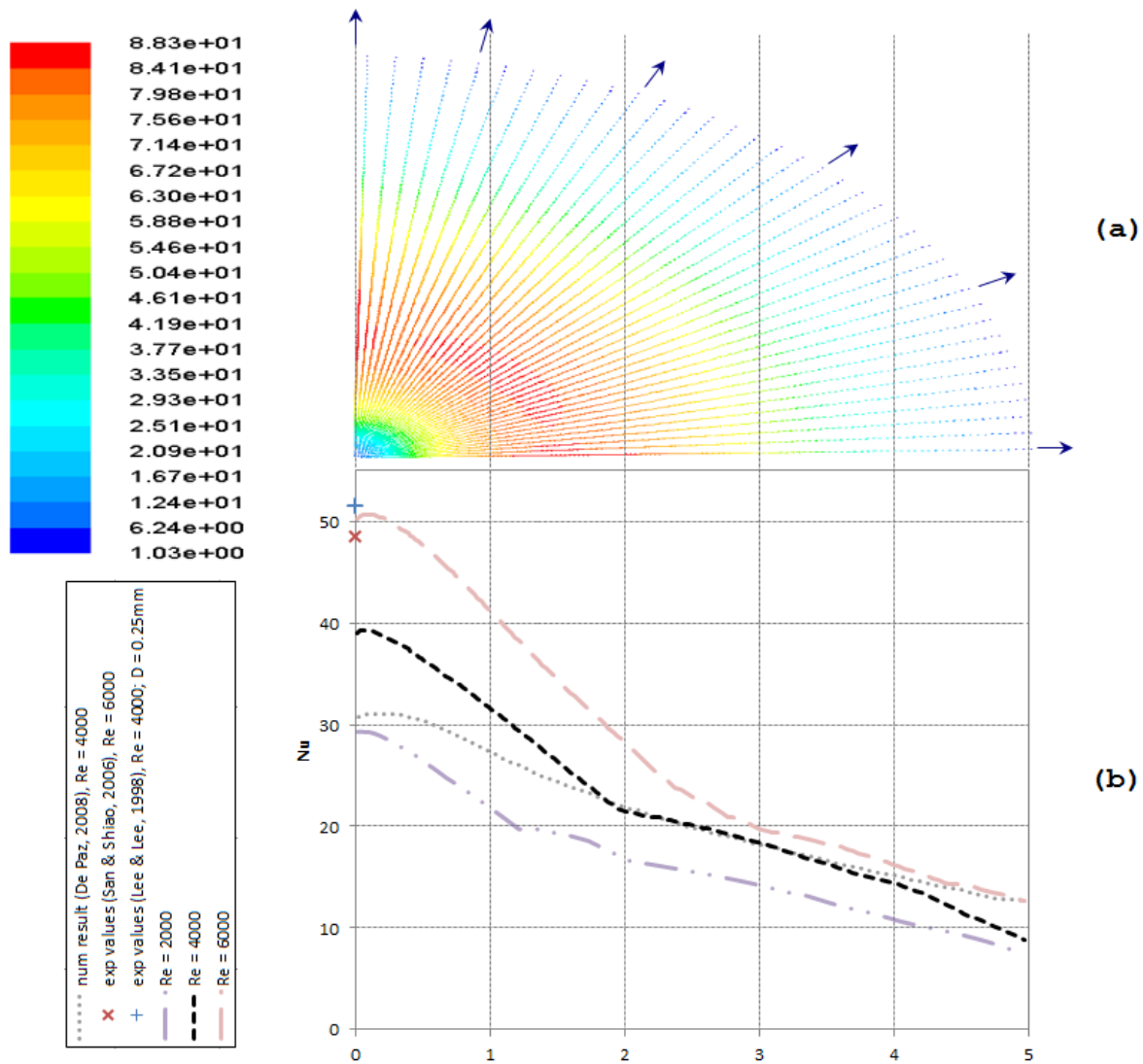
Figure 6-7: (a) Velocity vectors at target plate for Re=4000 (b) Local Nu values

At around r/D of 2 for Re = 4000, the so called saturation zone, is seen (refer to Figure 6-7). Considering the velocity vectors, flow is diffused in the radial direction. The gradient in terms of diffusion attains a lower value compared to the accelerating flow. This transition from a thin, unsteady and highly turbulent boundary occurs around this region to a stabilizing new boundary layer with a favourable pressure gradient. The acceleration and diffusion regions are clearly visible in Figure 6-9 where the dynamic pressure first increases and then decreases. This region with newly formed boundary layer experiences convective cooling effect. This saturation zone continues until r/D of 4 in Figure 6-7. The static pressure values soon decrease and attain gauge

value of zero implying atmospheric pressure is reached as confirmed in Figure 6-11 where the absolute pressure contours are plotted.

The reasoning for the extended total pressure contour and stabilizing Nu values is the recirculation of air making the flow healthier or energised (in terms of momentum). The build-up of skin friction from where the wall jet boundary layer is created (after transition) finally reduces the velocity value to zero and thus the heat transfer values decrease rapidly. Hence, high friction losses due to favourable pressure gradient are the cause of the diminished Nu values.

Considering the contours of total pressure on the plane between the nozzle and target plate, the pressure values are seen to depreciate below atmospheric value (Figure 6-10). This depreciated pressure is the cause for the impinging flow (that is, lower pressure demands for higher velocity). The total pressure soon increases as the static pressure increases just above the stagnation point.
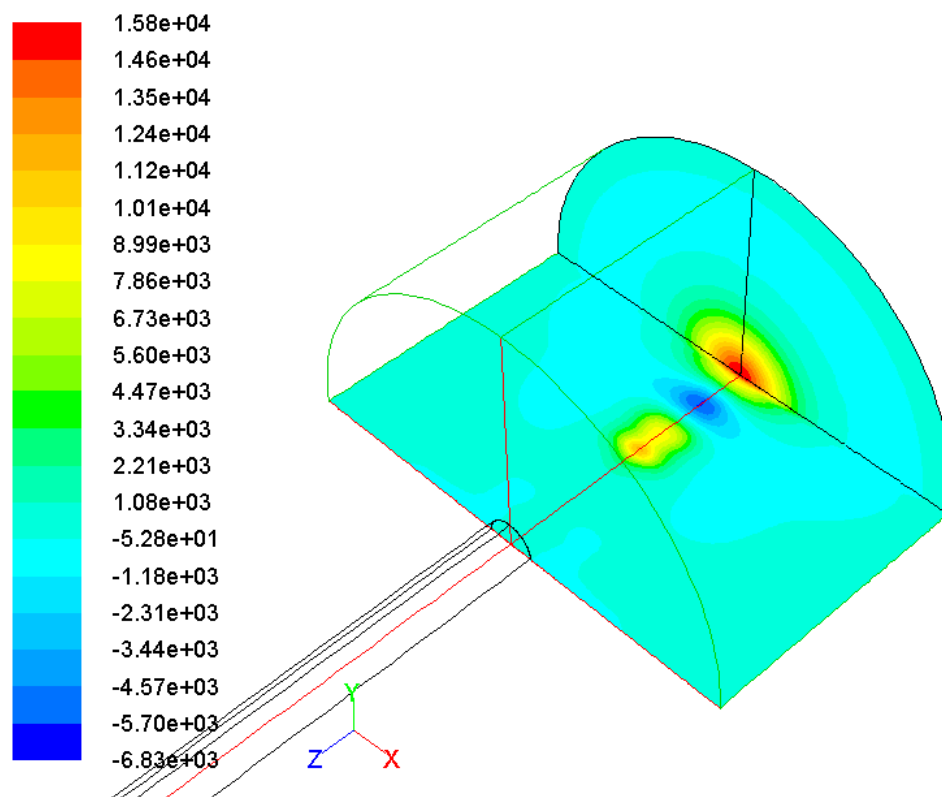
Figure 6-8: Static pressure (gauge) [Pa] values at Re=6000

59
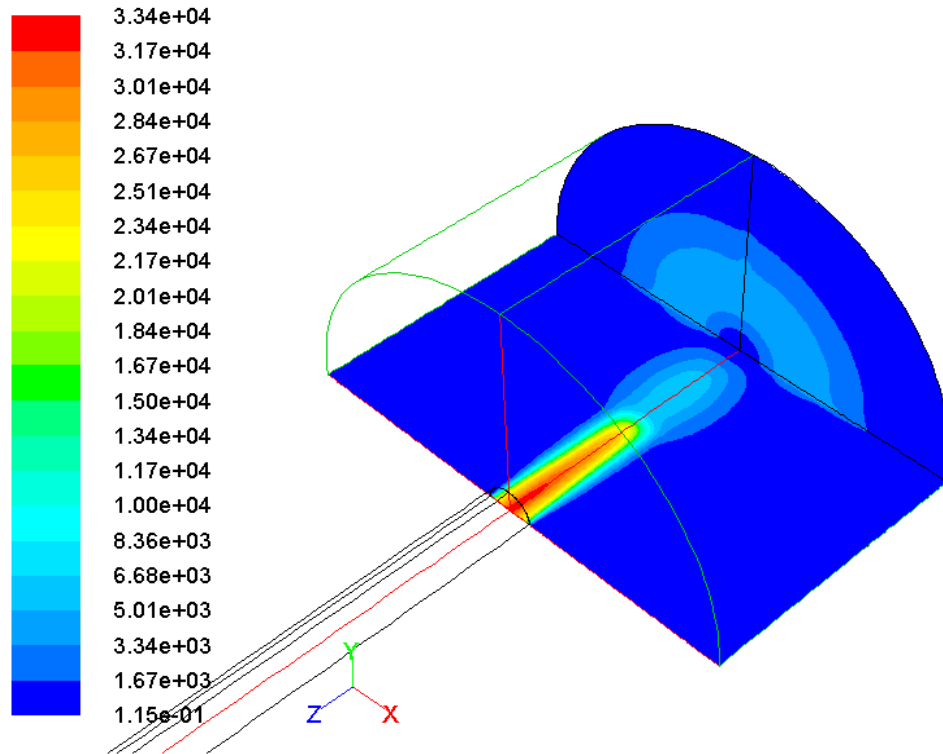
Figure 6-9: Dynamic pressure (gauge) [Pa] values at Re=6000
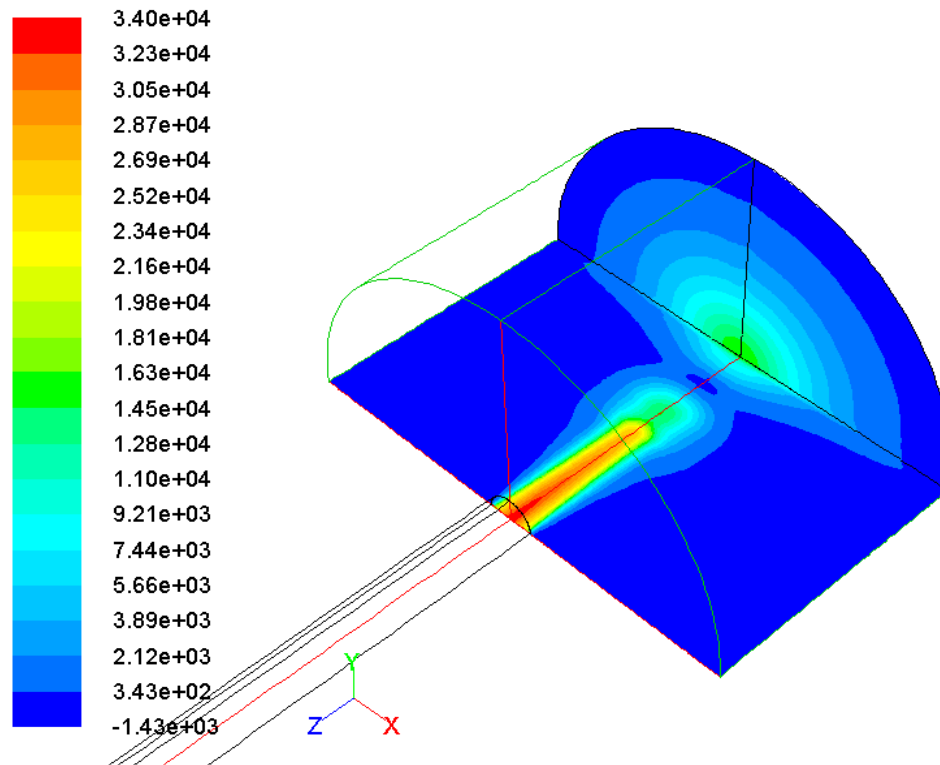
Figure 6-10: Total pressure (gauge) [Pa] values at Re=6000

60
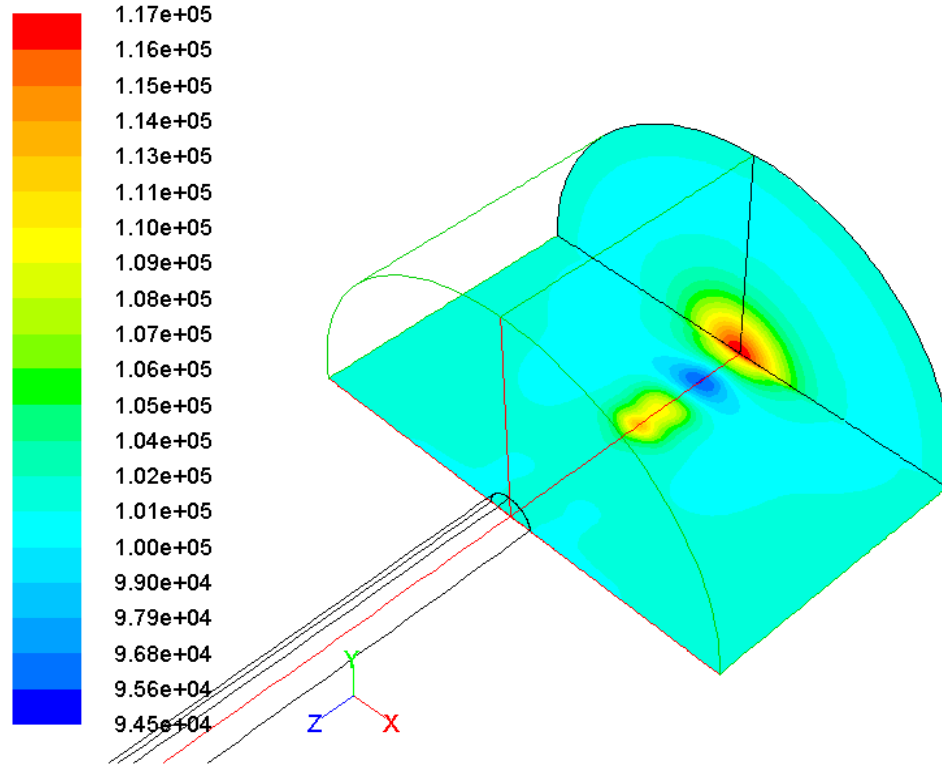
Figure 6-11: Absolute pressure [Pa] at Re=6000

6.1.2   *The Effect of Jet to Target Distance*

To understand the effects of changing the H/D ratio, the jet diameter was kept a constant at 0.5 mm with Pr = 0.72 and Re = 6000. H/D ratio was then changed and Nu variation was seen with respect to r/D for different H/D ratios. The jet to target distance was changed in this case as changing the height kept the jet exit velocity constant for all cases; also, it was done for ease of setup and coding purposes. Figure 6-12 shows a plot for the effect of H/D ratio at H/D=1, 3 and 6. Analogous to the previous case, the variation obtained for different Re (tested for Re = 4000 and 2000) yields similar results. For comparison, however, results obtained by De Paz have been included [13].

It is noticed from Figure 6-12 that changing the H/D ratio has negligible effect on the local heat transfer and thus cooling especially after r/D = 0.5. This phenomenon is confirmed by various such studies for the given Re [13,24,40,43,44]. A typical shift of stagnation value and maximum Nu value is observed as H/D changes. The stagnation point is followed by a steep slope where

61

the value of the slope decreases as H/D decreases. Similar observation was made by Lee and Lee [24]. However, in the experimental results for Lee and Lee, there is a visible secondary peak especially at lower H/D ratios. This is not prominent due to the effects of confinement. The effect of toroidal vortices enhancing the heat transfer also diminishes as H/D increases as grasped in Figure 6-12. This may be attributed to the high momentum flow in the radial direction and hence a reduced flow reversal. This is also confirmed from Figure 6-13 where an increase in jet to target spacing moves the center of the toroid radially outward. For the two streamlines shown at H/D = 1 and 3 for Re = 6000, the toroid moved from about r/D = 2.5 to about r/D = 4.75. That is, a change of H by 2D, displaced the center of toroid by about 2.25D towards the outlet. This effect is confirmed in an article by Fitzgerald and Garimella [60]. The figure also illustrates the entrainment due to recirculating air into the potential core. The effect of potential core length of the free jet on the impingement plate is also seen at the stagnation point. The Nu values are almost a constant and prominent for H/D = 1. As the potential core length is about 4D for fully developed flow [24], the heat transfer characteristics for low H/D ratio become complicated due to complex interactions in the stagnation region.

Due to the presence of confinement although the secondary peak is not formed, the confinement helps lengthen the saturation zone. For H/D = 1, the saturation zone experiences higher heat transfer rates compared to H/D of 3 or 6. For instance, at r/D of 2.5 the variation in heat transfer between H/D = 1 and H/D = 3 was about 5%. Similarly, the variation in heat transfer at the same radial distance for H/D = 1 compared to H/D = 6 was about 15%. The effect of confinement is dominant for H/D ratio of 1 and weakens as the ratio increases. The length of the saturation zone is dependent on the intensity of the toroid and the position of its eye.

For all the cases, however, the maximum Nu values are greater than the stagnation values. The location of maxima is around r/D = 0.5 for low H/D ratios. According to Gardon and Akfirat [37] and Lee and Lee [24], this maxima always occurs at r/D = 0.5, which may be due to the accelerating flow at lower nozzle to target plate spacing and due to the local thinning of the boundary layer. Conversely, this peak could also be credited to non-uniform, mixing induced turbulence in the developing jet that penetrates the boundary layer, increasing the heat transfer as noted by Pamadi and Belov in reference [24]. The average heat transfer values show marginal

difference when H/D ratio is changed from 1 to 6 as marked in Figure 6-14. This trend is not the same as predicted by Martin [22], but the effect could probably be a cause of confinement, where warm air recirculates and reduces the overall or $\overline{Nu}$ values especially at lower H/D ratios as also revealed in Figure 6-13.
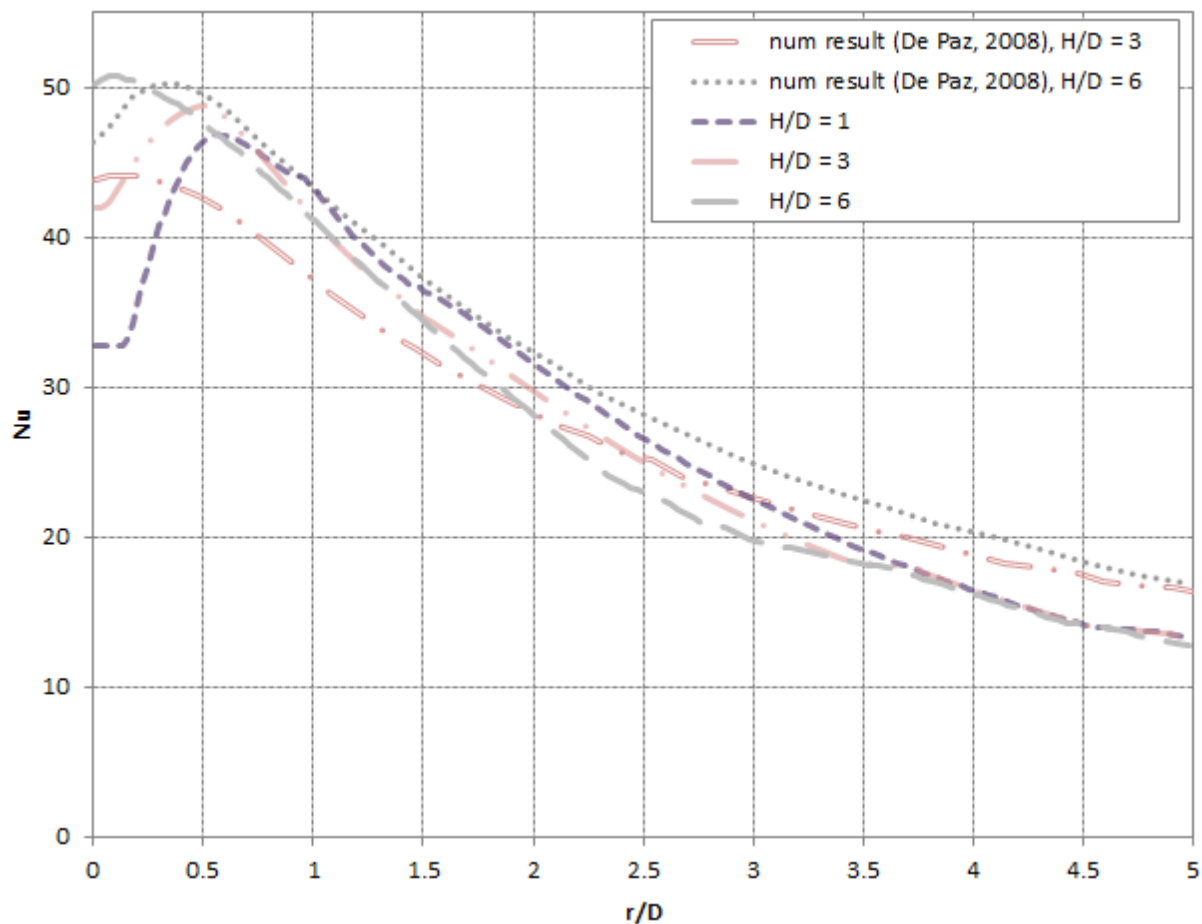
Figure 6-12: H/D effect on local Nu at Re=6000

Overall, it is seen that the Nu does not vary much with changing H/D ratios. That is, increasing H or decreasing D does not have much effect on the heat transfer values. This is however true for macro jet diameters. The effect of nozzle geometry including the diameter has been argued. Jambunathan et al. [36] argue that the Nu is not only a strong function of the Reynolds number but empirical values obtained show that the jet to target spacing (H) and the radial distance (r) are also important contributors to the heat transfer involved. Nevertheless, the contributions adhered to the condition that Nu is independent of H up to 12D at r > 6D. It has also been

suggested that the effect of nozzle geometry and diameter is more visible at lower H values. The total temperatures obtained for two H/D ratios at Re of 6000 is shown in Figure 6-15 confirming the observation of similar heat transfer results.
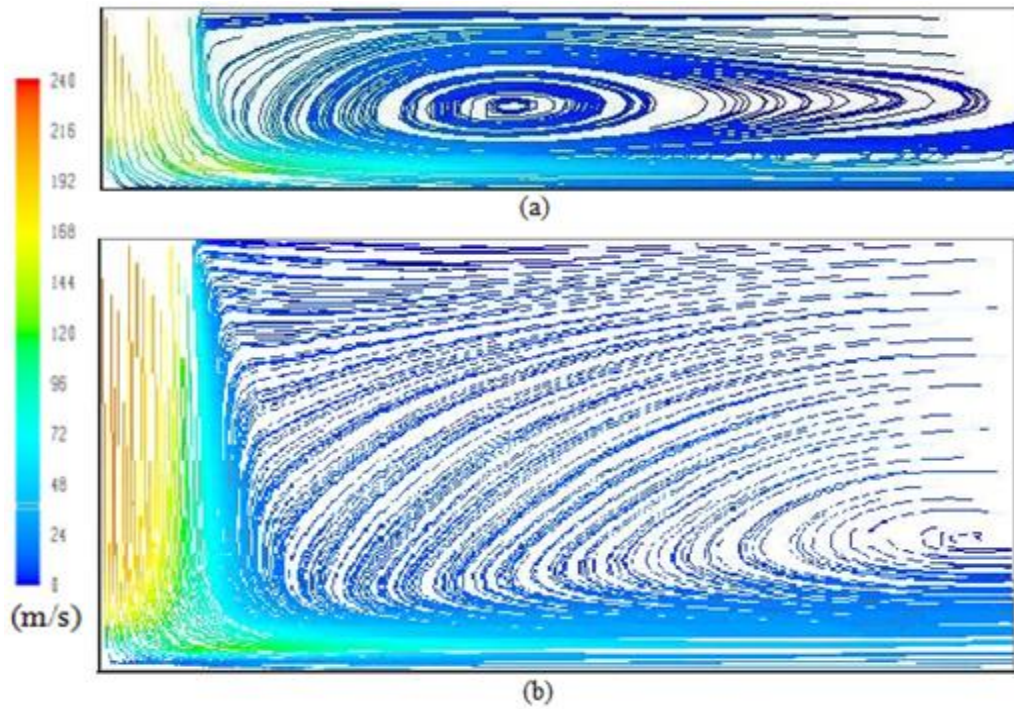
Figure 6-13: Path lines given by absolute velocity magnitude for (a) H/D=1 and (b) H/D=3
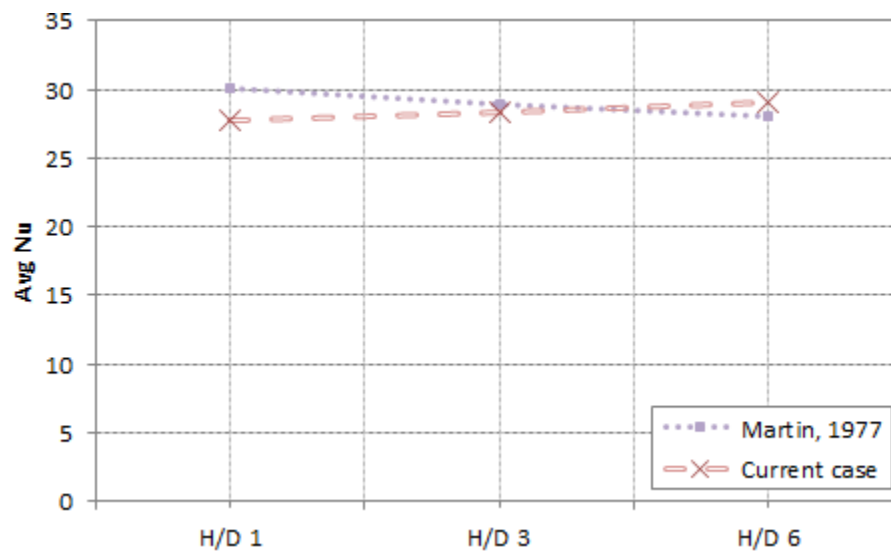
Figure 6-14: $\overline{Nu}$ with increasing H/D ratio at Re=6000

Considering the total pressure contours (Figure 6-17) for the different H/D cases, it was seen that the high pressure areas are created due to the high dynamic head impinging on the target surface. Since for H/D = 1 the stagnation area is larger as seen clearly in the absolute pressure diagram in Figure 6-16 (a) when compared to Figure 6-16 (b) and (c). Also, at the stagnation area, velocity is minimal and hence, the heat transfer values diminish. Moreover, the slope of the Nu values in the stagnation zone is zero. The radial distance of this zero slope is captured in Figure 6-12 where for H/D = 1 the stagnation dimension increases to 0.4 diametrically when compared to H/D = 3 or 6.
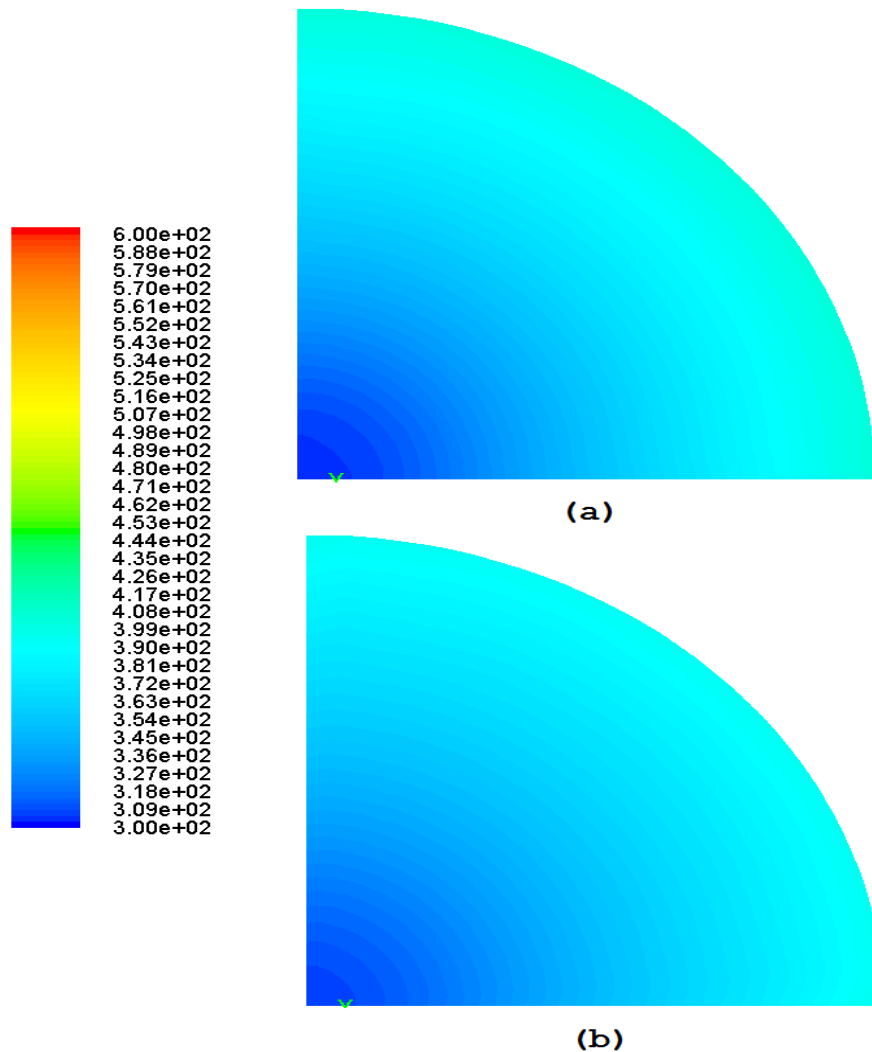
Figure 6-15: Total temperature [K] contours on target quarter model for (a) H/D=1 (b) H/D=3
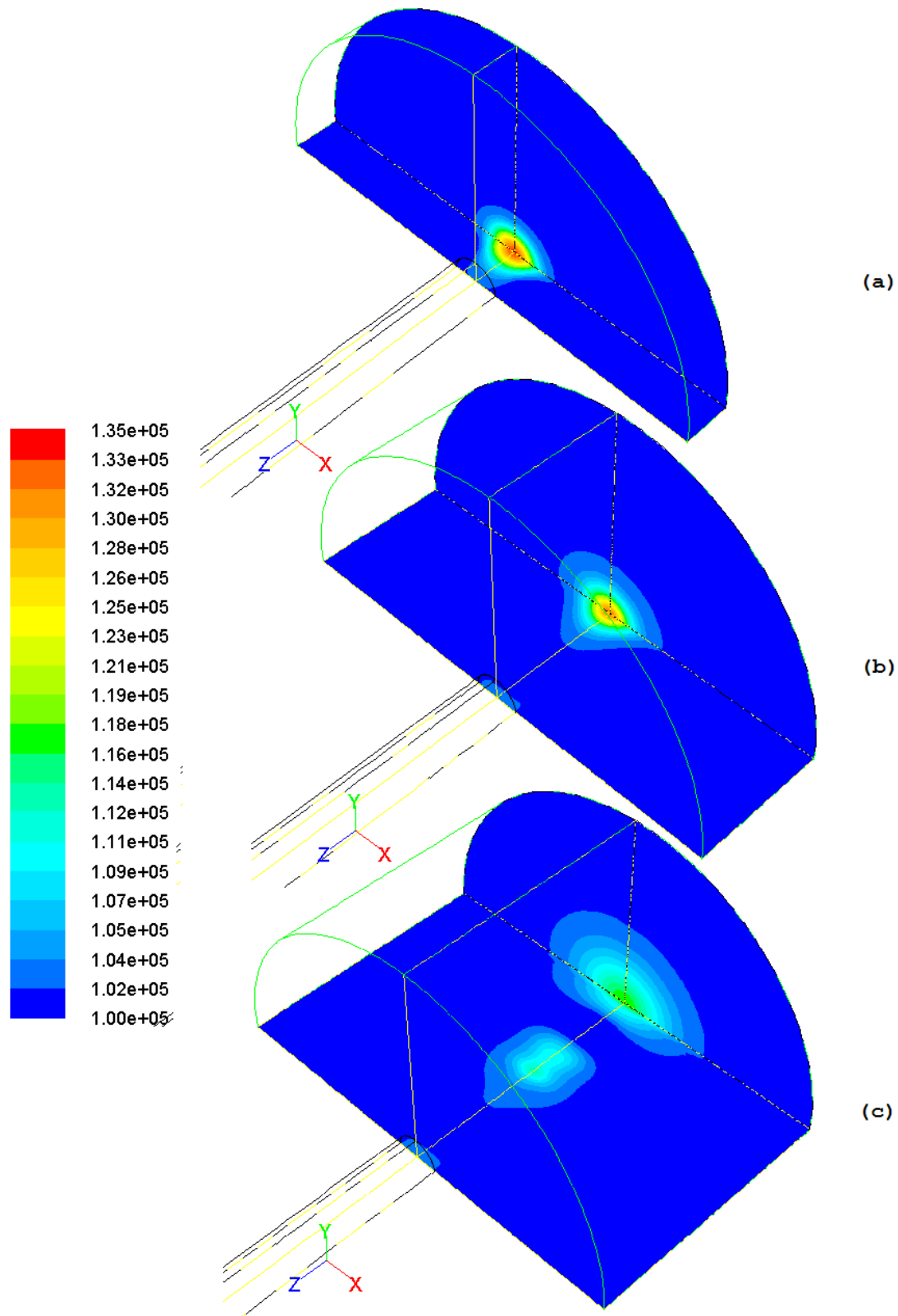
Figure 6-16: Contours of absolute pressure [Pa] (a) H/D=1 (b) H/D=3 (c) H/D=6
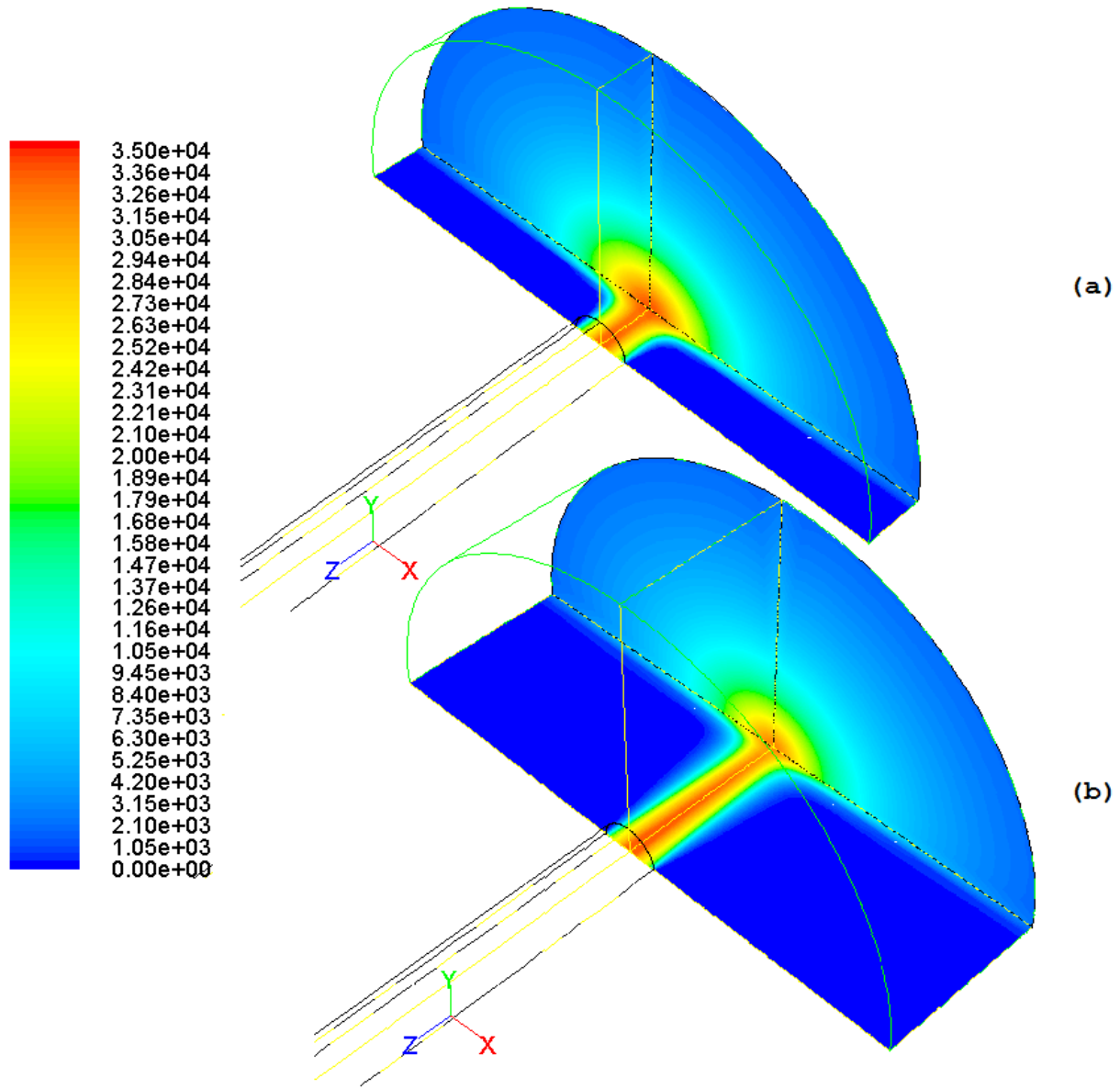
Figure 6-17: Contours of total pressure (gauge) [Pa] (a) H/D=1 (b) H/D=3

6.1.3   The Effect of Change in Nozzle Diameter

Since the micro-jet flows satisfy the continuum hypothesis, it is expected that the effect of nozzle diameter on local heat transfer shall maintain similar effects as that of the nozzle diameter on local heat transfer for the macro case. The comparison of nozzle diameter (macro scale) was shown by Lee and Lee [24] for H/D = 6 and Re = 23,000; the effect of diameter on the local Nu

was negligibly small for wall jet region due to impinging flow effects being diminished for r/D > 0.5. However, the stagnation Nu values were seen to increase by about 20%.

The effect of change in nozzle diameter can also be thought as the change in H/D ratio, where the H is kept a constant and the diameter is varied. Considering the above effects of H/D, it was seen that the heat transfer values did not have a significant effect in terms of cooling. However, by changing the diameter and maintaining the same mass flow rate, the average Re number is seen to increase. The effect of nozzle geometry including the diameter has been argued as presented previously in section 6.1.2. Hence the effect of change in nozzle geometry is studied.

The current study pertains to the application of micro jet impingement cooling for gas turbine blade. Hence, to understand the effect of reducing the nozzle diameter to a micro scale of 0.25 mm, the following assumptions are made. Firstly, the driving force for the coolant fluid is the pressure difference between the inflow and outflow boundary conditions. Secondly, this model is a simple reduction in jet diameter from the default values. To wit, it is the resultant model where the turbine vane's plenum is assumed to be drilled with an aperture of 0.25 mm in lieu of 0.5 mm. The first assumption, allows the use of mass flow rate specifications at inlet. If G is the mass flow per unit heated area, and since the flow is incompressible, a constant velocity inlet can be specified for the model. No other difference is made to the model; this allows for direct comparison between the micro and macro jets for the turbine vane. The results obtained for G = 0.5 and 0.6 kg/m^{2}s (mass flow of 0.00982 g/s and 0.0118 g/s, respectively) with H/D = 6, are displayed in Figure 6-18 for both, micro and macro case.

It is apparent that when the diameter of the nozzle is reduced to micro scale, significant improvement in heat transfer coefficient is obtained. The $\overline{Nu}$ for macro diameter at G = 0.5 kg/m^{2}s is 13.76 whereas for the micro diameter the value is 20.95 with 37.3% increase in stagnation value. Similarly, for G = 0.6 kg/m^{2}s, the stagnation value rose by 26.68% with 31.88% difference in the average values. About 20% to 70% increase was seen in stagnation values when the jet diameter was reduced from 1.5 mm to 1 mm in an experimental setup by Glynn and Murray [25] which confirms similar findings. Their paper suggested that, even with low Re values, large heat transfer coefficient could be achieved by using small jet diameters, not

only for enhancing stagnation heat transfer but to also maintain relatively good heat transfer rates in the near wall jet region.

The enhancement of heat transfer was expected due to the higher velocity achieved at nozzle exit, however the proportion of enhancement was greater than expected for micro diameters when compared to decreasing diameters at macro level. That is about 40% increase in stagnation value by change in diameter of 0.25 mm. This phenomenon of changing nozzle geometry being an important parameter has also been discussed previously. The increase in velocity is apparent as provided in Figure 6-19 below when compared to Figure 6-3. The effect however rapidly decreases in the direction of r/D (moving radially outwards from the stagnation point). The steep drop in Nu is obtained in Figure 6-18 for r/D < ~1.3 can also be perceived in Figure 6-20. The Nu contours have been added for reference (Figure 6-20) to show the fading effect at downstream region on the target plate. The true nature of heat transfer however is not only determined by the velocity but also the turbulent kinetic energy and turbulent fluctuations as explained in section 2.2. The contours of turbulent kinetic energy are provided in Figure 6-21.

The argument as proposed by Jambunathan et al. [36] that the Nu is not only a strong function of the Reynolds number but also the jet to target spacing (H/D) and the radial distance (r) is quite apparent from Figure 6-19, Figure 6-20 and Figure 6-21. Using Figure 6-21 as a refernce, it can be assumed that if the distance between the target plate and the jet exit was reduced to where the turbulent energy was a maximum (near the end of the potential core), the heat tranfer values would have been higher than seen in the case considered in the present study. The effect of radial distance on Nu is evident from the Nu contours in Figure 6-20.

Thus, the results obtained for effect of nozzle diameter for H/D of 6 varied greatly for wall jet region than what was expected and obtained for macro jets as shown above. Hence it is clear that the dependence on nozzle diameter does not fit with established trends of macro diameter effects and the variation is not continuous in results obtained from different diameters. The next section provides further insight to the results obtained due to changes in nozzle geometry.
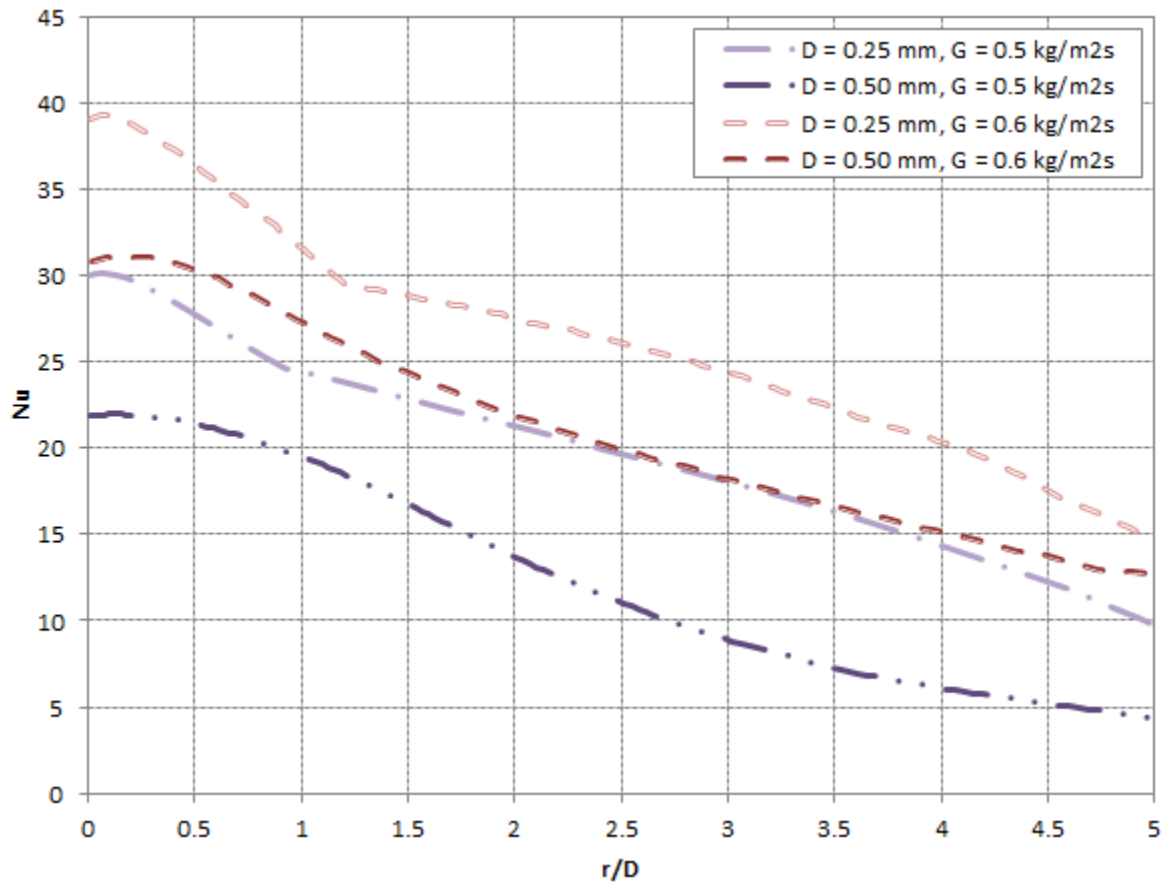
Figure 6-18: Effect of nozzle diameter at H/D=6
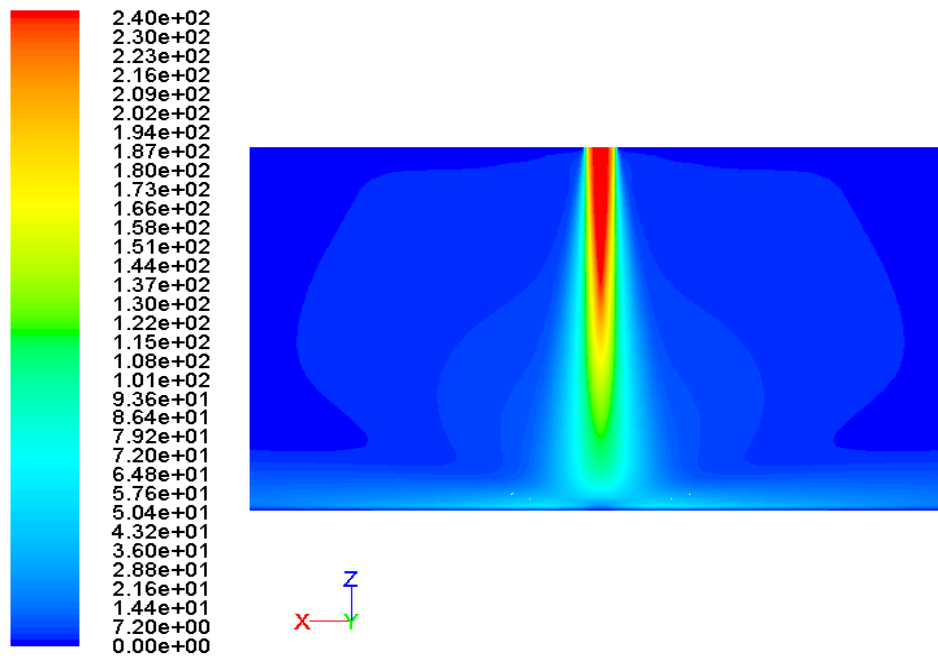
Figure 6-19: Velocity contours [m/s] for micro jet case

70
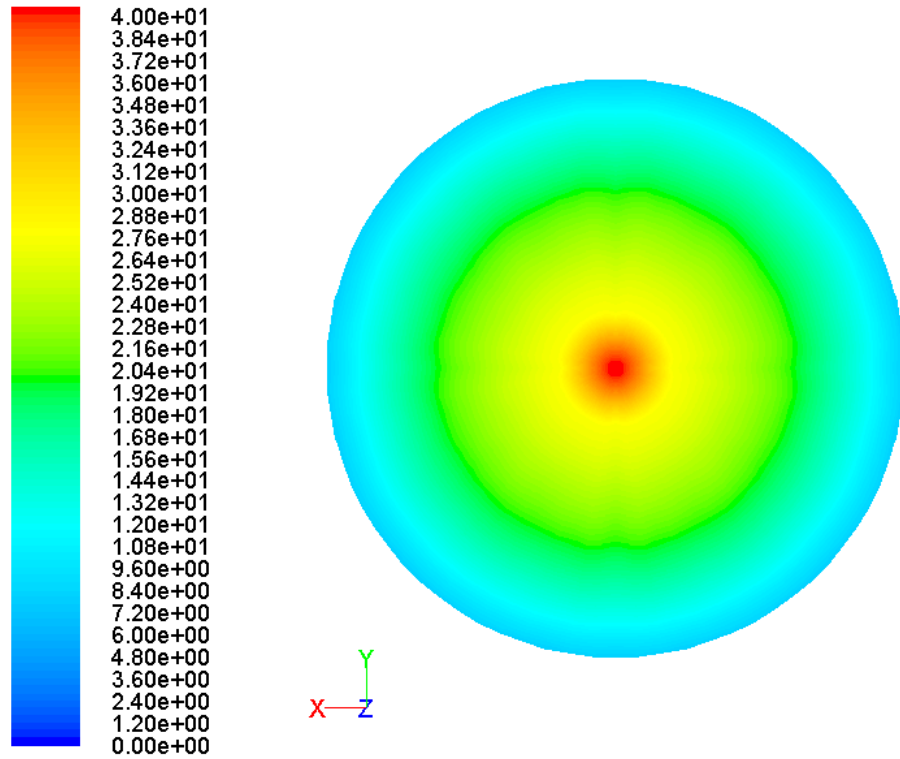
Figure 6-20: Contour of Nu for micro jet case
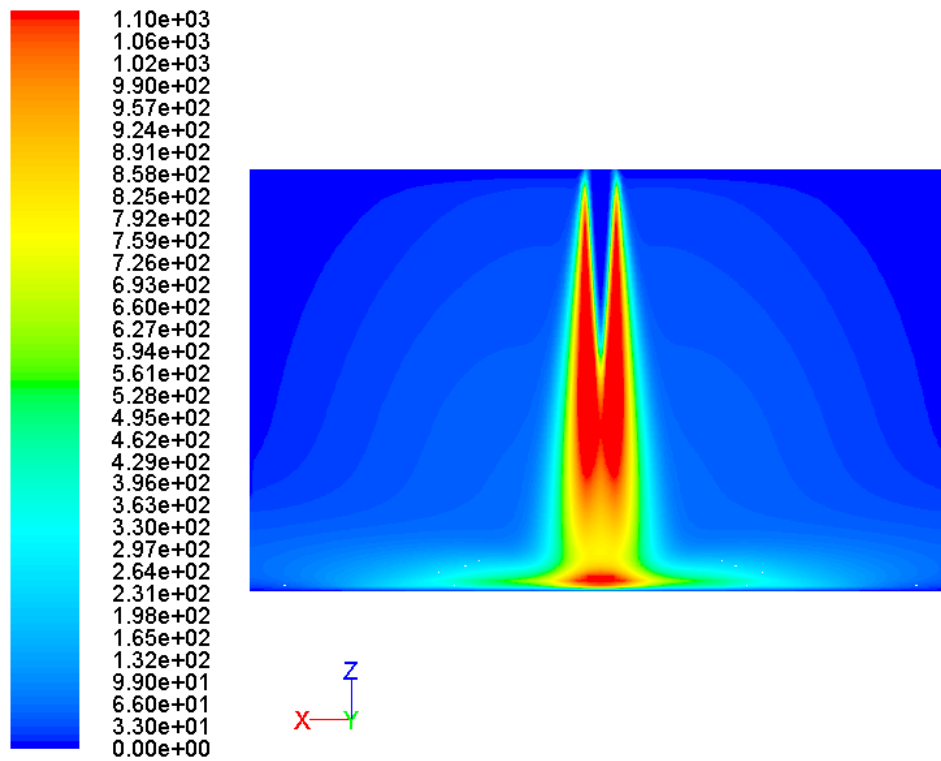
Figure 6-21: Contours of turbulent kinetic energy for micro jet case

71

6.1.4   The Effect of Change in Nozzle Shape

The nozzle shape was changed to an ellipse with the same hydraulic diameter of 0.5 mm as previously mentioned. Results were obtained for three regions on the target surface. Heat transfer results were extracted on a 2D line lying on the target surface as shown in Figure 6-22. The values were extracted such that the lines were parallel to the major axis, minor axis and a bisecting line between the major and minor axis of the ellipse termed as 45 degree axis or the bisecting axis[14]. The values reported were for r/D = 0 (at the stagnation point) and moving radially outwards in a similar fashion as for circular jets. The area within the circle in red is the target surface in Figure 6-22 and the image is taken in perspective view. The flow direction is outside the page from the elliptical nozzle.
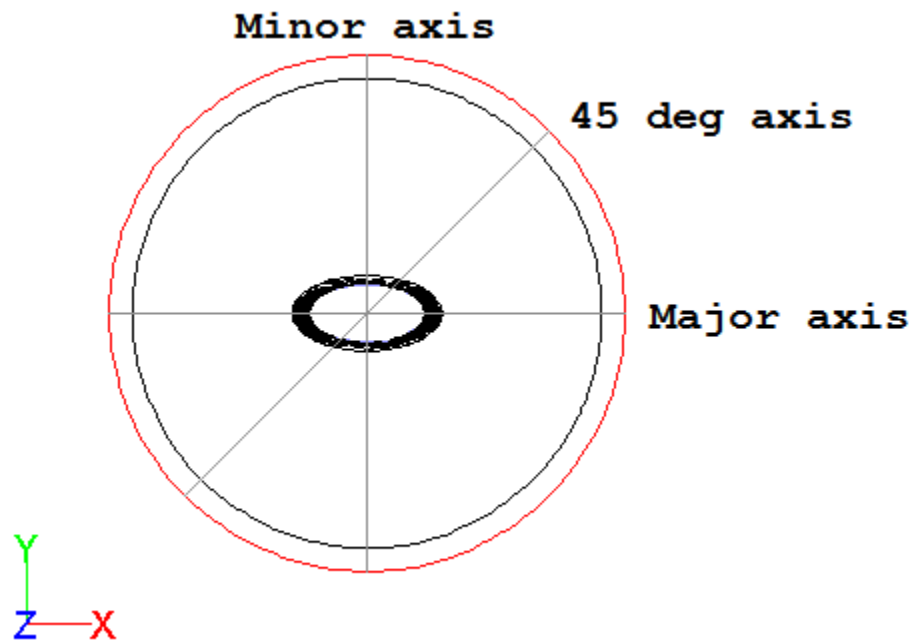
Figure 6-22: Extraction of heat transfer results on 2D lines shown in grey

Heat transfer results indicate that for the same hydraulic diameter as that of the circular jet, the Nu values obtained for elliptical jets are higher than those for circular cross-sectional nozzle as viewed in Figure 6-23. Clearly seen is the elongated stagnation zone for elliptical nozzles

---

[14] The dimensions of the major axis and minor axis for the ellipse as given in Chapter 4.1 correspond to the true major and minor axis of the ellipse and should not be confused with the heat transfer results extraction line as in Figure 6-22

starting at r/D_H of 0 to around 0.7 where the Nu values varied within 2% margin. The diameter used is the hydraulic diameter.

At $r/D_H = 0$, the Nu value marked 50 for circular and elliptical case with around 0% difference. The major axis saw the highest heat transfer values while the minor axis was comparatively lower at $0.7 < r/D_H < 3.5$. As expected, the bisecting line heat transfer values were in between the two lines compared previously. The trends in Nu values remained similar to that of the circular jet. That is, initially the slope remained around zero marking the stagnation area. The slope then increased until the Nu values reached its maximum and hence the slope gained a value of zero again. The difference between the maximum heat transfer values from minor and major axis is about 8%. The relative positions of the maximum values also varied where the former axis obtained maximum Nu value at $r/D_H = 0.6$ while the latter case obtained maximum Nu value at $r/D_H = 1.25$. In all cases for an elliptical jet, the decay in the Nu values was higher (steeper slope) until the saturation zone. Also, according to the results obtained the saturation zone heat transfer values were the same for the minor, major and 45 degree axis as seen at r/D_H of 3.5. The slope at the saturation zone was the same for the elliptical case and the circular cross-section; however, the heat transfer values were higher by about 44%.

The average Nu values in Figure 6-24 provided some information on the variation in heat transfer results across the target plate. It was clearly seen that the circular cross-sectional jet at Re of 6000 and H/D ratio of 6 under performed compared to the elliptical jets. The average Nu value for the elliptical jet was 36.82 which was 20.8% higher compared to the circular jet. The breakdown of the average values in terms of the region of target surface (that is, major axis, minor axis and bisecting axis) is provided in Figure 6-24. The trend was obvious considering Figure 6-23 that the major axis performed better. The deviation in averaged heat transfer values from minor axis to bisector axis was 4.8% while the deviation from bisector axis to the major axis was around 6.2%. The variation from minor axis to the major axis was computed to be 11.7%. The difference in the average heat transfer values comes from the region between the stagnation zone and the saturation zone as seen in Figure 6-23.
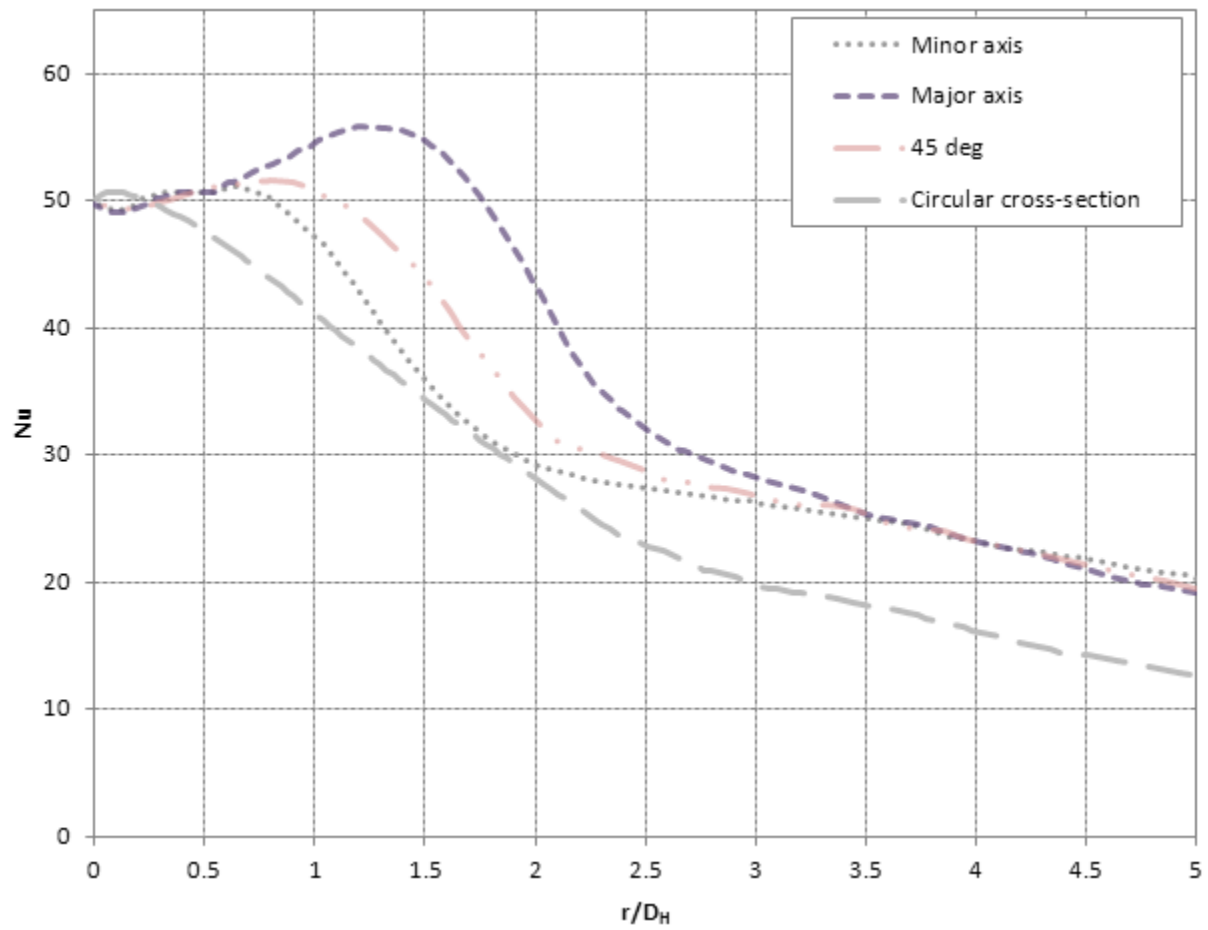
Figure 6-23: Nu values for elliptical nozzle at Re=6000 and H/D=6
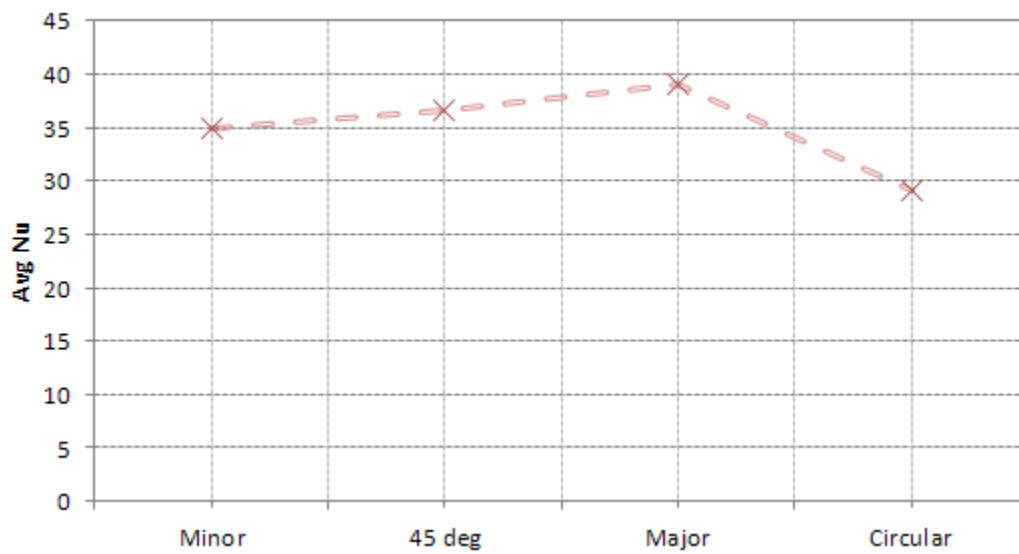
Figure 6-24: $\overline{Nu}$ for elliptical jet compared to circular jet at H/D=6 and Re=6000

74

Geometric variation analysis of single impinging jets was also performed by Dano et al. [61] where an overall heat transfer enhancement was seen for cusped ellipse orifice. An extensive study was performed by Obot et al. [38] to determine the effects of nozzle inlet shape (contoured and sharp edged) and L_e/D on impingement heat transfer. Chambers [62] presents a computational and experimental investigation into the use of shaped elliptical or elongated circular impingement holes designed to improve the penetration of the impinging jet across the coolant passage.

As before, the heat transfer results can be best understood by the velocity contours and have been added for the different regions in the impinging domain in Figure 6-25. It can be observed from the figure that the velocity values obtained are similar for the three regions in the figure, except that the width of the potential core has increased tremendously for the major axis compared to the rest. It is seen that the jet is not influenced much by circulating air and penetrates easily through to stagnation. Also, the entrainment of air is reduced due to increased plan-form area in the major axis when compared to the circular jet case in Figure 6-3. This increased stagnation zone area protects entrainment of air and is the reason for higher overall heat transfer in an elliptical case. The velocity magnitude at stagnation point by definition should be zero; this is confirmed by the contours in the same figure. This also causes the maximum heat transfer to be shifted away from the stagnation zone itself, as convection effects are negligible. Although entrainment of air is reduced due to increment in stagnation zone (due to geometry), entrainment itself is also the cause for the widening of jet from the nozzle exit. The local Nu contours have also been added for better representation and comparison purposes in Figure 6-26.

Comparing the pressure profiles for the elliptical jet in Figure 6-27, Figure 6-28 and Figure 6-29 to circular jet case in Figure 6-8, Figure 6-9 and Figure 6-10 respectively, it is seen that the static pressure profile is enlarged and higher pressure values are observed for the elliptical jets. Thus, the high static pressure values obtained (the dynamic head is reduced to zero, allowing the static pressure to rise) is the true cause of impingement heat transfer and is not the convective heat transfer (at stagnation when velocity is zero, heat transfer values are still comparably high although not the maximum recorded). The scale has been adjusted for easier comparison to circular jet case. The dynamic pressure at the center is zero and the area of the stagnation zone is

larger compared to the circular case. The increase in dynamic head is however larger at the apex of stagnation zone. Finally, the total pressure provides an overall view of the pressure profiles felt by the target plate and the reasons for the higher heat transfer values in elliptical jets. Hence, the effect of changing the nozzle geometry has a significant relation to the heat transfer values obtained.
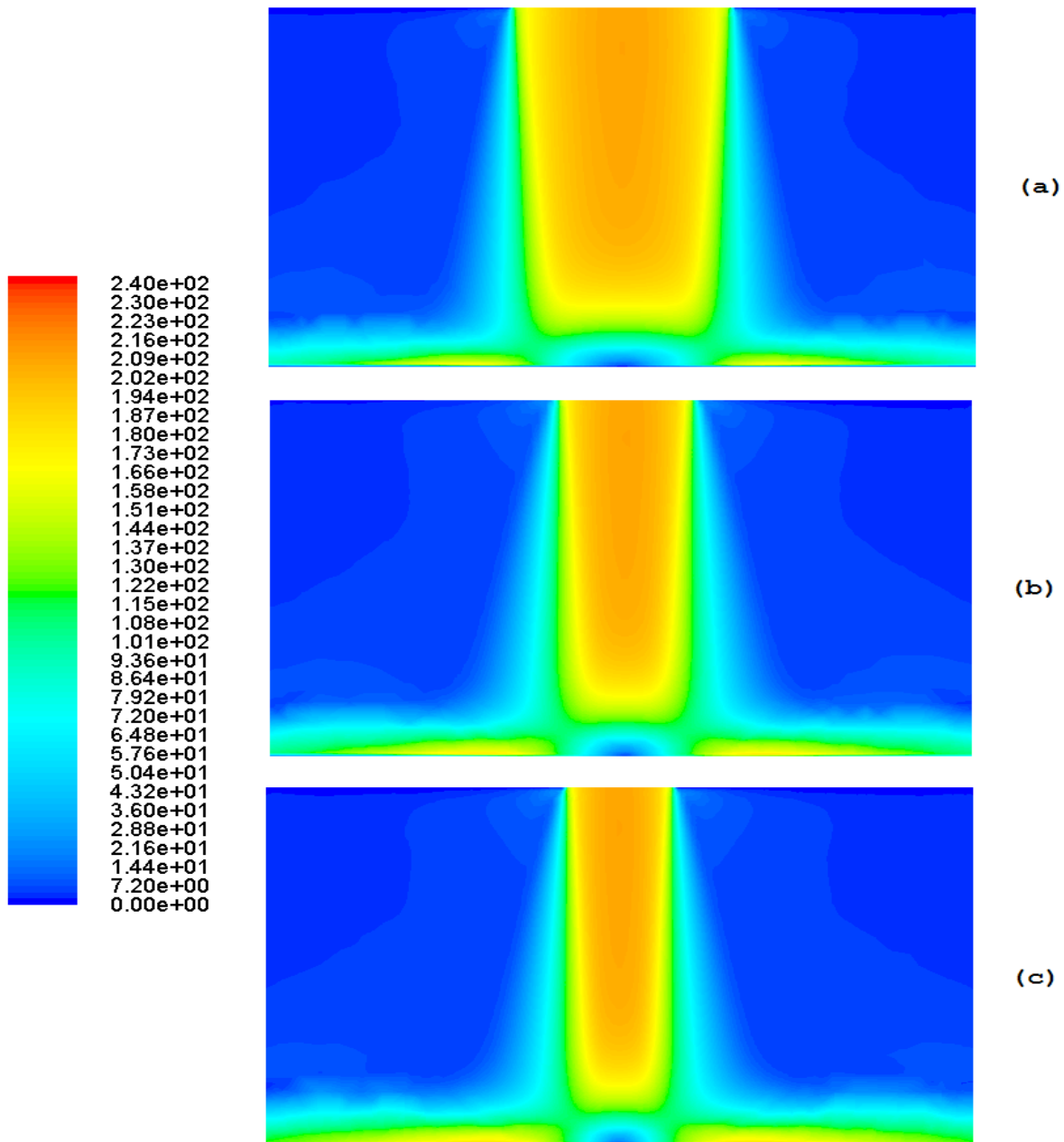
Figure 6-25: Contours of velocity [m/s] for elliptical jet
(a) Major axis (b) Bisecting axis (c) Minor axis
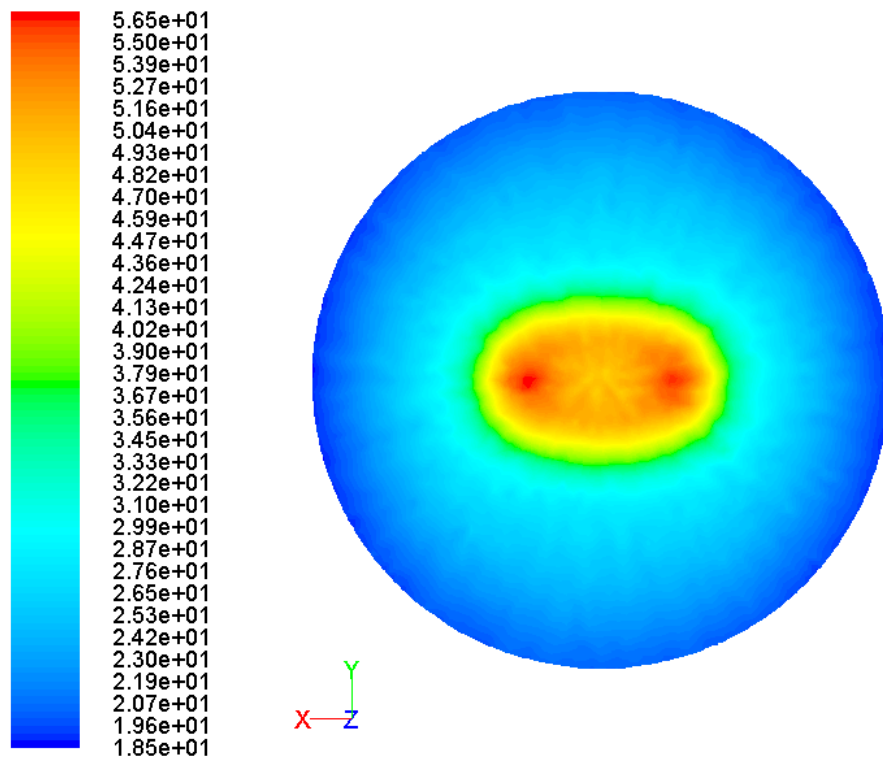
Figure 6-26: Local Nu contours for elliptical case
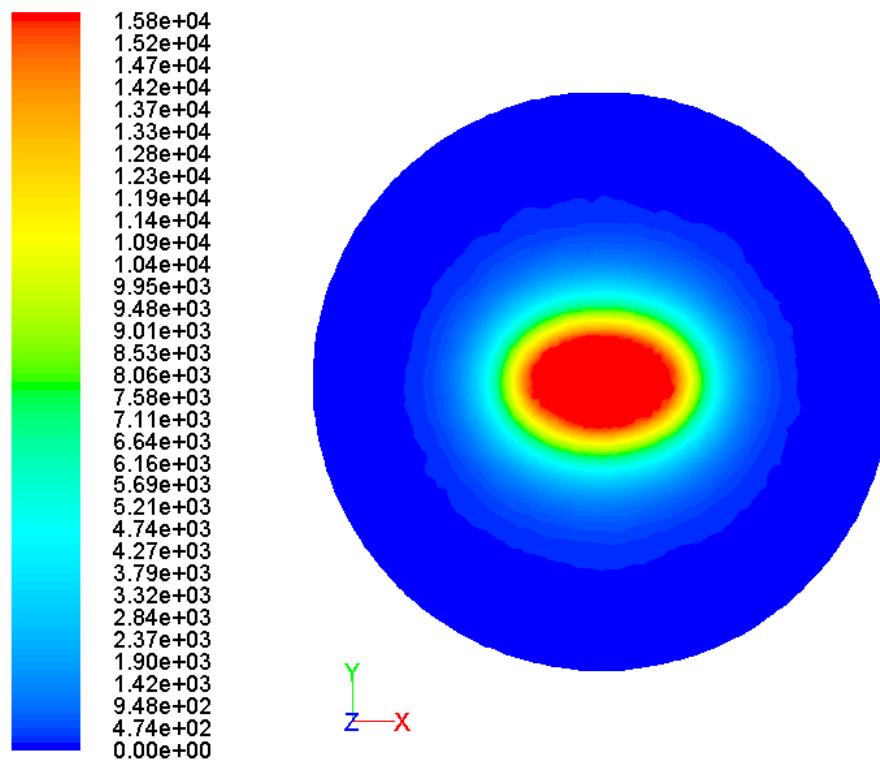
Figure 6-27: Static pressure contours (gauge) [Pa] for elliptical jet
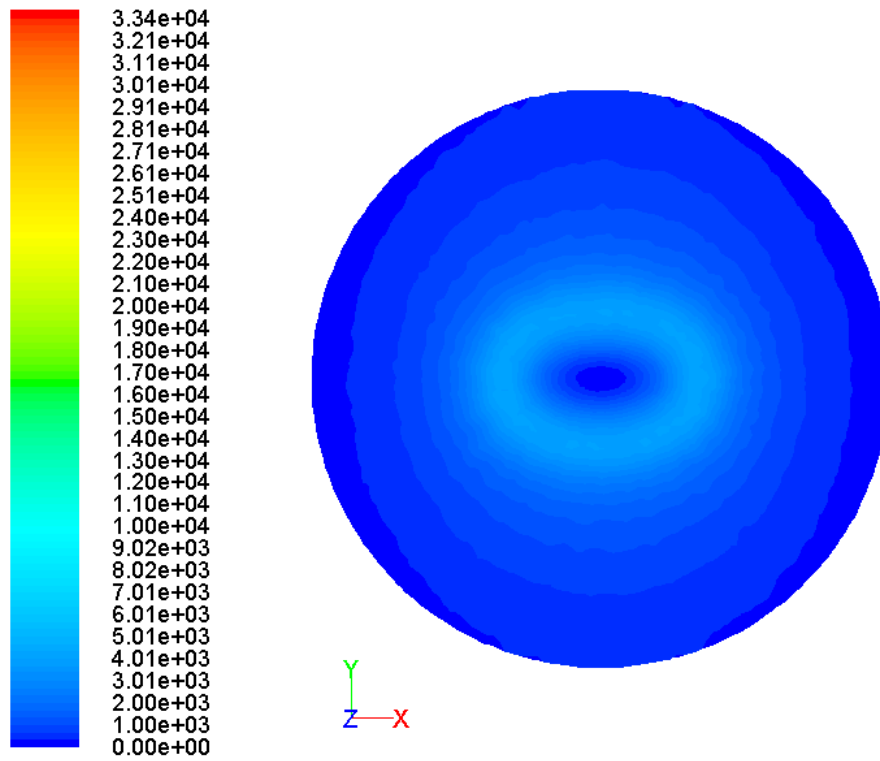
Figure 6-28: Dynamic pressure (gauge) [Pa] for elliptical jet
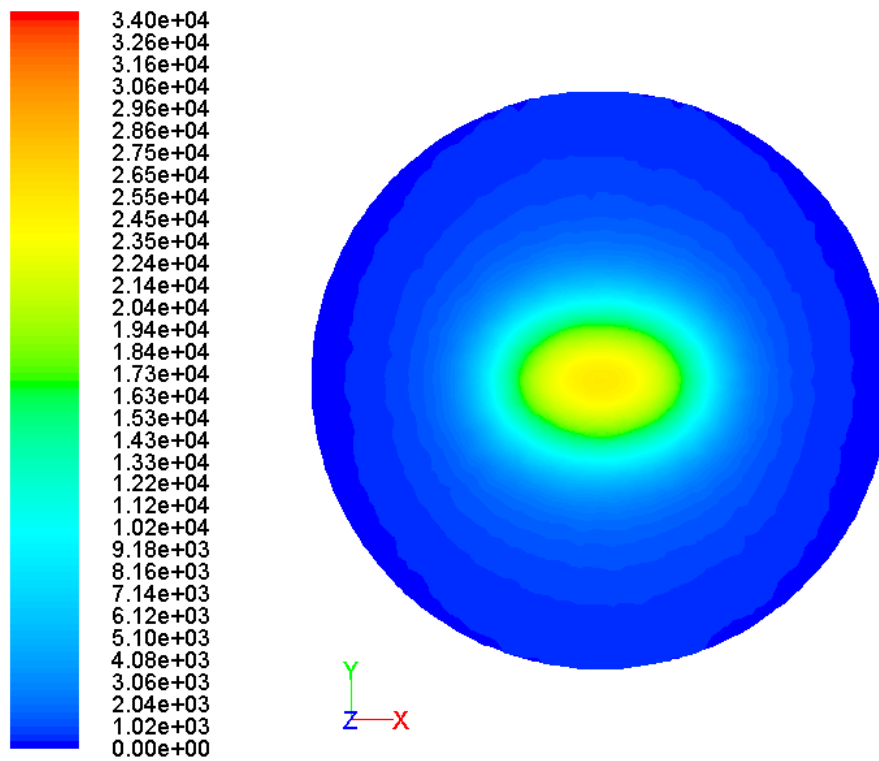
Figure 6-29: Total pressure (gauge) [Pa] for elliptical jet

78

6.2   High Pressure Turbine Vane Model

6.2.1   Validation

Validation of the model was performed against numerical work of Leon De Paz [26][15]. The geometry of the validation vane was previously depicted in Figure 4-7 (b). The averaged spanwise pressure at each jet exit is obtained for each row and normalized against plenum pressure. The result is plotted in Figure 6-30 for jets numbered successively starting at zero for leading edge and covering the suction and pressure surfaces. The maximum relative deviation between the two cases for the normalized pressure was found to be about 0.09%.

Local Nu values were also mapped in Figure 6-31 to assure validity of the vane for further analysis. The abscissa in Figure 6-31 is the curved length of pressure surface which is non-dimensionalized by the diameter; and, the ordinate is the Nu extracted for the middle column of jets as shown in the red band in Figure 6-32. The maximum relative deviation between the predicted results and that of reference [26] for local Nusselt number was around 6.4% near the trailing edge. The reason for the high deviation near the trailing edge may be due to the geometry used by Leon De Paz [26]. The complete blade geometry was not defined in reference [26] and almost all of the profiles were traced out while the validation model used herein was constructed using co-ordinate points provided in NASA Technical Report by Timko [42]. Another reasoning for the deviation near the trailing edge may be that the trailing edge radius was not specified and for both cases (Validation model used herein and geometry used by Leon De Paz [26]) were traced out. The inlet turbulence intensity could also add to the deviation obtained. The inlet turbulence intensity was calculated using equation (5.2). It was assumed that reference [26] used default Fluent values as no mention about turbulence intensity was specified. The deviations that could be observed (for single jet) due to this effect is explained in section 5.1.3. Otherwise, the Nu profiles obtained using the validation vane agrees well with the Nu distribution obtained by Leon De Paz [26] and using equation (3.7). Using the sensitivity analysis as described in section 5.2.3 and the validation results for key parameters checked, the mesh is considered independent of discretization and mesh errors and valid for further analysis.

---

[15] Validation for the vane against experimental results (flat plate with corresponding conditions) has been performed; see reference [43] for more information.
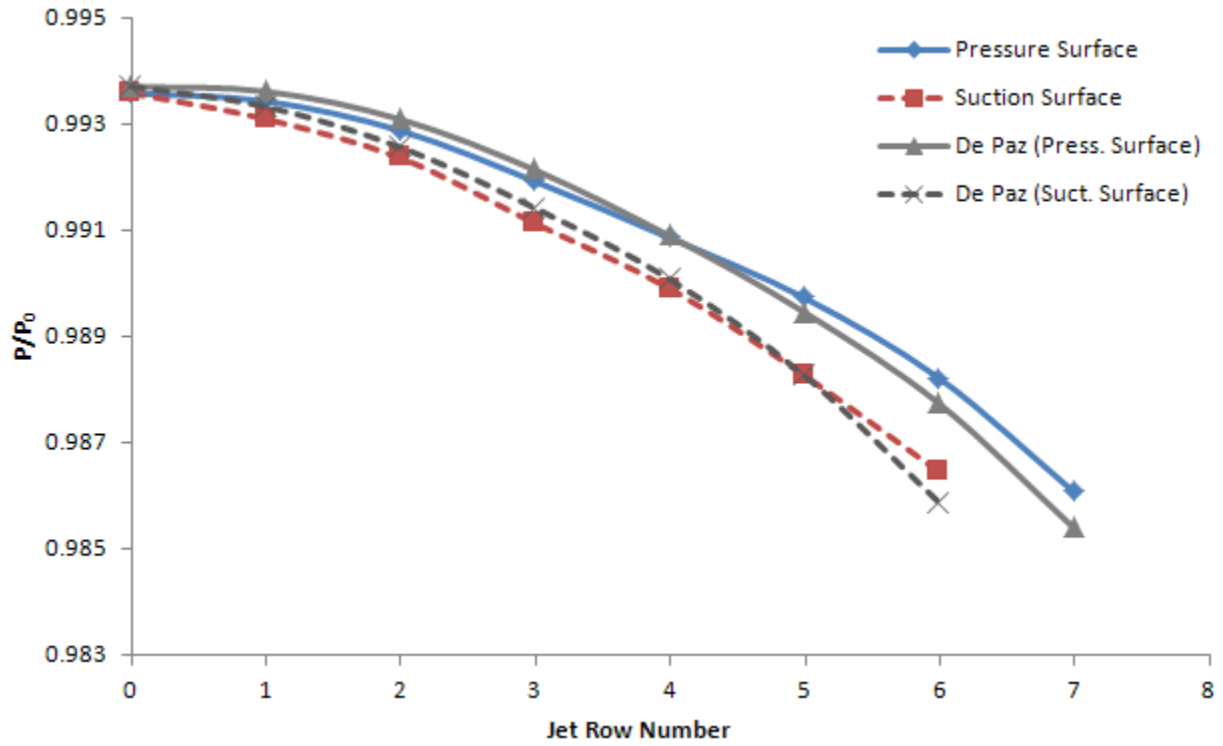
Figure 6-30: Normalized pressure at jet exit for each jet row starting at leading edge
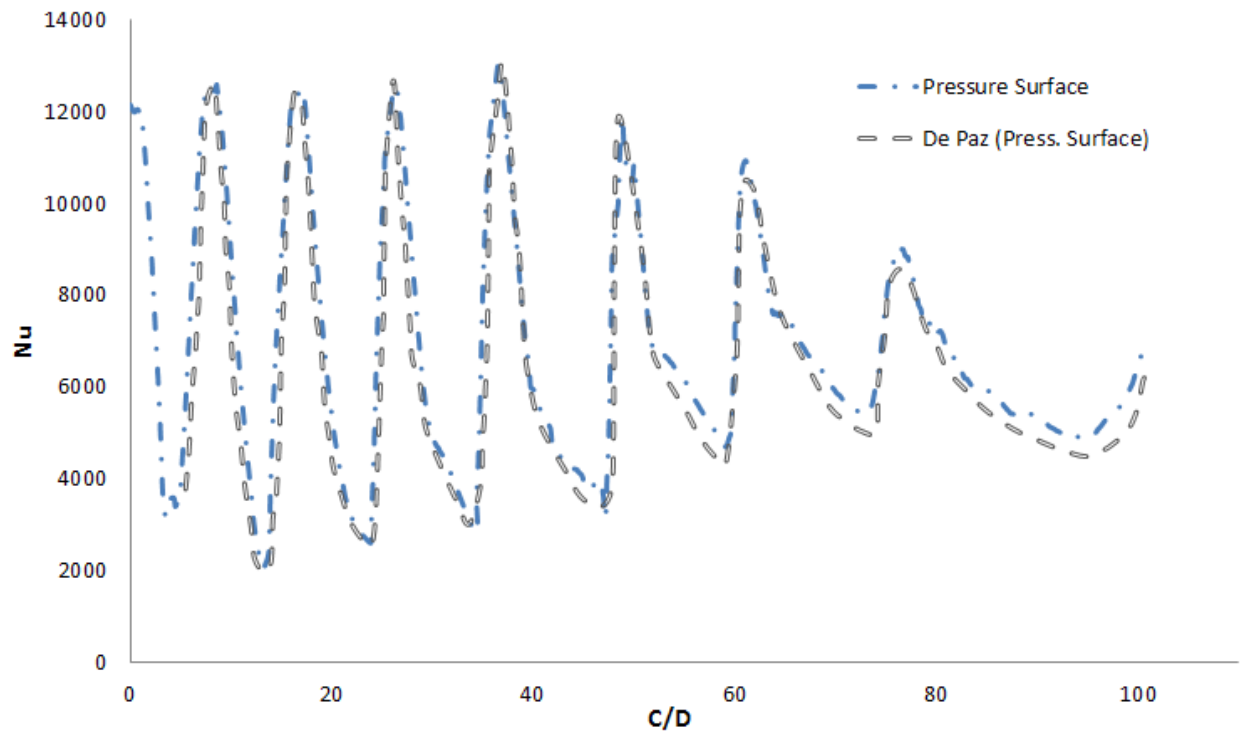
Figure 6-31: Nu for non-dimensional curve length on pressure surface along mid-plane of jets
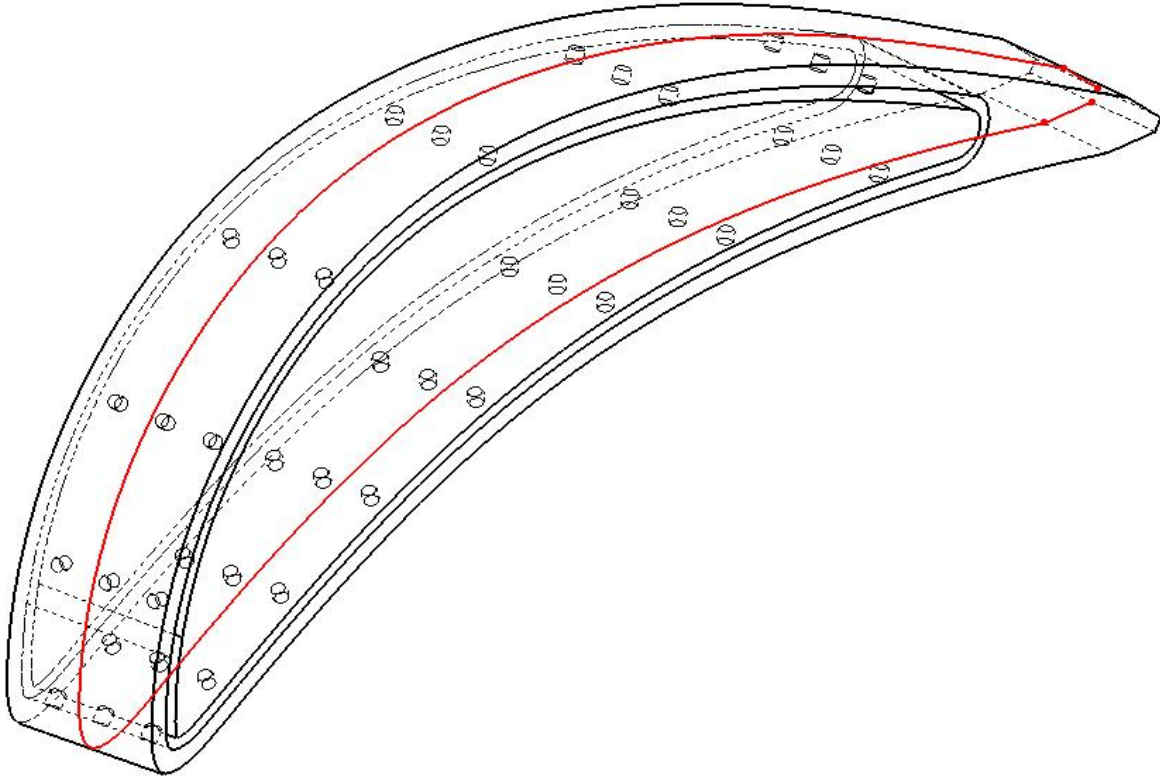
Figure 6-32: Extraction of local heat transfer results at the line-segment shown in red

6.2.2 *Hydrodynamics for Base Vane*

The geometry of the base vane is presented in Chapter 4, Figure 4-7 (c), and is initially compared to the validation vane in Figure 4-7 (b). Flow propagates in the direction of tapering (-Z direction) and the local Nu values are observed to increase compared to the validation vane as observed in Figure 6-33. The values are computed at the red line lying on the target surface which passes over the middle column of jets as shown in Figure 6-32[16]. The maximum percent increase in the stagnation Nu value was recorded to be about 10.3% due to the change in airfoil profile from the validation model. The average Nu value increased by 5.9% compared to the validation model. It is interesting to note that the change was obtained for a span of only 12 times the diameter ($510 \ \mu m$).

---

[16] For the base model, the L_C is located at the same span (50%) where the strip is positioned; L_C is the same for the validation vane. This was done for comparison purposes. Also, L_C, the chord length, was calculated from leading edge to the trailing edge of the true airfoil outer surface and not the airfoil inner-surface.
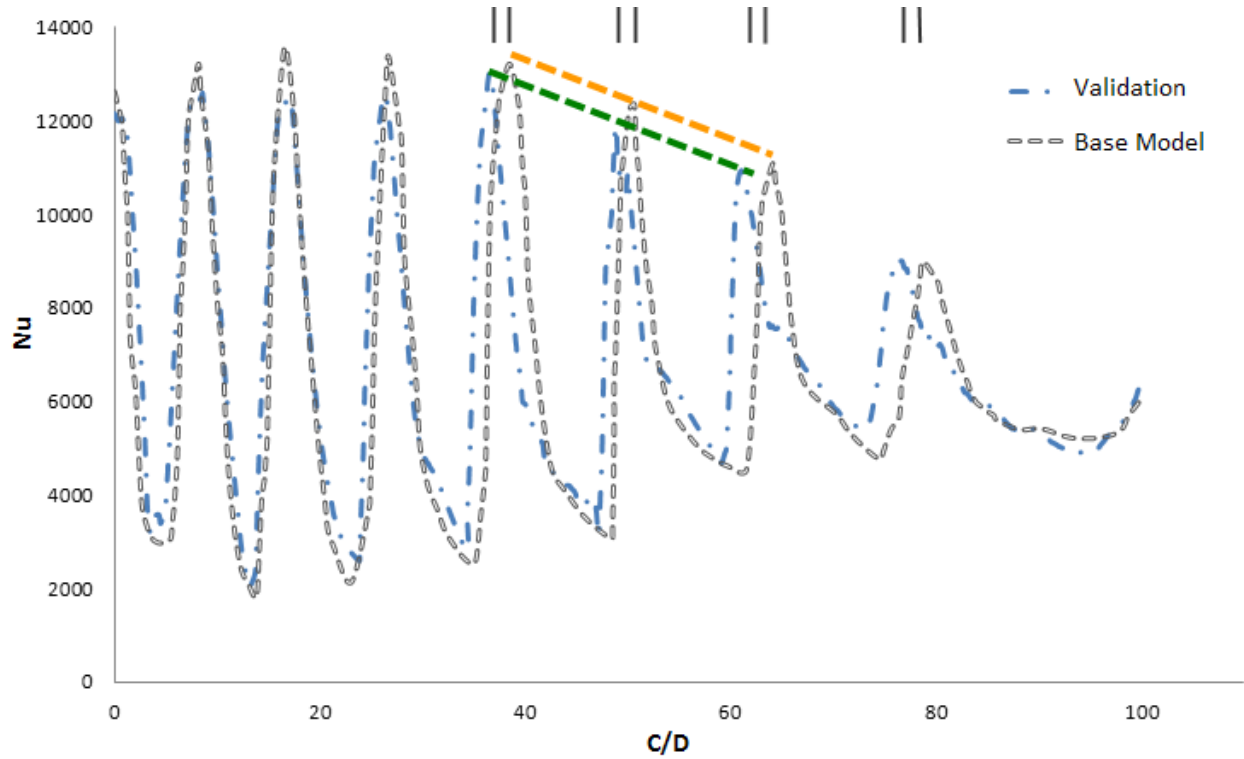
Figure 6-33: Local Nu distribution for validation vane and base vane on pressure surface

The increase in Nu values can be related to the increase in the velocity at jet exit location for the two cases shown in Figure 6-33. The exit velocity is shown in the section view of the plane through the 6th row of jet on the pressure surface (see Figure 6-34). Clearly, the increase in jet velocity is seen in going from Figure 6-34 (a) to Figure 6-34 (b). The average velocity at exit for jet row number 6 on the pressure surface, middle column, of the validation vane was 46.93 m/s whereas the average for base model was 52.3 m/s or an 11.4% increase[17].

In terms of the change obtained from columns 1 to 3, the validation model does not represent any noticeable change in velocity[18]. On the other hand, for the base model, the exit velocity increases in the -Z direction, also showing increased effective heat transfer. The average exit velocities from left to right in Figure 6-34 (b) are 47.6 m/s, 52.3 m/s and 58.1 m/s or a 10% and 11% increase respectively. The length of the potential core is also seen to increase due to the increase in the exit velocities.

---

[17] The rows are numbered successively from the leading edge to the trailing edge starting at row zero for leading edge.
[18] The columns are numbered successively in the direction of the flow (spanwise) starting with column 1.

The major contributor to the increase in Nu value for the base vane is the tapering of the airfoil in the spanwise direction in the meridional view plane. The tapering of the geometry increases the effective velocity at the jet exit. Contours in Figure 6-35 and Figure 6-36 depict the change in jet exit velocity while moving in the direction of inlet flow (spanwise, in the −Z direction). The plenum flow direction and the direction of impingement are also shown in the same figures. The term target in the images denotes the targeted airfoil inner surface to be cooled. Also, it is interesting to note that the velocity increases at the jet exit while moving in the streamwise direction, i.e. from leading edge to trailing edge as seen in Figure 6-35 and Figure 6-36. The overall fluid velocity also increases in the same direction due to the build-up from upstream jets. This is due to the cross-flow effect discussed below. Although the velocity is seen to increase in the streamwise direction, the length of the potential core diminishes as in Figure 6-35 and Figure 6-36. The velocity distribution across the planes passing through the three columns of jets is also shown in Figure 6-37.
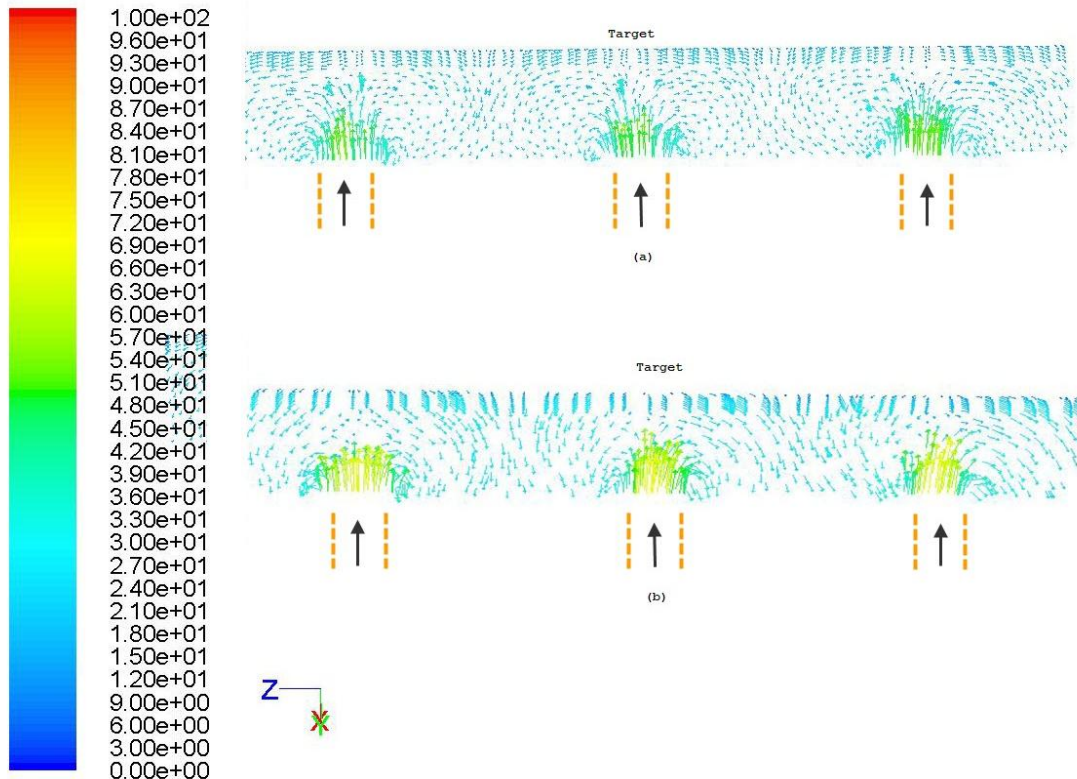
Figure 6-34: Jet exit velocity vectors [m/s] for the 6th row on the pressure surface.
(a) Validation Model (b) Base Model

83
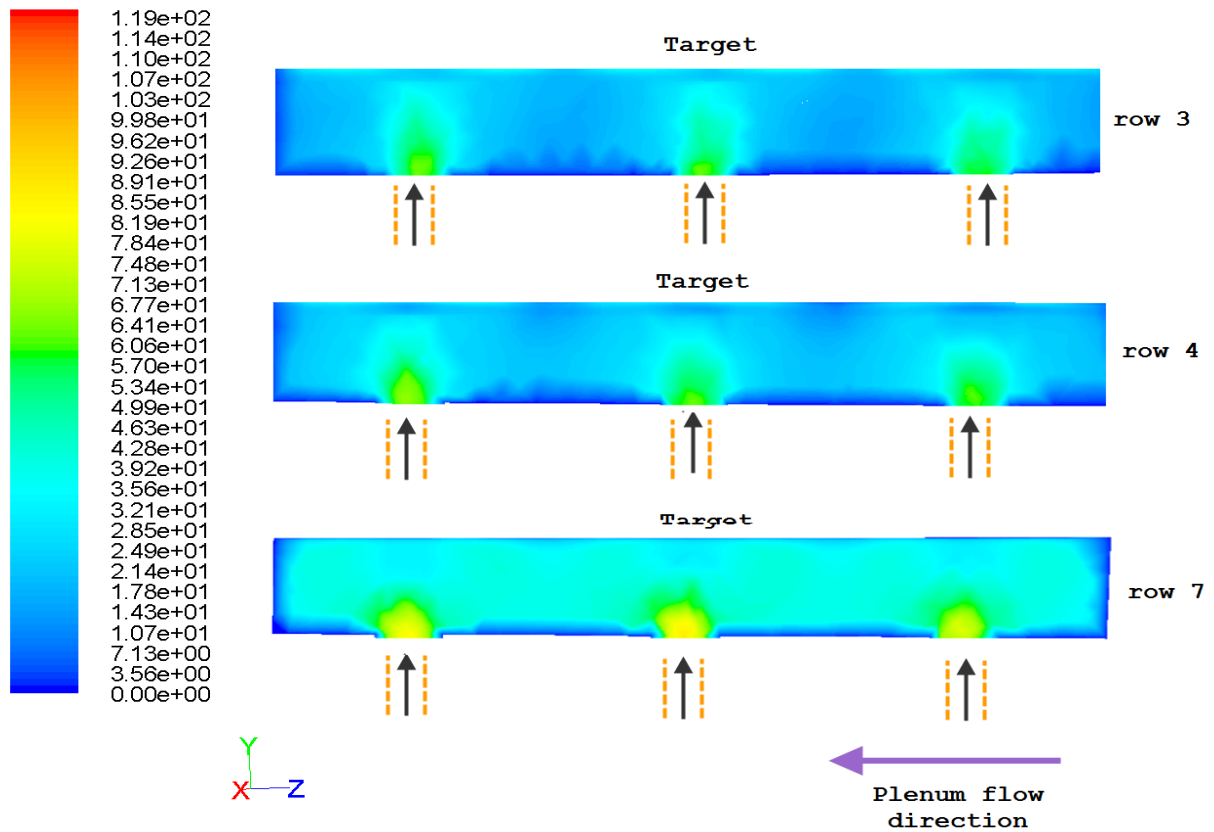
Figure 6-35: Velocity contours [m/s] on planes cutting across pressure surface jets
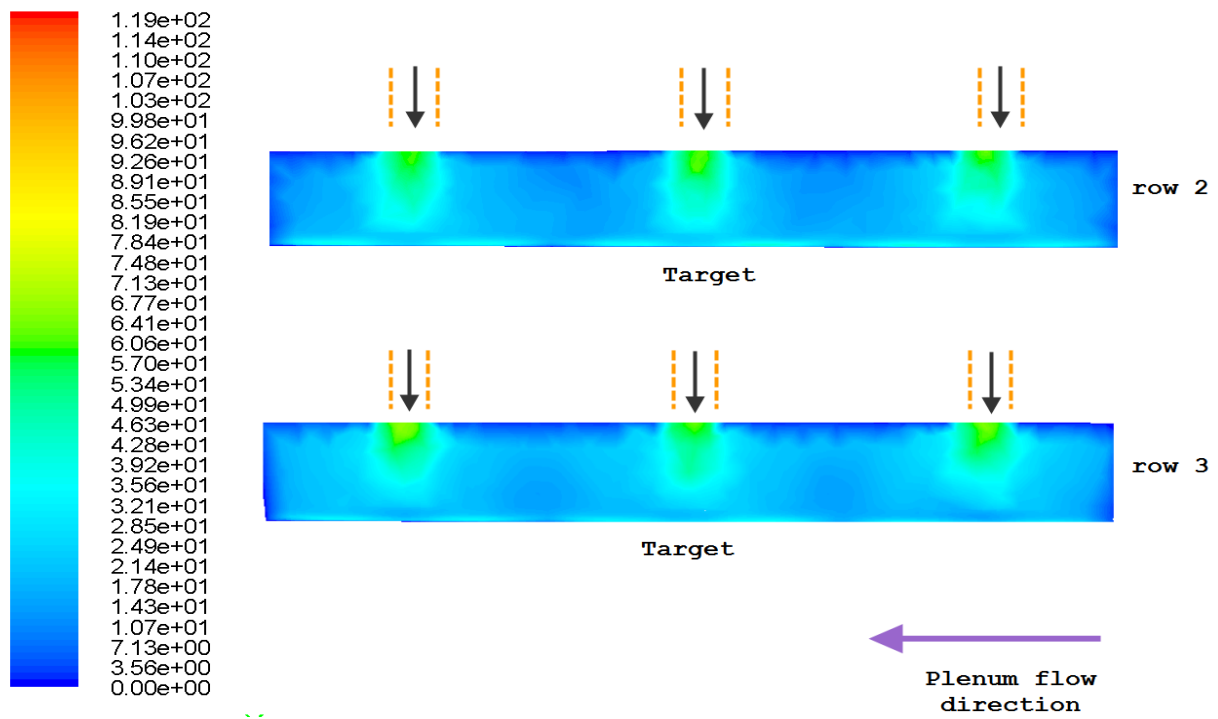
Figure 6-36: Velocity contours [m/s] on planes cutting across suction surface jets

84
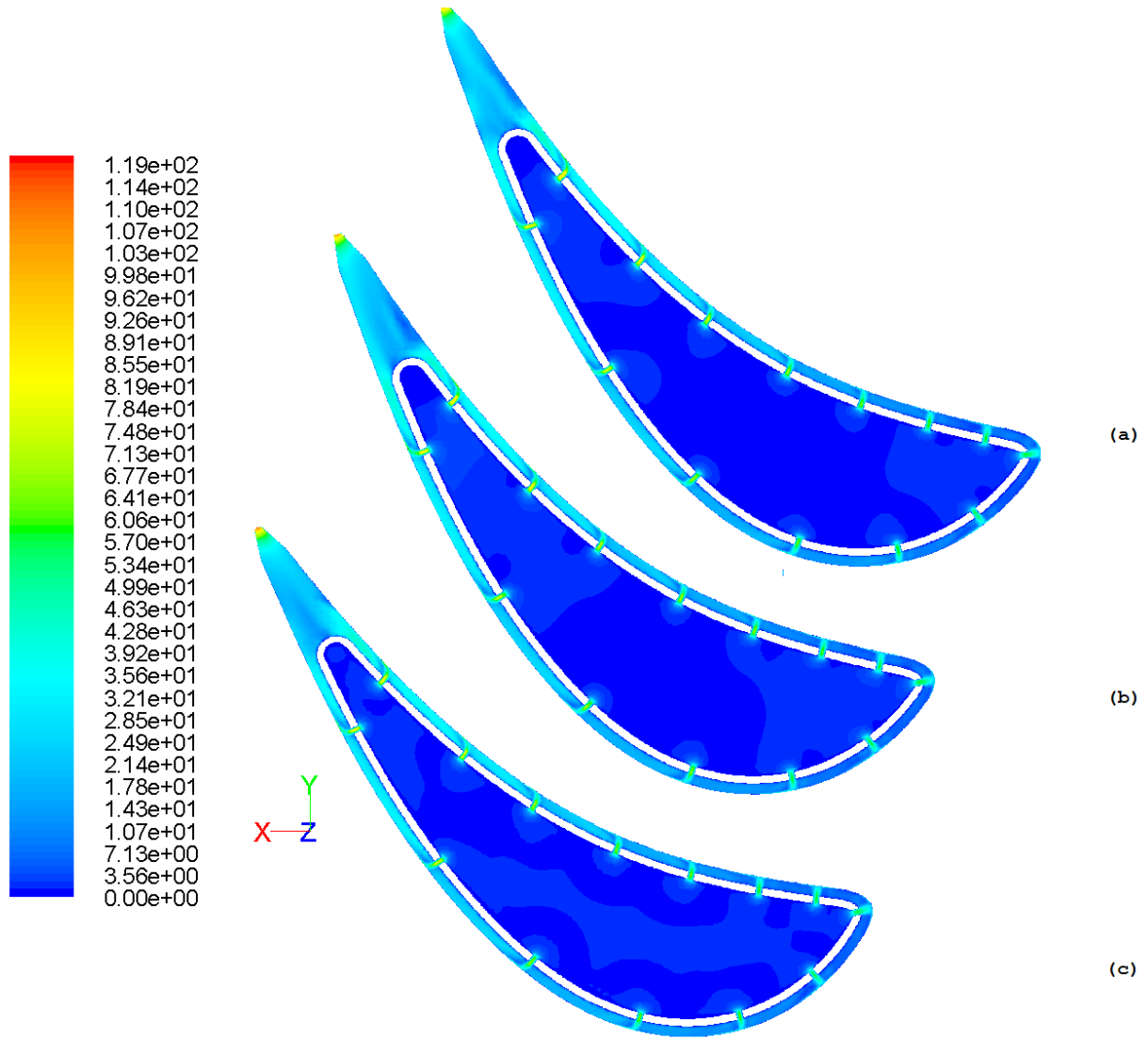
Figure 6-37: Velocity distribution for base model (a) Column 1 (b) Column 2 (c) Column 3

The effect of streamwise cross-flow becomes prominent starting with the 4th jet (Figure 6-33); and, as the cross-flow increases moving downstream, the position of the stagnation point shifts away from the jet center location in the direction of cross-flow; this has been marked by vertical lines at the top of Figure 6-33. Similar cross-flow effects were obtained by numerical work of Leon De Paz [26] and experimental work of Gao [63]. For jet rows 1 through 4, the local heat transfer tends to perform well, increasing marginally. It was realized that the streamwise cross-flow velocity here was less than 10% of the jet average velocity. Such enhancement was seen experimentally by Gao [63] where surface heat transfer was enhanced by low cross-flow velocities. Examination of cross-flow interactions and its influence on heat transfer was

85

performed by Wang et al. [64] using a 3-D transient liquid crystal scheme. In general, it was seen that the jet momentum and the cross-flow buffering effect are in constant competition. When the jet momentum is higher, the jet flow penetrates and local heat transfer values are high. When the cross-flow momentum is higher than the jet flow, a horizontally stretched pattern (almost uniform) of heat transfer is seen. The figure below (Figure 6-38) shows one of the jets experiencing the cross-flow effect.
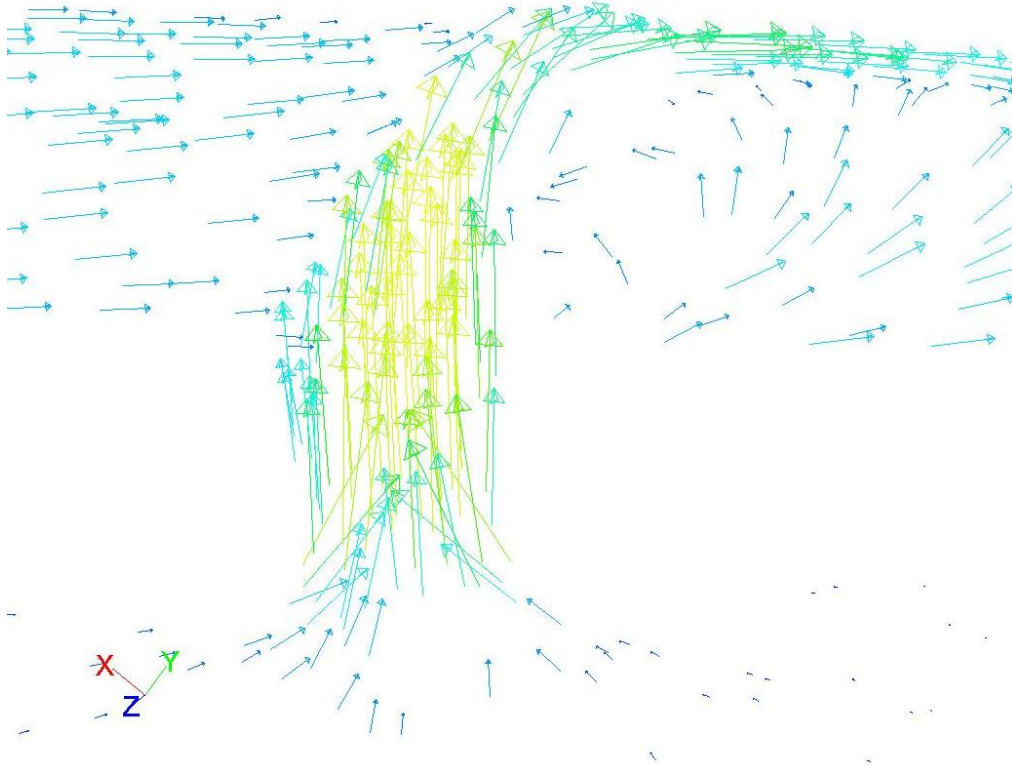
Figure 6-38: Jet experiencing cross-flow effect

In comparison of the two models shown in Figure 6-33, the slope of the drop in stagnation values due to cross-flow was found to be the same (shown in orange and green lines; the magnitude approximately being -100.5) with the vertical distance between them providing the increase in Nu value and horizontal distance the shift in stagnation value (~2.75D). The region in between the jets illustrates the effects of forced convection with the least increase in heat transfer at the exiting flow near the trailing edge. Nu contours also explain the above phenomena. Careful examination of Figure 6-39 (a) reveals the qualitative determination of cross-flow effect. For a single jet, the shape of Nu distribution remains uniform in all directions [1]; however in array of jets the shape changes based on location. The center jet in the figure below is subject to cross-

flow from the edge jets and vice versa; also, the jets are subject to spent air from upstream direction. The simplistic sketch (Figure 6-39 (b)) explains the effect of cross-flow from upstream and edge jets on Nu. In other words, the Nu contour shape expresses the local flow direction.
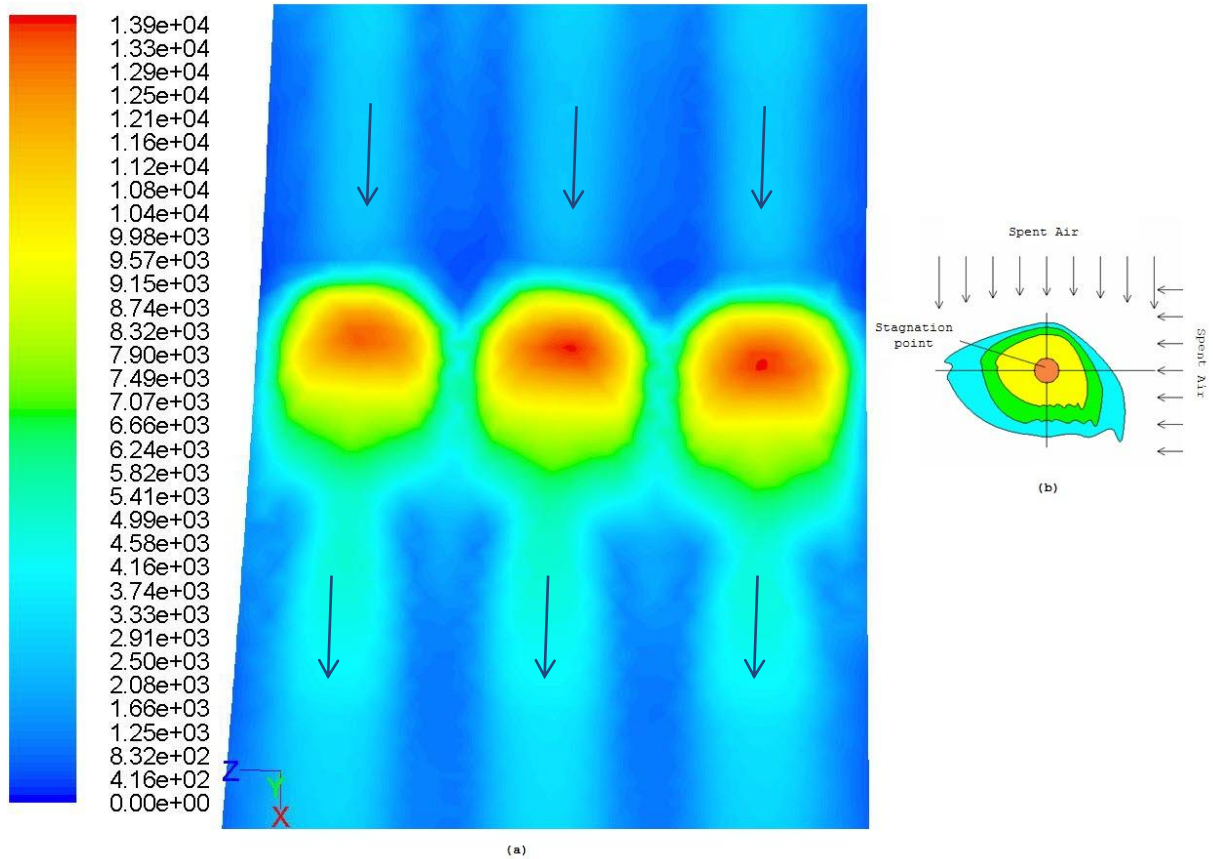
Figure 6-39: Nu contours for jet with cross-flow effect.
(a) Base vane (b) Simplistic sketch [63]

In Figure 6-39 (a), the plenum flow is in the -Z direction. The impingement flow is moving into the paper where the stagnation zone is seen in red as the jet impinges on the airfoil surface. The arrows show the direction of the streamwise cross flow build-up due to the upstream jets. The influence of cross-flow for multiple jets on heat transfer was experimentally studied by Bouchez and Goldstein [65]. Flow visualization results showed that the interaction between the cross-flow (streamwise and spanwise) and impinging jets made the flow highly three-dimensional, which increased the complexity of the flow structure and the heat transfer distribution. Heat transfer coefficients in general were seen to reduce due to these complex flow interactions. Moreover, investigation of cross-flow effect performed by Wang et al. [64] showed that not only is the flow

three dimensional but also that the heat transfer distribution is highly non-uniform due to the complex 3-D flow structure. Figure 6-38 displays the velocity vectors representing the flow structure due to cross flow effect.

The pressure distribution across the array is of great interest as it affects the exit velocity of the jets, the cross-flow, and therefore, the heat transfer coefficient at each jet row. The absolute pressure is highest in the plenum chamber as represented in Figure 6-40; using the ideal gas law (equation (3.3)) with equations (3.1) and (3.4), allows the micro jets to behave with no slip condition. In the impingement chamber the pressure decreases in the streamwise direction. Thus, the lowest pressure point is found at the trailing edge of the vane. The decrease in pressure can be attributed to the increase in the streamwise crossflow velocity. Using Figure 6-30 as a reference, the overall pressure drop across the suction surface jets and pressure surface jets are relatively the same. The suction surface and pressure surface curves do not overlap in the figure because of the difference in the number of jets on these surfaces. If pressure values are compared at the same curve length (as opposed to jet row number), the absolute pressure on the pressure surface is higher than that on the suction surface. And, the lower pressure at a given curve length on the suction surface yields higher streamwise cross-flow momentum compared to the pressure surface. The lower absolute pressure on the suction surface and the lowering of pressure along the streamwise direction favours the cross-flow momentum due to the increased mass (from upstream spent air) when compared to the jet flow momentum. Since the cross-flow momentum overpowers the jet flow momentum in the streamwise direction, the cross-flow impedes the performance of the impinging jet by reducing the exit Re number. Since the suction surface observed lower pressure, it implies the cross flow momentum shall be higher on the suction surface and hence the impinging jet exit Re shall be degraded for the suction surface when compared to the pressure surface. This is verified using the Re distribution for the jet row numbers graphed in Figure 6-41. Comparing jet 7 and 5 (they are almost at the same curve length from leading edge) from the pressure surface and suction surface respectively, higher Re is achieved at the pressure surface compared to suction surface. Jet row numbered zero represents the leading edge jet and the jets are successively moving in the spanwise direction as mentioned previously.

88
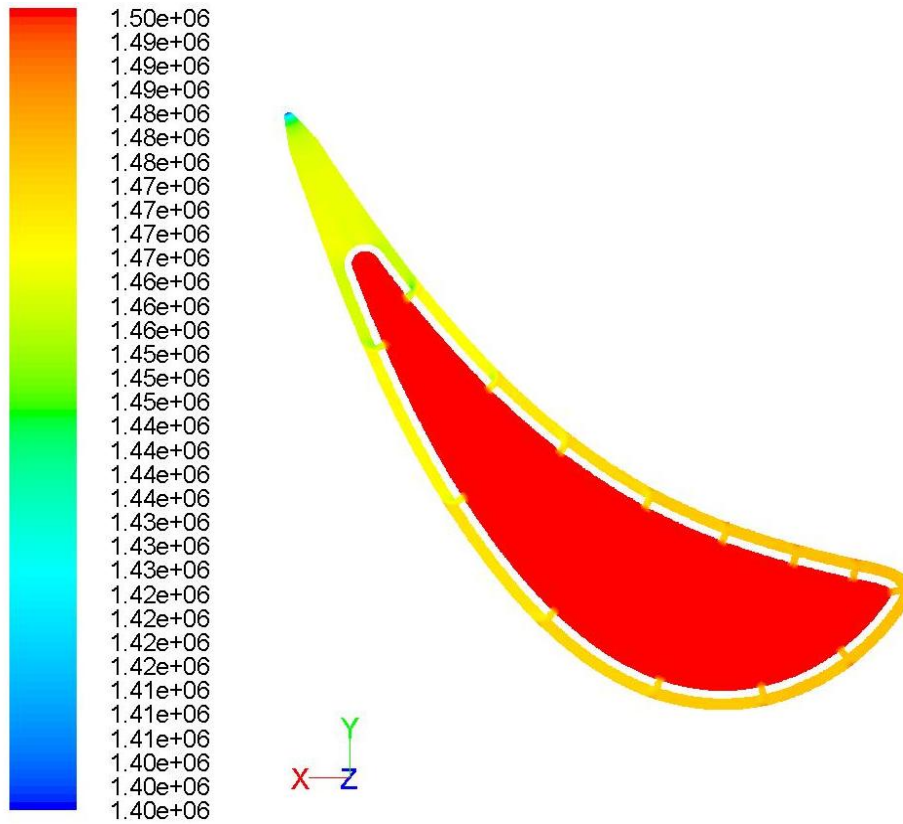
Figure 6-40: Pressure contours [Pa] for base vane
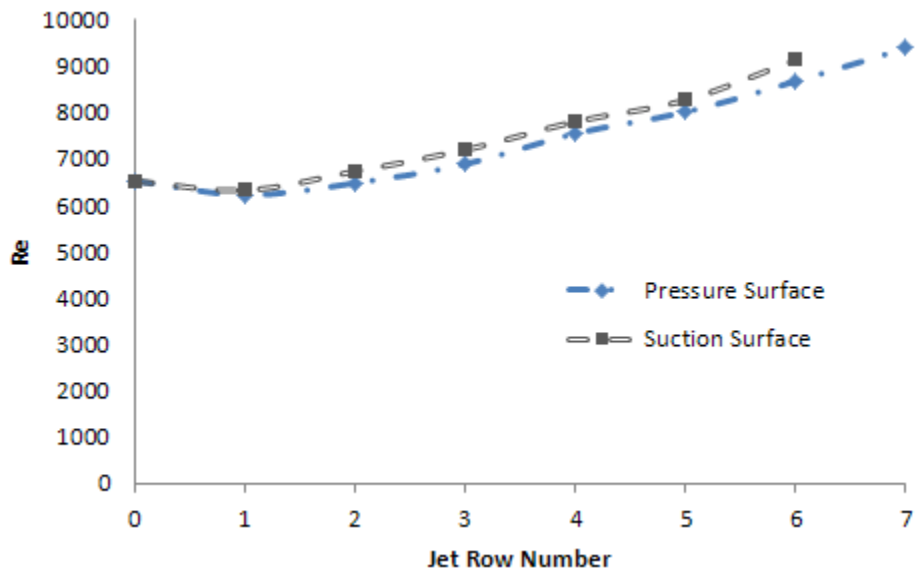
Figure 6-41: Reynolds number distribution at jet exit

As with the single jet case, the static and the dynamic pressure explain the effectiveness of the heat transfer due to impinging flow or convective flow. The total pressure contour is presented in

Figure 6-42. At the stagnation point the velocity is zero and the dynamic head of the impinging flow completely transforms to a static pressure rise which equals the total pressure at the point. The red spots in Figure 6-42 (a) near the leading edge until around mid-cord region show the high static pressure and turbulent mixing at the boundary layer, hence producing maximum heat transfer at the stagnation zone. The boundary layer in this region is thin, highly turbulent and it is newly formed at each stagnation region. It is because of the excessive mixing that the red spots seen in Figure 6-42 (a) are larger than the ones seen in Figure 6-44. The increased velocity due to the accelerating flow around the stagnation zone increases the dynamic pressure as seen in Figure 6-45. Thus, the high momentum coupled with velocity fluctuations is the cause of high heat transfer coefficient around the stagnation region. Streamlines ejected from the jets show the complex flow pattern, the mixing and cross flow effect in Figure 6-43. Furthermore, the total pressure is seen to decrease in the streamwise direction due to the cross flow effect and the hence weakened dynamic head before impingement.
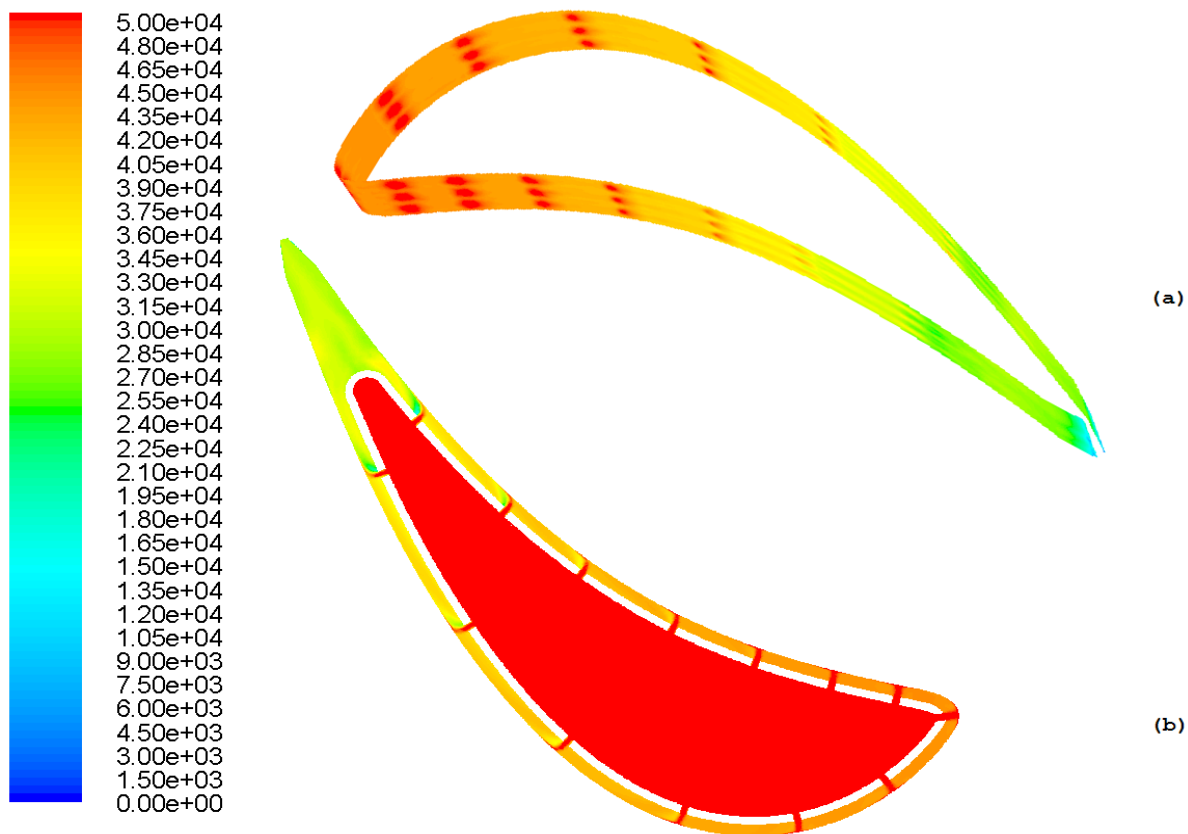
Figure 6-42: Contours of total pressure [Pa] (gauge) for base model
(a) **Target surface (b) Column 2**

90
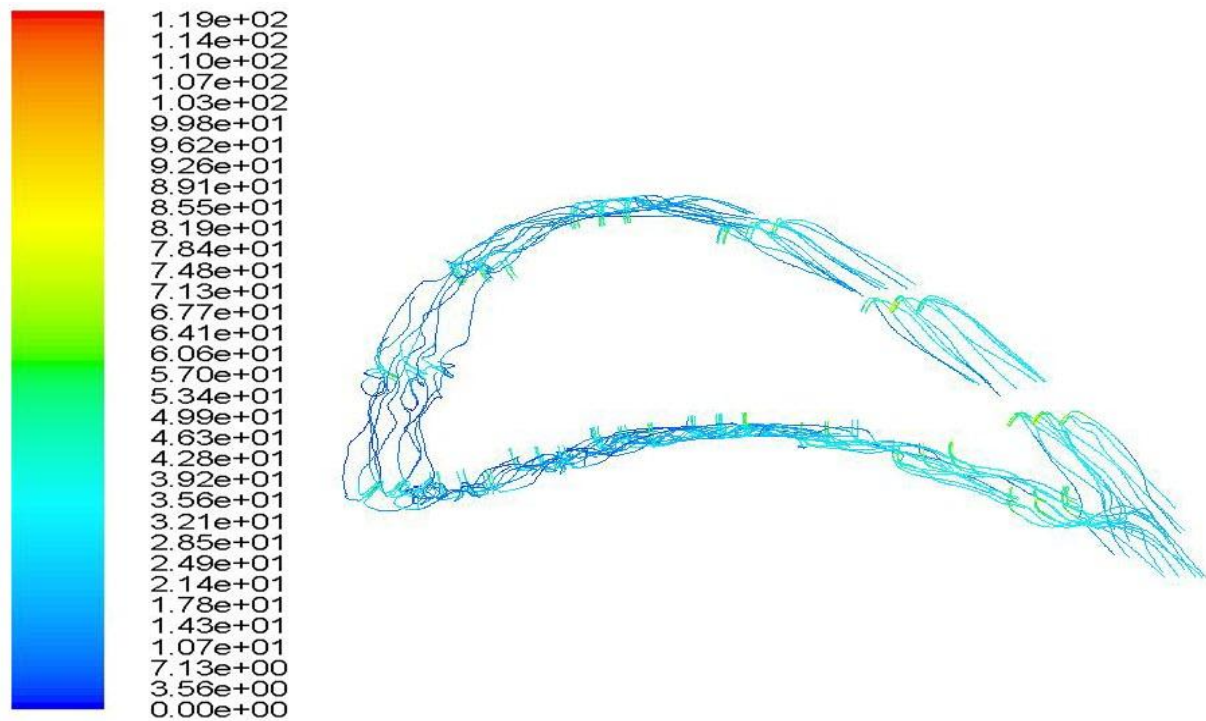
Figure 6-43: Streamlines based on velocity for the base model

(a)

(b)

Figure 6-44: Contours of static pressure [Pa] (gauge) for base model
(a) Target surface (b) Column 2
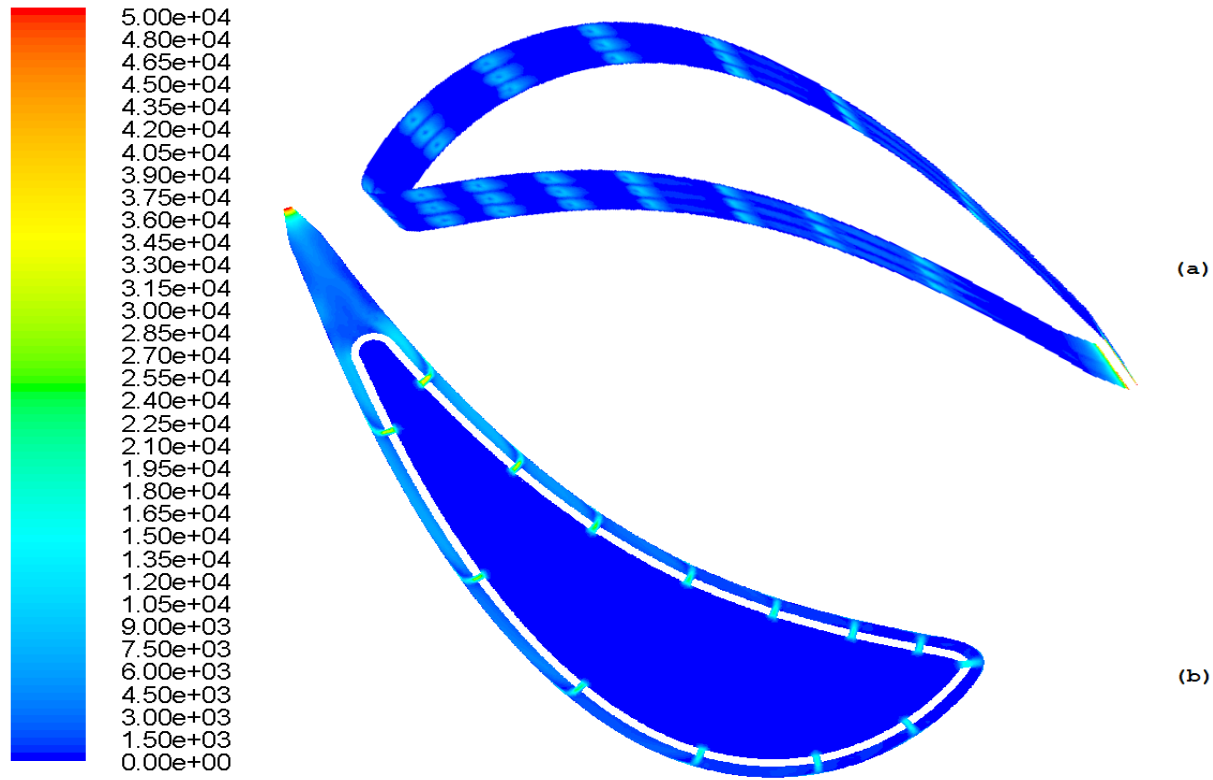
Figure 6-45: Contours of dynamic pressure [Pa] (gauge) for base model
(a) Target surface (b) Column 2

6.2.3 The Effect of Jet Inclination

Heat transfer distributions for impinging array of inclined jets are studied. Figure 4-8 shows jet configurations used. Jet holes are still 0.51 mm and the effect of inclination is compared to the base vane. The jets are aligned such that the target impingement co-ordinate remains the same to the base model. The flow pattern followed is: flow enters spanwise into the plenum chamber, enters the impingement hole inclined such that they are in the direction of streamwise cross-flow build-up (+45°) or oppose it (-45°) from the leading edge. The local Nu is plotted in Figure 6-46.

Examining +45° inclination, the stagnation values drop drastically providing reduced heat transfer at stagnation; this is due to the enhanced effects of cross-flow as the flow is directed in the same route. Similar analysis was performed by Huang et al. [23] where the jets were inclined in the same direction; however, the incoming flow was in the streamwise direction as opposed to the spanwise direction. Results obtained indicated that the inclined jets had less heat transfer

coefficient than straight jets. As mentioned earlier, the cross-flow effects are not apparent in the first few jets where the exit velocity is greater than 10% of the cross-flow velocity. The deviation of the stagnation point due to enhanced cross-flow is observed in the same figure marked by red vertical lines at the top. It is interesting to note that the effect of inclining the jet in the direction of streamwise cross-flow enhances the deviation of stagnation point from the base model; the deviations obtained are 2.5D, 3.95D and 6.25D. That is, the trend followed is similar to 2.5^1, $2.5^{1.5}$ and 2.5^2; where 2.5 is the coefficient of the first deviation. Enhancing cross-flow would mean enhancing the convective effects; this can be observed by viewing the slope of the Nu distribution curve. The slope instead of being steep like in the case of the base model is now comparatively gentle but spans a larger area. This results in the base of the fountain shaped distribution being wider as seen around the last three jets in Figure 6-46.
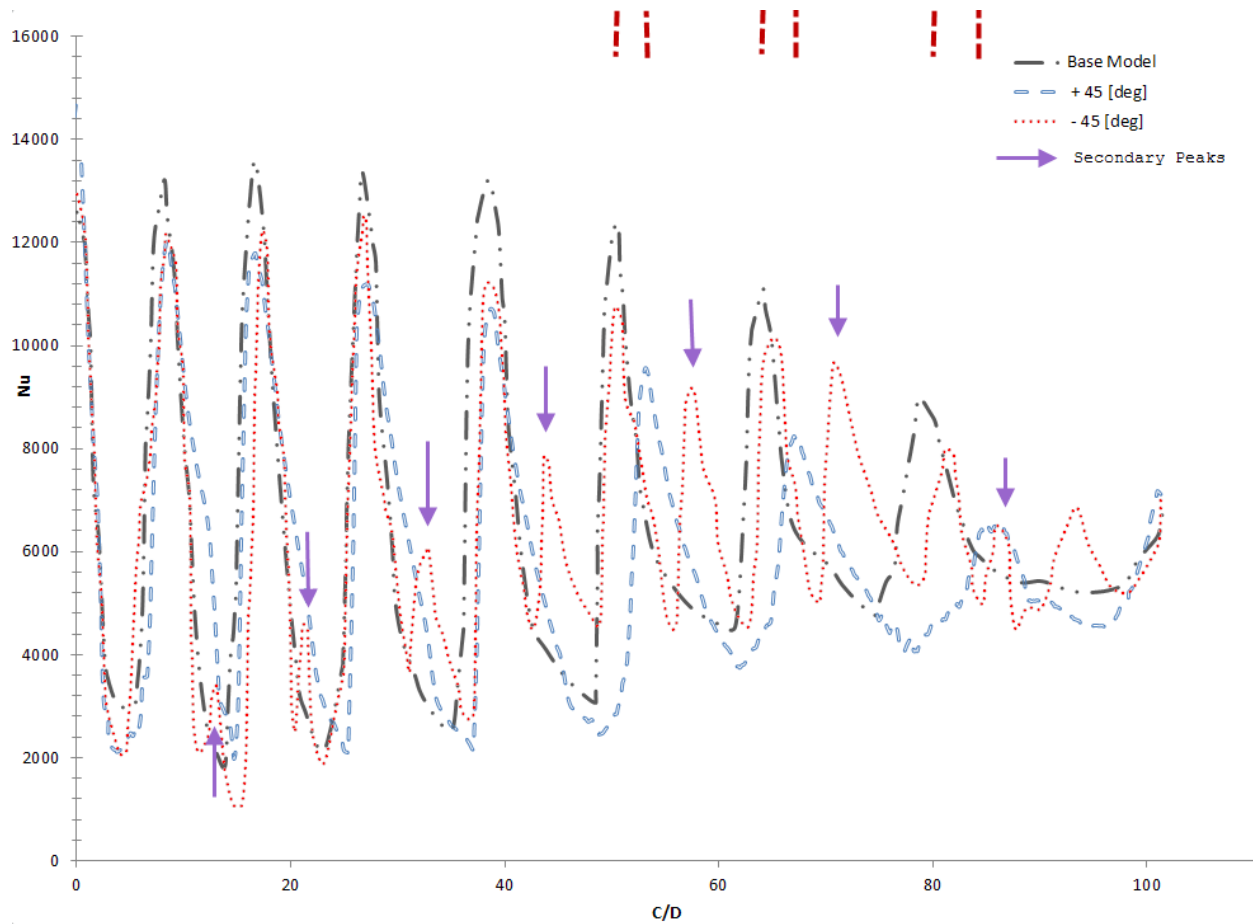
Figure 6-46: Nu distribution showing the effects of impingement jet angle on pressure surface
The red lines on top shows the streamwise shift in stagnation point for the last 3 jets for +45° inclination

93

The effects seen above can be observed in the velocity contours shown in Figure 6-47 and compared to the base model in Figure 6-37. Figure 6-47 (a) clearly shows the cross-flow diffusing the impinging jet and hence reducing the Nu effect. The difference in impingement heat transfer and convective heat transfer can be easily gathered form the same figure in conjunction with the Nu plot in Figure 6-46.
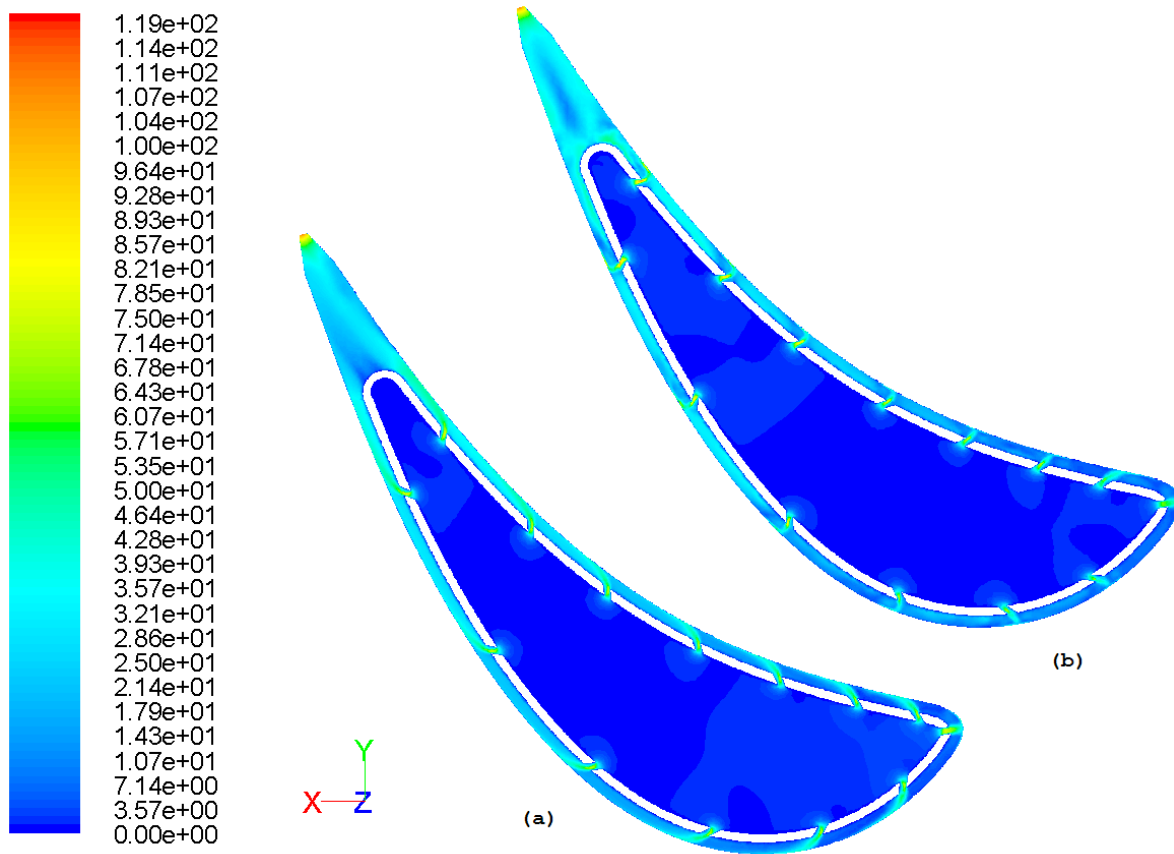
Figure 6-47: Velocity distribution [m/s] for (a) +45° and (b) -45°

Probing the effects of -45° inclination, using Figure 6-46, the stagnation Nu value seems to drop from the base model, however the magnitude of the drop is less compared to the +45° case. It is noteworthy to watch the Nu distribution being characterized by a secondary maximum, whose value increases as the flow moves downstream; this is signified by the arrow indicator in the figure. This secondary maximum may be associated with the increase in turbulence level and heavy mixing of flow. That is, the high momentum flow from the jets coupled with velocity fluctuations could be the cause of secondary peaks. This phenomenon may also be contributed by the boundary layers in this region being thin and highly turbulent as in the case of single

impingement jets with H/D < 5 [14]. The deviation in the location of stagnation for this case due to streamwise cross-flow is marginal compared to the +45° case. Velocity distribution in Figure 6-47 (b) shows the variation of velocity magnitude upstream of the jet, at the jet impingement and further downstream of the jet. This fluctuating velocity and heavy flow mixing with strong eddies are the cause for secondary peaks. This was also seen in the experimental results of Bouchez and Goldstein [65] where the interaction of adjacent jets, streamwise cross-flow build-up and confinement were held responsible for eddying of flow and boundary layer separation just before impingement. Also, such interactions resulted in the formation of secondary heat transfer peaks between jets. The averaged Nu values over the entire target surface showed 11.3% increase for the latter case and 8.9% dip compared to the base vane.

Although the -45° inclination's peak Nu values are reduced compared to the base vane, the appearance of secondary peaks improved the overall heat transfer values. As a result, the thermal stress on the airfoil surface is reduced and hence this will benefit the vane in terms of providing longer lifespan. +45° tilt of nozzle improved the streamwise cross-flow effect and thus the convective heat transfer, but reduced the effectiveness of impingement heat transfer.

Nusselt number is a measure of effectiveness of heat transfer. Upon plotting the effectiveness on the y-axis computed using equation (3.8) versus the C/D ratio in Figure 6-48 and comparing it to Figure 6-46, it is seen that the curves follow the same trend and that they are very similar except that the scale on the y-axis has changed. The Nu could be easily substituted due to the constant temperature boundary condition on the target surface instead of a heat flux. Since the Nu curve essentially shows the effectiveness of heat transfer, it was used throughout the thesis results. The magnitude of effectiveness in terms of percentage, however, can be seen in Figure 6-48.

The total pressure for the +45° tilt is dominated by the dynamic pressure and not the static pressure as seen from Figure 6-49, Figure 6-50 and Figure 6-51. This implies that the cooling is mainly due to the convective cooling of the cross-flow and not due to enhanced mixing. The effect of cross-flow is also apparent in the same figures. Compared to the baseline case the dynamic pressure at the jet exit increases and so does the total pressure. The total pressure for the -45° tilt increases way higher and is dominated by the static pressure as in Figure 6-52.
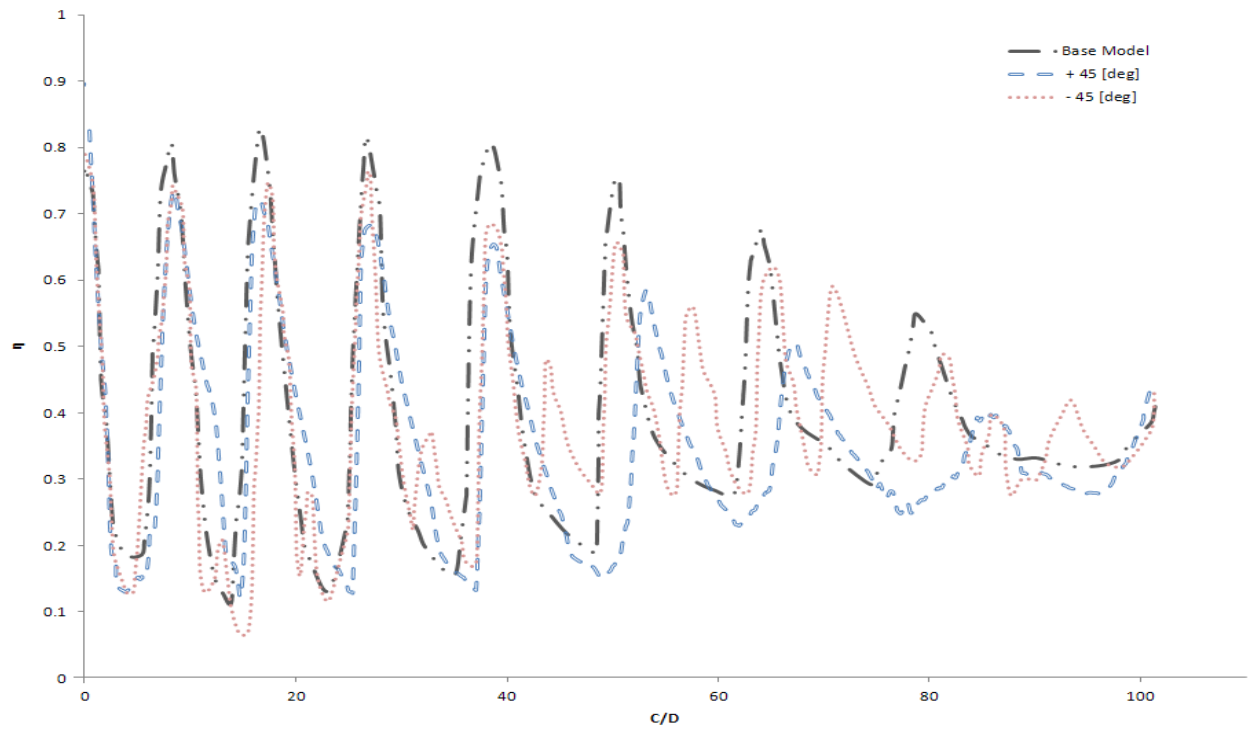
Figure 6-48: Adiabatic effectiveness of jets

Figure 6-49: Static pressure [Pa] (gauge) for +45° inclination (a) Target surface (b) Column 2
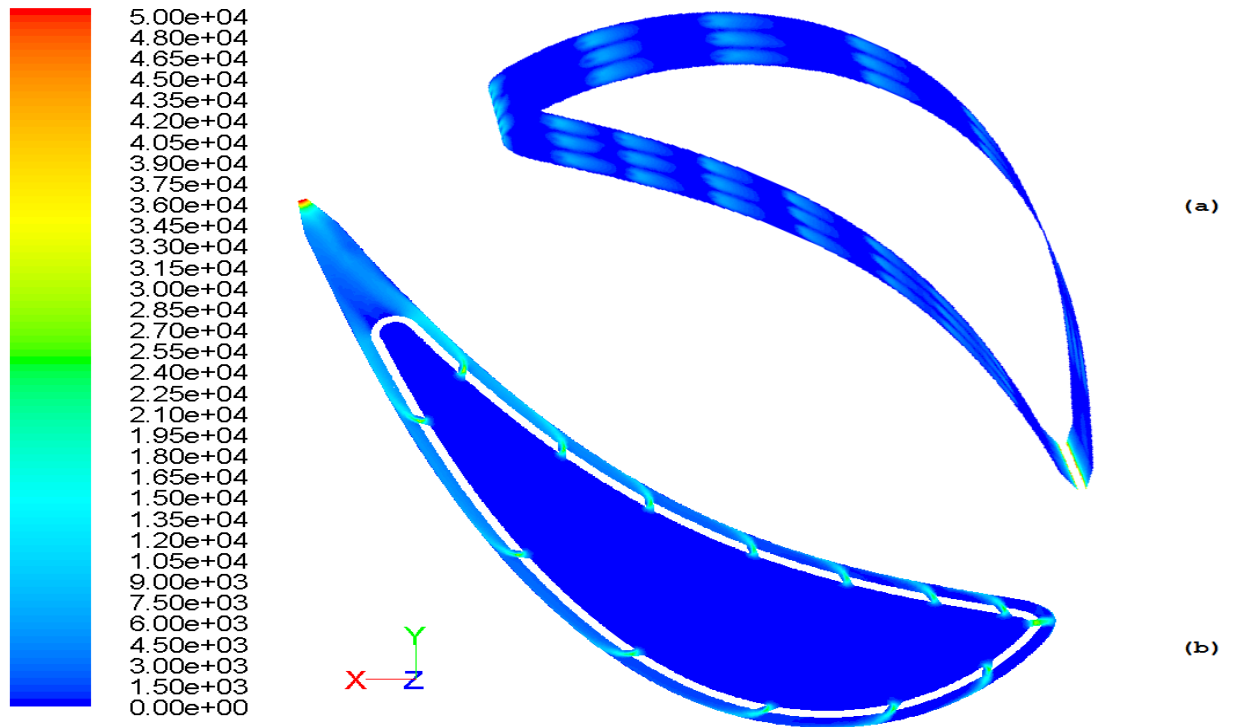
Figure 6-50: Dynamic pressure [Pa] (gauge) for +45° inclination
(a) Target surface (b) Column 2

Figure 6-51: Total pressure [Pa] (gauge) for +45° inclination (a) Target surface (b) Column 2
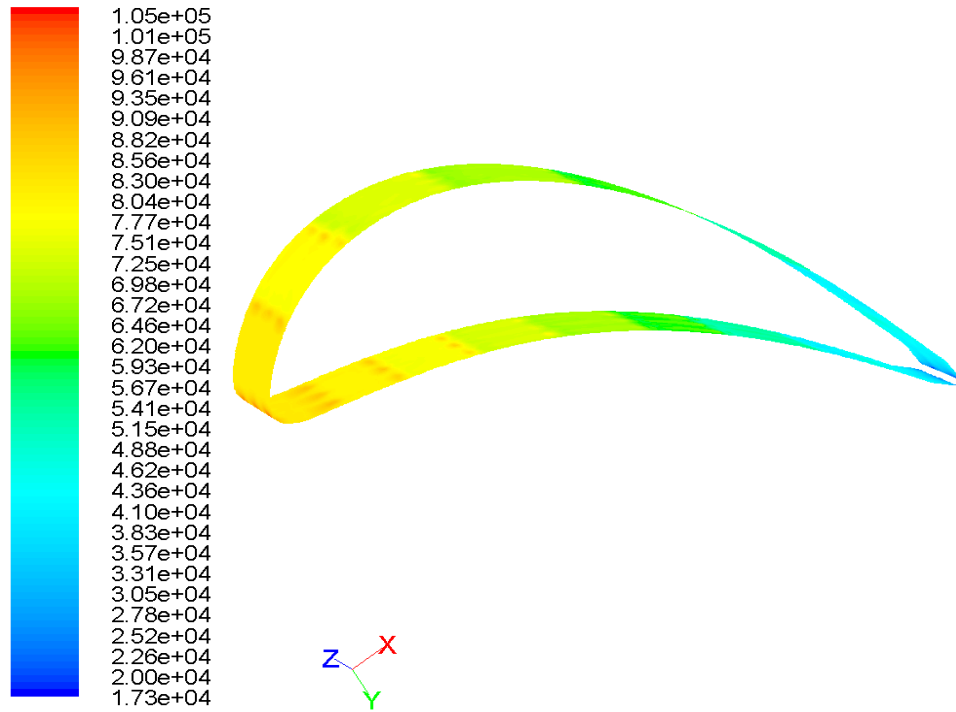
Figure 6-52: Total pressure [Pa] (gauge) for -45° inclination on target surface

From all the pressure contours above it is apparent that if the static pressure at the target increases, the overall heat transfer increases. Also, if the dynamic pressure increases, the static pressure reduces and the static pressure difference increases between the plenum and impingement chamber. Since the plenum pressure can be tweaked using the compressor bleed, it can be considered a constant. Thus, the static pressure in the impingement chamber decreases and this decrease causes the jet exit velocity to increase. If the dynamic head due to cross-flow increases the battle between the impinging jet and cross-flow build-up is dominated by the streamwise cross-flow build-up as seen in the +45° inclination of jets. If the dynamic head of the streamwise cross-flow is not allowed to build-up and prematurely disturbed, the static pressure at the target increases, however, the exit velocity at the jet decreases due to reduced demand for flow and hence the stagnation Nu for the -45° inclination is poor compared to the baseline case but dominant compared to the +45° tilt. The -45° inclination however, allows better mixing and transitions or resurrects the boundary layer allowing secondary heat transfer peaks and overall increase in Nusselt number. Hence, although the base model has improved stagnation heat transfer or high local heat transfer, the -45° jets perform better in terms of overall heat transfer. Also the coupling of dynamic and static pressures makes the heat transfer extremely complex.

98

6.2.4   *The Effect of Jet Diameter*

The analysis hereunder pertains to the application of micro jet impingement cooling for gas turbine vanes. Hence, to understand the effect of reducing the nozzle diameter to a micro scale of 0.25 mm, and 0.125 mm, the following assumption is made: this model is a simple reduction in jet diameter from the default values[19]. To wit, it is the resultant model where the turbine vane's plenum is assumed to be drilled with an aperture of 0.25 mm and 0.125 mm in lieu of 0.5 mm.

It is apparent from Figure 6-53 that when the diameter of the nozzle is reduced to micro scale, significant improvement in heat transfer coefficient is obtained. In fact, the improvement is about 1.5 times, as the diameter is reduced to half. Similar results have been comprehended by experimental results; for instance, about 20% to 70% increase was seen in stagnation values when the jet diameter was reduced from 1.5 mm to 1 mm in an experimental setup for single jet impingement by Glynn and Murray [25] as mentioned previously.
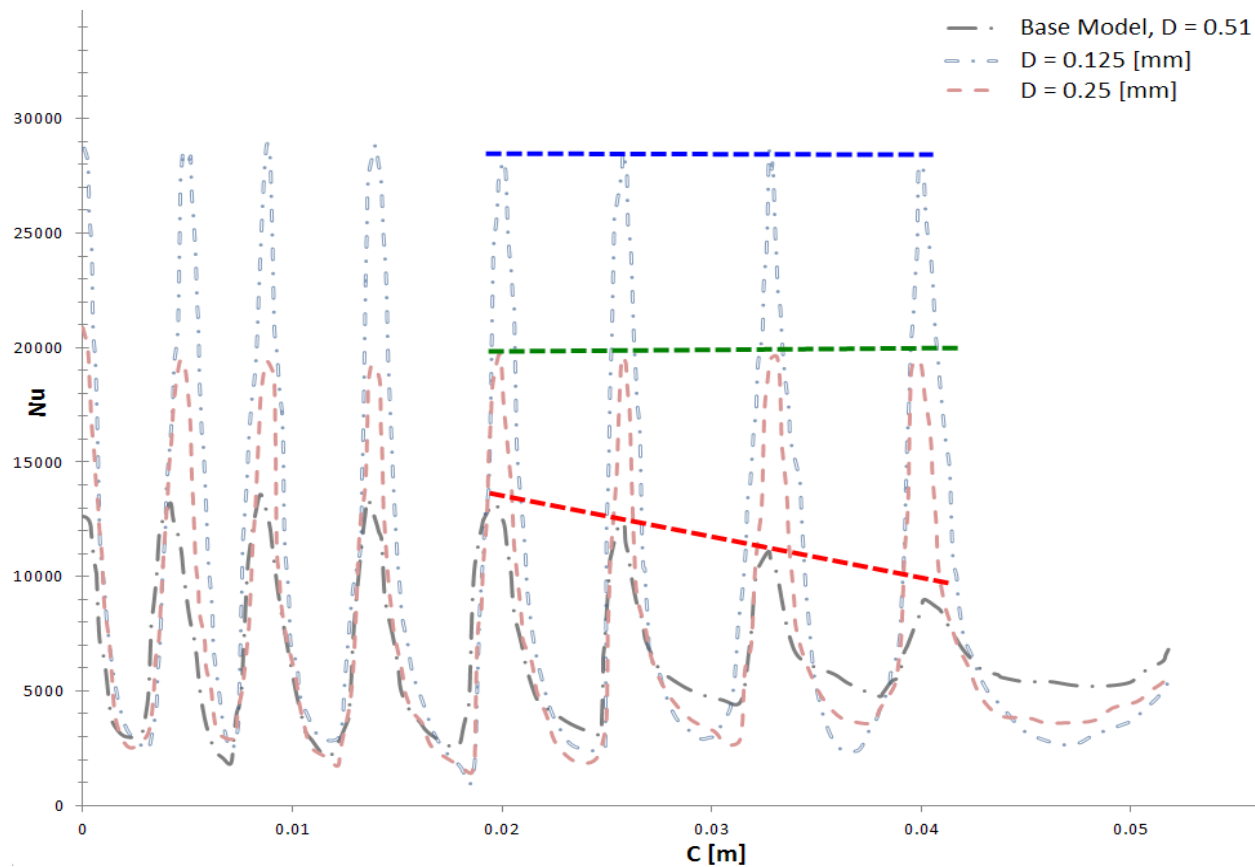
Figure 6-53: Effect of Jet Diameter

---

[19] The operating conditions allow the fluid to behave as a no slip continuum for D=0.25 mm as shown in Chapter 3.

A dimensional curved length was used on the abscissa since the non-dimensional form, C/D, relies on the diameter which varies across the models. Improvement on the heat transfer is seen for the same mass flow at the inlet of the plenum. The increased effectiveness of the jet impingement is increased compared to base model because of the reduced streamwise cross-flow effects. This is due to the reduced cooling flow (percent coolant mass) lessening the effect of cross-flow. Therefore, there are multiple benefits of micro-jets: they reduce the cross-flow by increasing the spanwise spacing and reducing the coolant mass; higher exit Re is seen due to the reduction in exit jet area and this increases the penetration of the jet; consequently, this yields a more uniform stagnation point heat transfer distribution on the airfoil surface. The effect of reduced cross-flow can be noticed by the relatively zero slope of the line joining the stagnation points for D = 0.25 and 0.125 mm shown in green and blue hashed lines as compared to 0.51 mm shown in red.

The downside however, apart from plugging as explained in Chapter 3.2, may be the high heat transfer gradient obtained; this may add to the thermal stress map and high thermal loading may shorten the lifespan of the vane [42]. Another shortcoming to reducing the diameter is the demand for higher pressure head. The impingement holes in the vane's plenum can be perceived as an orifice plate. When fluid reaches the orifice, it is forced to converge to go through the small hole. The point of maximum convergence actually occurs downstream of the physical orifice as explained in Chapter 3.2. As a result, the static pressure increases as the diameter decreases. The static pressure contours is provided in Figure 6-54. To meet this requirement, the flow area in the flow passage decreases, thereby increasing blockage as diameter is reduced; and, if the blockage increases, the losses will escalate implying the flow would not pass through the hole. Thus, there is an optimum point to the reduction in jet diameter.

The static pressure on the target surface increases for the reduced diameter case (0.25 mm diameter shown in Figure 6-54 (a)) compared to the baseline case Figure 6-44 (a). Similar increase is also seen for the 0.125 mm case and has not been included below. The total pressure, being dominated by the static pressure, also increases as seen in Figure 6-55. This is the cause of the tremendous increase in heat transfer. From Figure 6-54 (b), near the trailing edge (jet 7 on pressure surface), some indication of blockage is seen where the static pressure approaches zero.
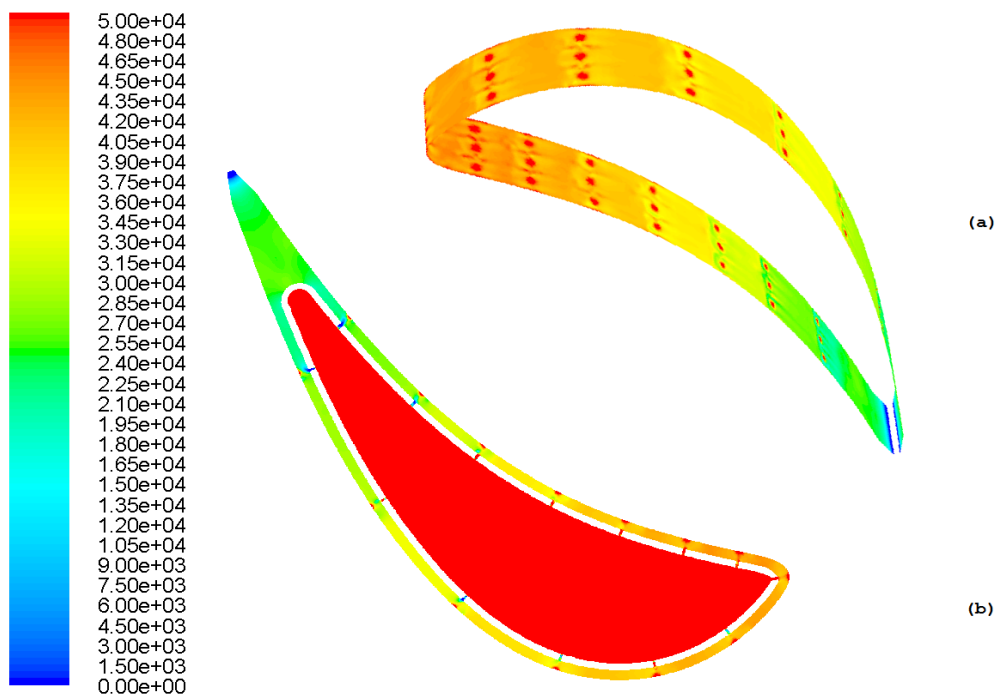
**Figure 6-54: Static pressure [Pa] (gauge) for 0.25 mm diameter
(a) Target surface (b) Column 2**
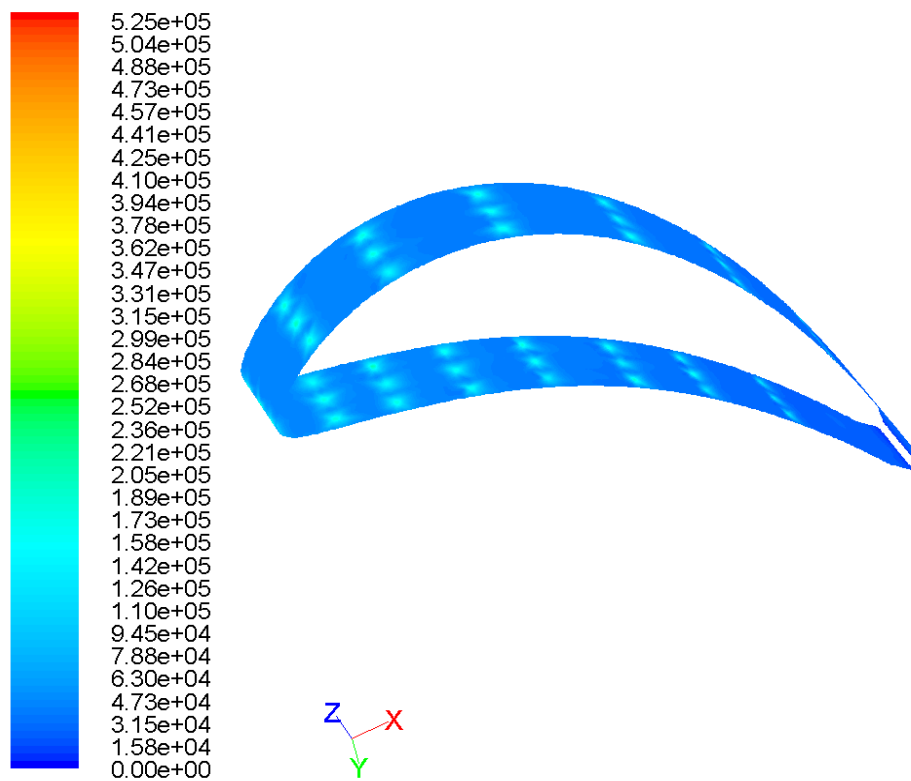
Figure 6-55: Total pressure on target surface for 0.25 mm diameter

101

The average Nu however for 0.125 mm surged to about 55% higher than 0.51 mm. The Re almost doubled at jet exit; that is, reducing the diameter of the nozzle by half, doubles the average Re across the array. This effectively increases the heat transfer obtained. Results for effect of change in Re are known as shown in single jet impingement case. The streamwise distribution of Re however remains the same.

Since the exit condition of the vane is extremely important as it determines the performance parameters of the engine, exit condition at the trailing edge of the vane, i.e. the average temperature for the cases considered herein is shown in the bar graph below. Figure 6-56 shows the inlet fluid temperature at 500 K. The target airfoil surface was at 300 K. Thus, the air after heat transfer shall get cooler; and, higher the overall heat transfer, cooler will be the temperature at the exit. In case of the real turbine vane without such boundary condition simplification, the plot would be the inverse of the one shown as the coolant would be heated up. It can be observed that decreasing the diameter increases heat transfer and for the real vane, increases the outlet temperature. Thus, the smaller diameter jets would reduce losses usually experienced at the trailing edge of the vane when the flow is injected back into the mainstream gas path. This is due to the reduced variation in temperature between the mainstream flow and coolant flow [42].
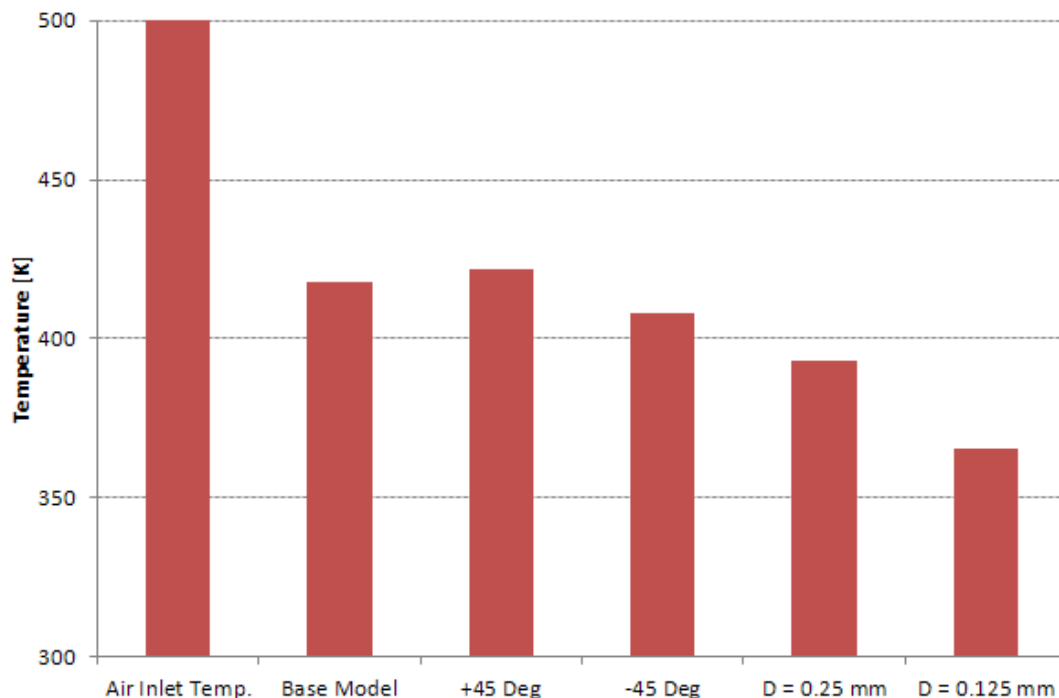
Figure 6-56: Temperature [K] of the fluid at vane exit (Trailing edge)

CHAPTER SEVEN

CONCLUSIONS AND RECOMMENDATIONS FOR FUTURE WORK

Several conclusions were drawn throughout the study and they are reviewed below starting with the single jet impingement case.

The local heat transfer characteristics for a single, axisymmetric jet impingement cooling model was successfully modeled for application towards cooling of a high pressure turbine vane. The model was built and meshed in Gambit, whereas the pre-processing, solving and post processing was performed in Fluent. Mesh sensitivity analysis was performed for selecting the turbulence model. Low-Re-k-ε Lam Bremhorst turbulence model outperformed the standard turbulence models when compared to experimental results. The effects of Reynolds number, H/D effect and geometric changes, that is, the change of nozzle diameter and the change in nozzle shape were considered for the parametric analysis. The tested Reynolds number were Re = 2000, 4000 and 6000. It was concluded that as the Reynolds number increased, so did the heat transfer rates. This phenomenon was confirmed by the corresponding velocity contours. In general, a monotonic decrease in Nusselt number was found from its peak. The maximum Nu value did not occur at the stagnation point but at a non-dimensional radial distance of 0.5. In addition, for the H/D ratios (H/D = 1, 3 and 6), it was seen that the local Nu did not vary much with changing H/D ratios downstream in the radial direction. Predicted trends for other H/D ratios shows a discontinuity when H/D < 1. It was seen that the trend improves for smaller H/D ratios. A typical saddle shape was also seen around the stagnation region for lower H/D ratios. In terms of reducing the hole diameter to 0.25 mm, it was seen that micro-impingement performed better than macro scale for the same mass flow per unit heated area. Also, for the elliptical nozzle with the same hydraulic diameter, a 20.8% increase in average Nusselt number values was obtained. In terms of the pressure distribution, the dynamic head converting to static pressure rise was seen as the stagnation zone where impingement heat transfer was high. Thus, this study formed the base for exploration of micro scale impingement cooling inside a turbine vane.

Three-dimensional actual shaped turbine vane geometry of the NASA GE Energy Efficient Engine was numerically studied for the effects of change in diameter and inclination of 42 micro jets. The diameters investigated include 0.51 mm, 0.25 mm and 0.125 mm. The inclinations altered were +45° and -45°. For simplicity, validation and better understanding the nature of impingement heat transfer, the airfoil surfaces were provided with a constant temperature boundary condition. Moreover, it was assumed that the flow in its entirety exits from the trailing edge and no leakages occur (especially at inter-stage seal). Validation was performed against existing numerical results on a simplified model with no spanwise tapering or twisting.

Results for airfoil with tapering and twisting yielded better heat transfer results as the flow moved in the tapered span direction when compared to the validation vane. Cross-flow build-up was seen to impede the effective impingement heat transfer distribution. The effects however were not prominent for the first few jet rows, where it was witnessed that if the average exit velocity was greater than the spent air velocity, the heat transfer distribution was improved or remained almost the same.

The results obtained for reduction in nozzle diameter indicated that the Reynolds number at the jet exit almost doubles and improves the heat transfer substantially. Another added benefit to reduced diameter is the lessened cross-flow effect. Uniform heat transfer distribution is thus observed for both cases considered: 0.25 and 0.125 mm jet diameter, that is, the cross-flow is at a minimum. On the other hand the small diameter leads to higher effective thermal stresses and may be prone to plugging.

The effects of changing the inclination of nozzles were also studied. Two cases were considered, one where the inclination of the nozzle supported the streamwise cross-flow and the other opposed it. Although both cases did not produce improvement in terms of stagnation values compared to the base model, the inclination of -45° yielded secondary peaks and an overall improvement in the averaged Nu value. +45° tilt of nozzle improved the streamwise cross-flow effect and thus the convective heat transfer, but reduced the effectiveness of impingement heat transfer. The deviation in the position of stagnation Nu number increased in the stream wise direction

The shortcomings, however, for the reduced diameter case included plugging or blockage and high heat transfer gradients. This heat transfer gradient adds to the thermal stress map and it was known that high thermal loading shortens the lifespan of the vane [42]. Another limitation to reducing the diameter was the demand for higher pressure head and higher losses. This results in a static pressure rise as the diameter decreases. To meet this requirement, the flow area in the flow passage decreases, thereby increasing blockage; and, if the blockage increases, the losses further escalate implying the flow would not pass through the hole.

Overall, the study was a success where the advantages and disadvantages for the various cases considered above were discussed. The potential for micro jets in alleviating heat transfer effectiveness was considered beneficial for application inside a turbine vane. The following future work is recommended for further exploration in the same area of research:

It was seen that the cross-flow build-up and the impinging jet were coupled and in constant battle. That is, a higher cross-flow reduces the local pressure and demands for increased Reynolds number at the jet exit, thus allowing better heat transfer due to impingement. Also, for low cross-flow build up an increase in heat transfer was observed. Hence, there should be an optimum point to achieve maximum heat transfer for the coupling explained above.

One of the shortcomings of reduction in jet diameter is the increase in blockage due to reduced flow area. Therefore there is an optimum jet diameter where the static pressure rise is such that the blockage is at a minimum and the heat transfer is at a maximum.

Design of experiment/optimization of the nozzle shape should be performed for exploring the design space of micro jet impingement and hence, larger data should be gathered for understanding geometric effects on heat transfer.

Since small diameter jets leads to higher effective thermal stresses, uniform cooling where reduced thermal stresses are seen can be employed by increasing the number of jets. However, the cross-flow effect will increase and so will the interaction of jets. The problem of reducing thermal stress while minimizing cross-flow effect needs to be explored.

Finally, the model should be expanded to include one dimensional heat balance starting from the outer surface with real heat flux and conditions as used in reference [42].

REFERENCES

[1] Je-Chin Han, Sandip Dutta, and Srinath V. Ekkad, *Gas Turbine Heat Transfer And Cooling Technology*. New York, USA: Taylor & Francis, 2000.

[2] S. Farokhi, *Aircraft Propulsion*.: John Wiley & Sons, Inc., 2009.

[3] B. L. Koff, "Spanning the Globe with Jet Propulsion," *AIAA*, pp. 1-17, 1991.

[4] B. Lakshminarayana, *Fluid Dynamics and Heat Transfer of Turbomachinery*.: John Wiley & Sons, Inc., 1996.

[5] Meherwan P. Boyce, *Gas Turbine Engineering Handbook*, 3rd ed.: Gulf Professional Publishing, 2006.

[6] E. E. Halila, D. T. Lenahan, and T. T. Thomas, "Energy Efficient Engine: High Pressure Turbine Test Hardware Detailed Design Report," 1982.

[7] M. Suo, "Turbine Cooling," in *Aerothermodynamics of Aircraft Engine Components*.: American Institute of Aeronautics and Astronautics, 1985, ch. 5, pp. 275-330.

[8] I. G. Currie, *Fundamental Mechanics of Fluids*, 3rd ed. New York: Marcel Dekker, Inc., 2003.

[9] Giacoma Flora and Muhammad Usman. (2010) The MathWorks, Inc. [Online]. http://www.mathworks.com/matlabcentral/fileexchange/28042-a-graphical-user-interface-for-solving-the-falkner-skan-equation

[10] E. Kaufman and E. Gutierrez-Miravete, "An Analysis of Hiemenz Flow," in *COMSOL Conference*, Boston, 2008.

[11] Frank M. White, *Viscous Fluid Flow*, 2nd ed. Toronto: McGraw-Hill, Inc., 1991.

[12] Ferruh Erdogdu, Maria Ferruh, Samrendra K. Singh, and Paul R. Singh, "Air-impingement cooling of boiled eggs: Analysis of flow visualization and heat transfer ," *Journal of Food Engineering*, vol. 79, no. 3, pp. 920-928, April 2007.

[13] Marcel Leon De Paz and B. A. Jubran, "Predictions of Thermal and Hydrodynamic Characteristics of a Single Circular Micro-Jet Impinging on a Flat Plate," in *Proceedings of ASME Turbo Expo 2008: Power for Land, Sea and Air*, vol. GT2008-50490, Berlin, 2008, pp. 1-10.

[14] Frank P. Incropera, David P. DeWitt, Theodore L. Bergman, and Adrienne S. Lavine, *Fundamentals of heat and mass transfer*, 6th ed.: John Wiley & Sons, Inc., 2007.

[15] Peter Hrycak, "Heat Transfer From Imping Jets - A Literature Review," Flight Dynamcis Laboratory (AFWAL/FIEE), New Jersey Institute of Technology, Final Report Report Number: AFWAL-TR-81-3054, 1981.

[16] James W. Gauntner, John N. B. Livingood, and Peter Hrycak, "Survey of Literature on Flow Characteristics of a Single Turbulent Jet Impinging on a Flat Plate," Lewis Research Center, Cleveland, Technical Note Report Number: NASA TN D-5652, 1970.

[17] R. N. Koopman and E. M. Sparrow, "Local and Average Transfer Coefficients due to an Impinging Row of Jets," , vol. 19, 1976, pp. 673-683.

[18] L. W. Florschuetz, R. A. Berry, and D. E. Metzger, "Periodic Streamwise Variations of Heat

Transfer Coefficients for Inline and Staggered Arrays of Circular Jets with Crossflow of Spent Air," , vol. 102, 1980, pp. 132-137.

[19] T. K. Van, Z. Wang, P. Ireland, I. Jones, and S. Kohler, "Comparison and Prediction of Local and Average Heat Transfer Coefficients under an Array of Inline and Staggered Impinging Jets," , Birmingham, 1996.

[20] T. Van, "Impingement Flow Heat Transfer Measurements of Turbine Blades Using a Jet Array," University of Oxford, PhD Thesis 1994.

[21] D. Kercher and W. Tabakoff, "Heat transfer by a square array of round air jets impinging perpendicular to a flat surface including the effect of spent air," vol. 92, pp. 73-82, 1970.

[22] H. Martin, "Heat and mass transfer between impinging gas," *Adv. in heat transfer*, vol. 13, pp. 1-60, 1977.

[23] Y. Huang, S. V. Ekkad, and J. C. Han, "Detailed Heat Transfer Coefficient Distributions Under an Array of Inclined impinging Jets Using a Transient liquid Crystal Technique," , Singapore, 1996.

[24] J. Lee and S.J. Lee, "Stagnation Region Heat Transfer of a Turbulent Axisymmetric Jet Impingement," *Expt. Heat Transfer*, vol. 12, no. 2, pp. 137-156, 1998.

[25] C. Glynn and D.B. Murray, "Jet Impingement Cooling in Microscale," *ECI Int. Conf. on Heat Transfer & Fluid Flow in Microscale*, pp. 1-7, 2005.

[26] M. Leon De Paz, "A Numerical Study of Impinging Jets Inside a Turbine Vane," Department of Aerospace Engineering, Ryerson University, Toronto, MAScThesis 2009.

[27] Nicolas G. Hadjiconstantinou and Olga Simek, "Constant-Wall-Temperature Nusselt Number in Micro and Nano-Channels," *ASME*, vol. 124, pp. 356-364, April 2002.

[28] Anil W. Date, *Introduction to Computational Fluid Dynamics*.: Cambridge University Press, 2005.

[29] Frank M. White, *Fluid Mechanics*, 5th ed. Toronto: McGraw-Hill, 2003.

[30] Y. Yan and R. B. Thorpe, "Flow Regime Transitions due to Cavitation in the Flow Through an Orifice," *International Journal of Multiphase Flow*, vol. 16, no. 6, pp. 1023-1045, 1990.

[31] Thomas J. Grindle and Frank W., Jr. Burcham, "Engine Damage to a NASA DC-8-72 Airplane From a High-Altitude Encounter With a Diffuse Volcanic Ash Cloud," Technical Memorandum 2003.

[32] W. H. Cubberly and Ramon Bakerjian, *Desk Edition: Tool and manufacturing engineers handbook*.: Society of Manufacturing Engineers (SME), 1989, ch. 29, pp. 11-18.

[33] Kenneth B. Hall, "Dirt Removal Means for Air Cooled Blades," 4,820,123, Apr. 11, 1989.

[34] Camron C Land, Karen A. Thole, and Chris Joe, "Consideration of a Double-wall Cooling Design to Reduce Sand Blockage," , Berlin, 2008.

[35] A. F. Mills, *Heat Transfer*, 2nd ed. New Jersey: Prentice-Hall, Inc., 1999.

[36] K. Jambunathan, E. Lai, M. A. Moss, and B. L. Button, "A review of heat transfer data for single circular jet impingement," *J. Heat and Fluid Flow*, vol. 13, no. 2, pp. 106-115, June 1992.

[37] R. Gardon and J. Akfirat, "The role of turbulence in determining the heat-transfer

characteristics of impinging jets," *Int. J. f Heat Mass Transfer*, vol. 8, pp. 1261-1272, 1965.

[38] N. T. Obot, A. S. Majumdar, and W. J. M. Douglas, "The effect of nozzle geometry on impingement heat transfer under a round turbulent jet," *American Society of Mechanical Engineers (ASME)*, pp. 1-12, December 1979.

[39] D. Lytle and B.W. Webb, "Air Jet Impingement Heat Transfer at Low Nozzle-Plate Spacings," *Int. J. Heat Mass Transfer*, vol. 37, pp. 1687-1697, 1994.

[40] H. Hofmann, M. Kind, and H. Martin, "Measurements on steady state heat transfer and flow structure and new correlations for heat and mass transfer in submerged impinging jets," *Int. J. of Heat and Mass Transfer*, vol. 50, pp. 3957–3965, 2007.

[41] Fluent Inc., GAMBIT 2.2 Tutorial Guide, September 2004.

[42] L. P. Timko, "Energy Efficient Engine: High Pressure Turbine Component Test Performance Report,".

[43] M. Behnia, S. Parneix, Y. Shabany, and P. A. Durbin, "Numerical study of turbulent heat transfer in confined and unconfined impinging jets," *Int. J of Heat and Fluid Flow*, vol. 20, no. 1, pp. 1-9, 1999.

[44] M. Angioletti, E. Nino, and G. Ruocco, "CFD turbulent modelling of jet impingement and its validation by particle image velocimetry and mass transfer measurements," *International Journal of Thermal Sciences*, vol. 44, no. 4, pp. 349-356, November 2004.

[45] M. Coussirat and V.J. Beeck et al, "Computational fluids dynamics modeling of impinging gas-jet systems:2. Application to an Industrial Cooling System Device," *J.l of fluids engineering*, vol. 127, pp. 691-703, 2005.

[46] H. K. Versteeg and W. Malalasekera, *An introduction to computational fluid dynamics: the finite volume method*. Toronto: Pearson-Prentice Hall, 1995.

[47] S. Ashforth-Frost and K. Jambunathan, "Numerical Prediction of Semi-Confined Jet Impingement and Comparison with Experimental Data," *Int. J. Numer. Meth. Fluids*, vol. 23, pp. 295-306, 1996.

[48] M.K. Isman and E. Pulat et al., "Numerical Investigation of Turbulent Impinging Jet Cooling of a Constant Heat Flux Surface," *Numer. Heat Transfer, Part A: Applications*, vol. 53, no. 10, pp. 1109-1132, 2008.

[49] J.T Craft, W.L.J. Graham, and E.B. Launder, "Impinging Jet Studies for Turbulence Model Assessment—II. An Examination of the Performance of Four Turbulence Models," *Int. J. Heat Mass Transfer*, vol. 36, pp. 2685-2697, 1993.

[50] J.S. Wang and S.A. Mujumdar, "A Comparative Study of Five Low Reynolds Number k-e Models for Impingement Heat Transfer," *Appl. Therm. Eng.*, vol. 25, pp. 31-44, 2005.

[51] S.Z. Shuja, B.S. Yilbas, and M.O. Budair, "Gas Jet Impingement on a Surface Having a Limited Constant Heat Flux Area: Various Turbulence Models," *Numer. Heat Transfer*, vol. 36, pp. 171–200, 1999.

[52] A. Abdon and B. Sunden, "Numerical Investigation of Impingement Heat Transfer Using Linear and Non-linear Two-Equation Turbulence Models," *Numer. Heat Transfer*, vol. 40, pp. 563-578, 2001.

[53] Y. Tzeng, Y. Soong, and D. Hsieh, "Numerical Investigation of Heat Transfer Under

Confined Impinging Turbulent Slot Jets," *Numer. Heat Transfer: Part A*, vol. 35, pp. 903-924, 1999.

[54] N. Zuckerman and N. Lior, "Impingement Heat Transfer: Correlations and Numerical Modeling," *ASME J. Heat Transfer*, vol. 127, pp. 544-552, 2005.

[55] FLUENT INC. , FLUENT 6.3 User's Guide, 2006.

[56] Ansys Inc. , ICEM CFD Release Notes for 11.0 SP1 User Guide, 2007.

[57] J. Cadafalch, C. D. Perez-Segarra, R. Consul, and A. Oliva, "Verification of Finite Volume Computations on Steady-State Fluid Flow and Heat Transfer," vol. 124, no. 11, 2002.

[58] P. Roache, "Perspective: A Method for Uniform Reporting of Grid Refinement Studies," *Journal of Fluids Engineering*, vol. 116, pp. 405-413, 1994.

[59] Lianmin Huang and Mohamed S. El-Genk, "Heat transfer of an impinging jet on a flat surface," *Int. J of Heat and Mass Transfer*, vol. 37, pp. 1915-1923, 1994.

[60] Janice Fitzgerald and Suresh Garimella, "A study of the flow field of a confined and submerged impinging jet," *Int. J. heat and mass transfer*, vol. 41, pp. 1025-1034, 1998.

[61] Bertrand P.E. Dano, James A. Liburdy, and Koonlaya Kanokjaruvijit, "Flow characteristics and heat transfer performances of a semi-confined impinging array of jets: effect of nozzle geometry," *International Journal of Heat and Mass Transfer*, vol. 48, pp. 691-701, 2005.

[62] Andrew C. Chambers, David R. H Gillespie, Peter T. Ireland, and Mark Mitchell, "Enhancement of impingement cooling in a high cross flow channel using shaped impingement cooling holes," in *ASME Turbo Expo*, vol. 3 Part B, 2006, pp. 995-1004.

[63] Lujia Gao, "Effect of Jet Hole Arrays Arrangement on Impingement Heat Transfer," Louisiana State University, MASc Thesis 2003.

[64] T. Wang, M. Lin, and R. S. Bunker, "Flow and Heat Transfer of Confined Impingement Jets Cooling using a 3-D Transient Liquid Crystal Scheme," *International J. Heat and Mass Transfer*, vol. 48, pp. 4887-4903, 2005.

[65] J. -P. Bouchez and R. J. Goldstein, "Impingement Cooling from a Circular Jet in a Cross Flow," *International J. Heat and Mass Transfer*, vol. 18, no. 6, pp. 719-730, 1975.

[66] George Emanuel, *Analytical Fluid Dynamics*, 2nd ed.: CRC Press, 2001.

APPENDIX A - DERIVATIONS

Exact solution to 2-D, inviscid stagnation point flow starting with governing equations

The general form of 3-D continuity equation with no source terms is given as:

$$\frac{\partial \rho}{\partial t} + \frac{\partial \rho u}{\partial x} + \frac{\partial \rho v}{\partial y} + \frac{\partial \rho w}{\partial z} = 0 \tag{I}$$

and the N-S equation in Cartesian coordinate system is represented as below:

$$\left. \begin{array}{l} \dfrac{\partial \rho u}{\partial t} + u\dfrac{\partial \rho u}{\partial x} + v\dfrac{\partial \rho u}{\partial y} + w\dfrac{\partial \rho u}{\partial z} = -\dfrac{\partial p}{\partial x} + \mu\left[\dfrac{\partial^2 u}{\partial x^2} + \dfrac{\partial^2 u}{\partial y^2} + \dfrac{\partial^2 u}{\partial z^2}\right] + \rho g_x \\[3mm] \dfrac{\partial \rho v}{\partial t} + u\dfrac{\partial \rho v}{\partial x} + v\dfrac{\partial \rho v}{\partial y} + w\dfrac{\partial \rho v}{\partial z} = -\dfrac{\partial p}{\partial y} + \mu\left[\dfrac{\partial^2 v}{\partial x^2} + \dfrac{\partial^2 v}{\partial y^2} + \dfrac{\partial^2 v}{\partial z^2}\right] + \rho g_y \\[3mm] \dfrac{\partial \rho w}{\partial t} + u\dfrac{\partial \rho w}{\partial x} + v\dfrac{\partial \rho w}{\partial y} + w\dfrac{\partial \rho w}{\partial z} = -\dfrac{\partial p}{\partial z} + \mu\left[\dfrac{\partial^2 w}{\partial x^2} + \dfrac{\partial^2 w}{\partial y^2} + \dfrac{\partial^2 w}{\partial z^2}\right] + \rho g_z \end{array} \right\} \tag{II}$$

Reducing the continuity and N-S equation respectively to inviscid, incompressible, steady state, two-dimensional form with no body force we get:

$$\frac{\partial u}{\partial x} + \frac{\partial v}{\partial y} = 0 \tag{1}$$

$$\left. \begin{array}{l} u\dfrac{\partial u}{\partial x} + v\dfrac{\partial u}{\partial y} = -\dfrac{1}{\rho}\dfrac{\partial p}{\partial x} \\[3mm] u\dfrac{\partial v}{\partial x} + v\dfrac{\partial v}{\partial y} = -\dfrac{1}{\rho}\dfrac{\partial p}{\partial y} \end{array} \right\} \tag{2}$$

Transforming above equations to stream-function formulation by introducing the following:

$$u \equiv \frac{\partial \psi}{\partial y} \qquad v \equiv -\frac{\partial \psi}{\partial x} \tag{3}$$

Substituting in the continuity equation we get

$$\frac{\partial}{\partial x}\left(\frac{\partial \psi}{\partial y}\right) + \frac{\partial}{\partial y}\left(-\frac{\partial \psi}{\partial x}\right) = 0$$

$$\frac{\partial^2 \psi}{\partial x \partial y} = \frac{\partial^2 \psi}{\partial x \partial y} \tag{4}$$

Hence, continuity equation is unconditionally satisfied.

To transform N-S equation, differentiating x direction momentum equation w.r.t y we get

$$\frac{\partial}{\partial y}\left(u\frac{\partial u}{\partial x}\right)+\frac{\partial}{\partial y}\left(v\frac{\partial u}{\partial y}\right)=\frac{\partial}{\partial y}\left(-\frac{1}{\rho}\frac{\partial p}{\partial x}\right)$$

Or

$$\frac{\partial u}{\partial y}\frac{\partial u}{\partial x}+u\frac{\partial^2 u}{\partial x\partial y}+\frac{\partial v}{\partial y}\frac{\partial u}{\partial y}+v\frac{\partial^2 u}{\partial y^2}=-\frac{1}{\rho}\frac{\partial^2 p}{\partial y\partial x} \tag{a}$$

Similarly differentiating y direction N-S equation w.r.t x we get

$$\frac{\partial u}{\partial x}\frac{\partial v}{\partial x}+u\frac{\partial^2 v}{\partial x^2}+\frac{\partial v}{\partial x}\frac{\partial v}{\partial y}+v\frac{\partial^2 v}{\partial x\partial y}=-\frac{1}{\rho}\frac{\partial^2 p}{\partial y\partial x} \tag{b}$$

Subtracting equations (a) and (b) we get,

$$\frac{\partial u}{\partial y}\frac{\partial u}{\partial x}-\frac{\partial u}{\partial x}\frac{\partial v}{\partial x}+u\frac{\partial^2 u}{\partial x\partial y}-u\frac{\partial^2 v}{\partial x^2}+\frac{\partial v}{\partial y}\frac{\partial u}{\partial y}-\frac{\partial v}{\partial x}\frac{\partial v}{\partial y}+v\frac{\partial^2 u}{\partial y^2}-v\frac{\partial^2 v}{\partial x\partial y}=0$$

Rearranging the equation as:

$$\frac{\partial u}{\partial x}\left(\frac{\partial u}{\partial y}-\frac{\partial v}{\partial x}\right)+u\frac{\partial}{\partial x}\left(\frac{\partial u}{\partial y}-\frac{\partial v}{\partial x}\right)+\frac{\partial v}{\partial y}\left(\frac{\partial u}{\partial y}-\frac{\partial v}{\partial x}\right)+v\frac{\partial}{\partial y}\left(\frac{\partial u}{\partial y}-\frac{\partial v}{\partial x}\right)=0 \tag{c}$$

Introducing vorticity to the above equation for simplification, we have by definition of vorticity:

$$\xi=\frac{\partial v}{\partial x}-\frac{\partial u}{\partial y} \tag{5}$$

Substituting equation (5) into equation (c) above we get,

$$\frac{\partial u}{\partial x}(-\xi)+u\frac{\partial}{\partial x}(-\xi)+\frac{\partial v}{\partial y}(-\xi)+v\frac{\partial}{\partial y}(-\xi)=0$$

$$\xi\left(\frac{\partial u}{\partial x}+\frac{\partial v}{\partial y}\right)+u\frac{\partial \xi}{\partial x}+v\frac{\partial \xi}{\partial y}=0$$

Using equation (1) in the above equation, the equation reduces to:

$$u\frac{\partial \xi}{\partial x}+v\frac{\partial \xi}{\partial y}=0 \tag{6}$$

Substituting equation (3) into equation (5) we get:

$$\xi=-\frac{\partial}{\partial x}\frac{\partial \psi}{\partial x}-\frac{\partial}{\partial y}\frac{\partial \psi}{\partial y}$$

$$-\xi=\frac{\partial^2 \psi}{\partial x^2}+\frac{\partial^2 \psi}{\partial y^2} \tag{d}$$

Substituting equation (d) into (6) and making use of equation (3) we get,

$$\frac{\partial \psi}{\partial y}\left[\frac{\partial}{\partial x}\left(-\frac{\partial}{\partial x}\frac{\partial \psi}{\partial x}-\frac{\partial}{\partial y}\frac{\partial \psi}{\partial y}\right)\right]-\frac{\partial \psi}{\partial x}\left[\frac{\partial}{\partial y}\left(-\frac{\partial}{\partial x}\frac{\partial \psi}{\partial x}-\frac{\partial}{\partial y}\frac{\partial \psi}{\partial y}\right)\right]=0$$

Or,

$$\left(\frac{\partial\psi}{\partial y}\frac{\partial}{\partial x} - \frac{\partial\psi}{\partial x}\frac{\partial}{\partial y}\right)\left[\frac{\partial^2\psi}{\partial x^2} + \frac{\partial^2\psi}{\partial y^2}\right] = 0 \tag{7}$$

For inviscid flow, at the boundary, a streamline is present and velocity is not zero (or from potential flow theory) the first term cannot be zero, hence from the above equation we have:

$$\frac{\partial^2\psi}{\partial x^2} + \frac{\partial^2\psi}{\partial y^2} = 0 \tag{8}$$

The functional form of the stream function for total change in ψ is obtained from the following equation:

$$d\psi = \frac{\partial\psi}{\partial x}dx + \frac{\partial\psi}{\partial y}dy = -vdx + udy \tag{9}$$

Which, for constant ψ is:

$$\frac{dy}{dx} = \frac{v}{u} \tag{10}$$

The velocity potential (ϕ) is also obtained in a similar manner. Let the complex potential F(z) be defined as [8]:

$$F(z) = \phi(x,y) + i\psi(x,y) \tag{11}$$

Where,

$$z = x + iy \tag{12}$$

Taking derivative of equation (11) and using equation (3) and (12) we get the complex velocity:

$$W(z) = \frac{dF}{dz} = u - iv \tag{13}$$

The analytic solution for flow around a cylinder is given by [66]:

$$\psi = U_\infty \frac{y^2 + 2yR}{y + R}\sin\frac{x}{R} \tag{14}$$

Where, R is the radius of the cylinder. x is along the circumference of the cylinder. y is the distance measured perpendicular to x (normal to the circumference of the cylinder). The origin is at the stagnation point.

For stagnation point flow (near the vicinity of stagnation point), expanding the above equation using Taylor series to the first order at point y = 0 (stagnation point) for large values of R (such

that the target surface seen by the impinging flow is flat on the cylinder), and using small angle approximation, this equation reduces to:

$$\psi \approx \frac{U_\infty}{R} 2xy \tag{15}$$

Here, U_∞ is the free stream velocity and R is the reference length. Using the reference length as unity for simplification, we get:

$$\psi = 2U_\infty xy \tag{16}$$

This may also be arrived by using the complex potential (see equation (11) and (12) for reference) F(z) as follows:

$$\left. \begin{aligned} F(z) &= U_\infty z^2 \\ &= U_\infty (x + iy)^2 \\ &= U_\infty (x^2 - y^2) + i2U_\infty xy \end{aligned} \right\} \tag{17}$$

Or, equation (16) is satisfied from the imaginary part of the above equation. The real part of the equation is the velocity potential. Also, using equation (3) and (16) we get the u and v velocity for the stagnation point flow.

$$\left. \begin{aligned} u &= 2U_\infty x \\ v &= -2U_\infty y \end{aligned} \right\} \tag{18}$$

The flow structure represented by the above equations is for ideal fluid flow. The direction of the flow is obtained by finding the velocity at particular points using equation (18). For instance, at positive values of x, the u velocity ($\boldsymbol{i}$ component of velocity) is positive (flow is in the positive x direction) and for positive values of y, the v velocity ($\boldsymbol{j}$ component of velocity) is negative (flow is in the negative y direction). Hence the flow direction is as shown in Figure 2-1.

113

Exact solution to 2-D, viscous stagnation point flow

The velocity field in equation (18) satisfy the continuity and N-S equation as it was derived using these equations. However, the assumption made was that the fluid is inviscid and hence the viscous terms were neglected. The potential solution obtained is valid for areas where the inertial forces dominate and not the viscous forces. Inside the boundary layer, viscous forces are dominant and no slip boundary condition should be satisfied. Hence the solution obtained above is not correct within the boundary layer including at the surface of impingement.

The stream function is modified such that the function varies with y in a way that it satisfies the no slip condition [11]:

$$\psi = 2U_\infty x f(y) \tag{19}$$

Then using equation (3) we get the velocity components:

$$\left. \begin{array}{l} u = 2U_\infty x f'(y) \\ v = -2U_\infty f(y) \end{array} \right\} \tag{20}$$

The 2-D N-S equation with viscosity term is shown below:

$$\left. \begin{array}{l} u\dfrac{\partial u}{\partial x} + v\dfrac{\partial u}{\partial y} = -\dfrac{1}{\rho}\dfrac{\partial p}{\partial x} + v\left[\dfrac{\partial^2 u}{\partial x^2} + \dfrac{\partial^2 u}{\partial y^2}\right] \\ u\dfrac{\partial v}{\partial x} + v\dfrac{\partial v}{\partial y} = -\dfrac{1}{\rho}\dfrac{\partial p}{\partial y} + v\left[\dfrac{\partial^2 v}{\partial x^2} + \dfrac{\partial^2 v}{\partial y^2}\right] \end{array} \right\} \tag{21}$$

Substituting equation (20) into (21) we get:

$$4U_\infty^2 x(f')^2 - 4U_\infty^2 x f f'' = -\dfrac{1}{\rho}\dfrac{\partial p}{\partial x} + 2U_\infty v x f'''$$

$$4U_\infty^2 f f' = -\dfrac{1}{\rho}\dfrac{\partial p}{\partial y} - 2U_\infty v f''$$

Integrating the last equation w.r.t y,

$$\int 4U_\infty^2 f f' dy = \int \left(-\dfrac{1}{\rho}\dfrac{\partial p}{\partial y} - 2U_\infty v f''\right) dy$$

$$2U_\infty^2 f^2 = -\dfrac{1}{\rho}p(x,y) + g(x) - 2U_\infty v f'$$

Or,

114

$$p(x, y) = -2\rho U_\infty^2 f^2 - 2\rho U_\infty v f' + g(x) \tag{22}$$

From Bernoulli's equation for an inviscid flow,

$$\frac{1}{2}\rho(u^2 + v^2) + p = p_0$$

Where, p_0 is the total pressure at stagnation point (stagnation pressure). Substituting equation (18), we get:

$$p = p_0 - 2\rho U_\infty^2 (x^2 + y^2)$$

Comparing this equation to equation (22), we get g(x):

$$g(x) = p_0 - 2\rho U_\infty^2 x^2 + 2\rho U_\infty v$$

Then pressure distribution becomes,

$$p = p_0 - 2\rho U_\infty^2 f^2 + 2\rho U_\infty v(1 - f') - 2\,\rho U_\infty^2 x^2 \tag{23}$$

Taking derivative of p w.r.t x we get

$$\frac{\partial p}{\partial x} = -4\rho U_\infty^2 x$$

Substituting this equation in the x momentum of equation (21) and rearranging, we get a non-linear, third order ordinary differential equation:

$$\frac{v}{2U_\infty} f''' + ff'' - (f')^2 + 1 = 0 \tag{24}$$

Using Boundary condition as:

$$\left.\begin{array}{l} u(x, 0) = 0 \implies f'(0) = 0 \\ v(x, 0) = 0 \implies f(0) = 0 \\ y \to \infty \implies f(y) \to y \\ y \to \infty \implies f'(y) \to 1 \end{array}\right\} \tag{25}$$

To make equation (24) free of viscosity parameter and free stream velocity, let

$$\Phi(\eta) = \sqrt{\frac{2U_\infty}{v}} f(y) \tag{26}$$

And

$$\eta = \sqrt{\frac{2U_\infty}{v}} y \tag{27}$$

Then, equation (24) and (25) may be modified as:

$$\Phi''' + \Phi\Phi'' - (\Phi')^2 + 1 = 0 \tag{28}$$

$$\left.\begin{array}{c}\Phi(0) = \Phi'(0) = 0 \\ \eta \to \infty \implies \Phi'(\eta) \to 1\end{array}\right\} \tag{29}$$

And differentiation in the above equations is with respect to η.

Thus, the velocity field in a stagnation point flow is given by:

$$\left.\begin{array}{c}u = 2U_\infty x \Phi' \\ v = -\sqrt{2U_\infty \nu}\,\Phi\end{array}\right\} \tag{30}$$

The stream function is obtained using equation (3). The boundary layer thickness (δ) is given by equation (32) [8].

$$\psi = x\Phi(\eta)\sqrt{2U_\infty \nu} \tag{31}$$

$$\delta = 2.4 \sqrt{\frac{\nu}{2U_\infty}} \tag{32}$$

APPENDIX B - SCRIPTS/CODES

Matlab code for plotting 2-D, inviscid stream function in Figure 2-2

```
% Program to compute streamlines from stream function psi = 2xy
% Function "compute(y,x,c1)" contains the stream function
% where c1 is the current constant

clear;
x = linspace(-5,5,250);
c = linspace(0,10,15);
hold on;
for i = 1:15
   c1 = c(i);
    for j = 1:250
       y(j,i) = fzero(@compute,1,[],x(j),c1);
   end
end

plot(x,y,'Color','Blue');
plot(0,0:.001:5,'Color','Blue');
axis([-5 5 -1 5]);

% Function "compute":

function f = compute (y,x,c1)
if x <= 0
    f = 2*x*y+c1;
else
    f = 2*x*y-c1;
end
```

Macro code for geometry and mesh creation in gambit (axisymmetric single-jet case)

```
/ Topic: Single Jet Impingement
/ Author: Karan Anand
/ Case: 3D - quarter model – Axisymmetric
/ Notes: For use in GAMBIT ONLY
/ ------

/ Resetting meshing model if there exists any.
reset

/ Defining Geometric Inputs; Enter the inputs here:
/  where    Re              Reynolds #
/           HbyD            H/D ratio
/           title           Current file name for saving purposes
/           mesh_title      Save mesh as [title]
$Re = 6000
```

```
$HbyD = 6
$title = "Case1.dbs"
$mesh_title = "H_D-6_RE-6000.msh"

/ Defining constant parameters
/   where D Nozzle Diameter
/       B   Base plate Diameter
$D = 500e-06
$B = 10 * $D

/ Defining Meshing Inputs; Enter the inputs here:
/   where interval_nozzle: Volume mesh for nozzle; Total # of intervals
/     node_edge_ratio: Edge mesh for symmetric edges on wall faces;
/Ratio of increment of nodes; denser near center
/     edge_interval_size: Edge mesh for symmetric edges perpendicular
to wall faces; Interval size; smaller the number, denser the mesh
$interval_nozzle = 35
$node_edge_ratio = 0.98
$edge_interval_size = (($B/2)/($interval_nozzle))

/ Calculating dependent variables
/   where H distance between top and bottom plate
/       Le Nozzle entrance length (nozzle height) ~20D (For all
conditions)
$H = $HbyD * $D
$Le = 20 * $D

/ Main Program
save name $title
solver select "FLUENT 5/6"

/ Geometry creation
volume create height $Le radius1 ($D/2) radius3 ($D/2) offset 0 0
($Le/2) \
  zaxis frustum
volume create height $H radius1 ($B/2) radius3 ($B/2) offset 0 0
(($H/2)*-1) \
  zaxis frustum
volume unite volumes "volume.1" "volume.2"
volume create width 0.01 depth 0.01 height 0.1 offset 0.005 0.005 0.05
brick
volume move "volume.2" offset 0 0 -0.01
volume intersect volumes "volume.1" "volume.2"
vertex create coordinates 0 0 0
edge split "edge.25" vertex "vertex.19" connected
edge create straight "vertex.19" "vertex.15"
edge create straight "vertex.19" "vertex.1"
face create wireframe "edge.31" "edge.23" "edge.32" real
volume create translate "face.17" onedge "edge.25" reverse
volume split "volume.1" volumes "volume.2" connected
volume create translate "face.17" onedge "edge.30"
```

```
volume split "volume.1" volumes "volume.4" connected


/ Meshing
volume mesh "volume.2" cooper source "face.17" "face.3" intervals
$interval_nozzle
undo begingroup
/ … script truncated for spacing
blayer attach "b_layer.1" face "face.30" "face.10" "face.22" "face.31"
edge "edge.51" "edge.18" "edge.17" "edge.52" \
  add
undo endgroup
undo begingroup
edge modify "edge.24" "edge.51" backward
edge picklink "edge.24" "edge.51" "edge.18" "edge.22"
edge modify "edge.22" "edge.24" "edge.18" "edge.51" successive ratio1
$node_edge_ratio \
    intervals ($interval_nozzle*2)
undo endgroup
undo begingroup
edge modify "edge.20" "edge.55" backward
edge picklink "edge.20" "edge.55" "edge.21" "edge.54" "edge.30"
edge modify "edge.54" "edge.20" "edge.55" "edge.21" "edge.30"
successive ratio1 $node_edge_ratio \
  intervals $interval_nozzle
undo endgroup
/ … script truncated for spacing
volume  mesh  "volume.4"  cooper  source  "face.29"  "face.17"  intervals

$interval_nozzle


/ Boundary type specification
physics create "symmetryx" btype "SYMMETRY" face "face.30" "face.22"
physics create "symmetryy" btype "SYMMETRY" face "face.10" "face.31"
physics create "pipe_symmetryx" btype "SYMMETRY" face "face.16"
physics create "pipe_symmetryy" btype "SYMMETRY" face "face.23"
physics create "Outlet" btype "PRESSURE_OUTLET" face "face.15"
physics create "inlet" btype "VELOCITY_INLET" face "face.3"
physics create "target_plate" btype "WALL" face "face.14" "face.29"
physics create "pipe_wall" btype "WALL" face "face.2"
physics create "top_plate" btype "WALL" face "face.7"
save


/ Exporting mesh
export fluent5 $mesh_title
```

Codes pertaining to automation in Fluent and Icem-CFD are not shown as the scripts are lengthy.

APPENDIX C - SAMPLE CALCULATIONS

Validation of Continuum Law using Knudsen Number

$$K_n = \frac{\lambda}{D} \tag{33}$$

Where λ is the mean free path of air, D is the jet diameter and K_n is the Knudsen number.

For a single species of gas, the λ is given by:

$$\lambda = \frac{1}{n\sigma} \tag{34}$$

Where n is the gas density and σ is the gas particle collision cross section.

Solving for gas density using ideal gas law we have:

$$\left. \begin{array}{l} PV = NkT \\ P = \dfrac{N}{V}kT = nkT \\ n = \dfrac{P}{kT} \end{array} \right\} \tag{35}$$

Where V is the volume occupied by the gas, N is the total number of gas particles, k is the Boltzmann's constant and n is the gas density = N/V. Substituting n in equation (35) into equation (34) we get:

$$\lambda = \frac{1}{\dfrac{P}{kT}\sigma} = \frac{kT}{P\sigma} \tag{36}$$

The gas particle collision cross section is given by equation (37) with d being the particle diameter:

$$\sigma = \pi d^2 \tag{37}$$

Since particle diameter is difficult to find for air as such, assuming air is composed of nitrogen only (about 70% is nitrogen) and that the particles behave like hard spheres, the diameter of diatomic nitrogen (N_2) is (2 x 3.1 [Å] = 6.2 [Å]). Thus,

$$\sigma = \pi(6.2 \times 10^{-10})^2 = 1.21 \times 10^{-18}[m^2] \tag{38}$$

Substituting equation (38) in equation (36), we have

$$\lambda = \frac{1.381 \times 10^{-23}[J/K] \cdot 300 \ [K]}{101.33 \ [kPa] \cdot 1.21 \times 10^{-18}[m^2]} = 3.38 \times 10^{-8}[m] \tag{39}$$

The Knudsen number is then solved using equation (33). It should be noted that this assumption was for nitrogen and not air. For air at STP for a 125 [μm] diameter nozzle the Knudsen number increases further approaching the slip condition. However, for the case considered, the assumption of no slip is valid. The Knudsen number may be further related to the Reynolds number and Nusselt number as shown below:

Relation of Knudsen Number to Reynolds number and Nusselt number

The viscosity and the mean free path are related as:

$$\mu = \frac{\rho \bar{c} \lambda}{2}$$

Where μ is the dynamic viscosity, and the density ρ is the given by the product $n \cdot m$; where, n is the number density and m is molar mass of air with $\bar{c}$ being the average molecular speed (from Maxwell-Boltzmann distribution). And,

$$\bar{c} = \sqrt{\frac{8kT}{\pi m}}$$

Substituting the above equations and from equations of Reynolds and Nusselt number we get:

$$\left.\begin{array}{l} K_n = \dfrac{U_\infty}{Re} \sqrt{\dfrac{\pi m}{2kT}} \\[3mm] K_n = \dfrac{1}{Nu} \dfrac{h\mu}{k\rho} \sqrt{\dfrac{\pi m}{2kT}} \end{array}\right\} \qquad (40)$$